University Library

A gateway to Melbourne's research publications

Minerva Access is the Institutional Repository of The University of Melbourne

Author/s:
Sun, Chuanbowen

Title:
Advanced techniques for field recovery via direct detection

Date:
2020

Persistent Link:
https://hdl.handle.net/11343/268329

Terms and Conditions:
Terms and Conditions: Copyright in works deposited in Minerva Access is retained by the copyright owner. The work may not be altered without permission from the copyright owner. Readers may only download, print and save electronic copies of whole works for their own personal non-commercial use. Any use that exceeds these limits requires permission from the copyright owner. Attribution is essential when quoting or paraphrasing from these works.

Advanced Techniques for Field Recovery via Direct Detection

Chuanbowen Sun

Submitted in partial fulfilment of the requirements of the degree of
Doctor of Philosophy

Department of Electrical and Electronic Engineering

THE UNIVERSITY OF MELBOURNE

December 2020

Copyright © Chuanbowen Sun

All rights reserved. No part of the publication may be reproduced in any form by print, photoprint, microfilm or any other means without written permission from the author.

Abstract

The recent decade has witnessed the rapid growth of data traffic driven by various bandwidth-rich applications. Accordingly, both short-reach and long-haul fiber based optical networks are in great demand. For the long-haul transports, coherent detection is dominant due to its superior performance. Although the hardware structure of coherent systems possesses large footprint and the corresponding DSP algorithms are complicated, the cost is amortised by the high capacity and long transmission distance. While for short- to medium-reach transports such as intra- and inter- data center connections and metropolitan networks, cost is one primary concern. As such, direct detection has attracted extensive research interests due to its simple structure and low cost.

To support short- and medium-reach optical transports in a cost-effective manner, field recovery is a promising solution since it enables the chromatic dispersion (CD) compensation. Given the cost of the transmission link, direct detection with the recovery of optical field has attracted extensive attention. For direct detection systems, the signal-signal beat interference (SSBI) induced by the square-law detection is a major limiting factor of obtaining the replica of information-bearing signal. As such, various algorithms dealing with SSBI have been proposed in the recent years.

In this thesis, the optical field recovery of directly detected single sideband (SSB) and double sideband (DSB) signals has been studied and proposed. For SSB signals, without inserting a frequency gap to accommodate SSBI, Kramers-Kronig (KK) and iterative cancellation (IC) receivers enable the high spectral efficiency. The appropriate modulation formats fitting for both KK and IC receivers have been analysed. As KK and IC receivers are designed for the transmission links consisting of several spans of fiber, CD impacts on the performance of KK and IC receivers are investigated. Results show that the single-carrier modulation format is the better fit for KK receivers, while OFDM signals outperform single-carrier signals for IC receivers. Due to accumulated CD impacts after transmission, the peak-to-average power ratio

(PAPR) of the single-carrier signals increases, which is more likely to violate the minimum phase condition of KK receivers compared to the back-to-back (btb) condition. Accordingly, the KK receiver requires a higher CSPR after transmission, while the optimal CSPR for the IC receiver remains the same as the btb case. The first-order polarization mode dispersion (PMD) impacts are also investigated, and it is demonstrated that PMD is not a major limiting factor for the KK receiver.

For the field recovery of DSB signals, the direct detection scheme called carrier-assisted differential detection (CADD) has been theoretically analysed and experimentally demonstrated. The algorithm of recovering DSB signal field using CADD receiver has been elaborated, and the design guideline of CADD receiver including the joint optimization of several key parameters is given via simulations. Besides, the first-time experimental demonstration of the CADD receiver has been conducted. Experimental results show that the required receiver bandwidth is reduced by 41% compared with SSB based direct detection schemes. From the perspective of practical implementation, the IQ imbalance impacts of the CADD scheme have been analysed, and the tolerance of amplitude and phase mismatch is given.

Lastly, to alleviate the requirement of high CSPR, several DSP algorithms have been proposed. For the SSB direct detection scheme, both enhanced SSBI mitigation and virtual CSPR enhancement schemes can effectively reduce the CSPR by 2 to 3 dB. For the DSB signal based CADD receiver, a simple but effective power loading scheme is proposed to enhance the performance of low-frequency subcarriers, and hence predominantly reduce the required high CSPR.

Declaration

This thesis comprises only my own work towards the degree of Doctor of Philosophy except where indicated in the preface. Due acknowledge has been made in the text to all other material used, and this thesis is less than 100,000 words in length, exclusive of figures, tables, bibliographies, and appendices.

Space

Acknowledgements

I would like to express my sincere gratitude to many adorable individuals, without their supervision, guidance, cooperation, and assistance, the work in this thesis cannot be accomplished.

First, my utmost appreciation goes to my supervisors Prof. William Shieh and Dr. Robert Schmid for their high-quality supervision and insightful advice during my PhD candidature. Every time when I confront difficulties, their expertise and patient instructions can always guide and enlighten me. I would also like to appreciate all the valued and experienced comments from the committee chair Prof. Luis Fernando Ochoa Pizzali.

Second, I am grateful to the University of Melbourne and Department of Electrical & Electronic Engineering for the generous scholarship and world-class research environment. Without these supports, this thesis cannot be completed.

I would also like to thank my friends and colleagues for the stimulating discussions and encouragements during my PhD candidature at the University of Melbourne: Dr. Di Che, Dr. Yifei Wang, Dr. Jian Fang, Dr. Miao Sun, Honglin Ji, Zhaopeng Xu, Tonghui Ji, and Rebecca Dong. With their valued suggestions and assistance, the research and life at the University of Melbourne become different.

Last but not the least, I am indebted to my parents, for their understanding and constant support. I would not be the same without their unconditional love.

Space

Preface

(i) Contents arising from each contributing chapter towards the thesis:

Original contributions (overall percentage: 90%) of Chapter 3: conducted the simulation of a combination of two receiver schemes and two modulation formats, simulated the channel impairment impacts, analysed the simulation results, verified the simulation results via experiments, collected experimental data and obtained the conclusion.

Contributions from co-contributors (overall percentage: 10%) of Chapter 3: supervised the entire work (name of co-contributors: William Shieh); aided with the experiments, paper writing and revision (name of co-contributors: Di Che, Honglin Ji, and Robert Schmid).

Original contributions (overall percentage: 75%) of Chapter 4: proposed the algorithm of recovering the field of double sideband signals, conducted the simulation of CADD scheme, identified the optimal parameters, presented the design guideline of CADD receiver, demonstrated the first experiment of CADD receiver, processed the experimental data, and analysed the IQ imbalance tolerance.

Contributions from co-contributors (overall percentage: 25%) of Chapter 4: conceived the structure of CADD receiver, supervised the overall project, paper writing and revision (name of co-contributors: William Shieh); contributed to the simulation, helped with the experimental demonstration, and analysed the results (name of co-contributors: Honglin Ji, Tonghui Ji, and Zhaopeng Xu).

Original contributions (overall percentage: 90%) of Chapter 5: proposed the algorithms to relax the requirements of high CSPR, theoretical derivations, verified the proposed schemes via experiments, processed the experimental data, and analysed the results.

Contributions from co-contributors (overall percentage: 10%) of Chapter 5: supervised the overall project and paper revision (name of co-contributors: William Shieh); aided with the experimental setup design, contributed to the algorithms, and analysed the results (name of co-contributors: Di Che, Honglin Ji, Tonghui Ji, and Zhaopeng Xu).

(ii) None of the work towards the thesis has been submitted for other qualifications.

(iii) None of the work towards the thesis was carried out prior to enrolment in the degree.

(iv) No third-party editorial assistance was provided in preparation of the thesis.

(v) Publications arising from each contributing chapter towards the thesis:

Publications arising from Chapter 3:

(1) C. Sun, D. Che, H. Ji, and W. Shieh, "Investigation of single- and multi-carrier modulation formats for Kramers-Kronig and SSBI iterative cancellation receivers," Optics Letters, vol. 44, no. 7, pp. 1785-1788, Apr. 2019.

Contributions: Chuanbowen Sun (overall percentage: 85%): manuscript writing, built up simulation system, and analysed results. Di Che (overall percentage: 4%): aided with the simulation work, and contributed to the manuscript revision. Honglin Ji (overall percentage: 4%): aided with the simulation work, and contributed to the manuscript revision. William Shieh (overall percentage: 7%): supervised the overall project, evaluated and revised the manuscript.

(2) C. Sun, D. Che, and W. Shieh, "Comparison of chromatic dispersion sensitivity between Kramers-Kronig and SSBI iterative cancellation SSB receiver," Optical Fiber Communication Conference (OFC) 2018, paper W4E. 4.

Chuanbowen Sun (overall percentage: 85%): manuscript writing, built up simulation system, and analysed results. Di Che (overall percentage: 6%):

aided with the simulation work, and contributed to the manuscript revision. William Shieh (overall percentage: 9%): supervised the overall project, evaluated and revised the manuscript.

(3) C. Sun, D. Che, H. Ji, and W. Shieh, "Study of chromatic dispersion impacts on Kramers-Kronig and SSBI iterative cancellation receiver," IEEE Photonics Technology Letters, vol. 31, no. 4, pp. 303-306, Jan. 2019.

Chuanbowen Sun (overall percentage: 85%): manuscript writing, conducted the experimental demonstration, collected data, carried out signal processing, and analysed results. Di Che (overall percentage: 4%): aided with the setup of the experiment, and contributed to the manuscript revision. Honglin Ji (overall percentage: 4%): aided with the setup of the experiment, and contributed to the manuscript revision. William Shieh (overall percentage: 7%): supervised the overall project, evaluated and revised the manuscript.

(4) C. Sun, D. Che, R. Schmid, and W. Shieh, "Polarization mode dispersion impacts on Kramers-Kronig receiver," Optoelectronics and Communications Conference (OECC) 2018, paper 4B4-3.

Chuanbowen Sun (overall percentage: 85%): manuscript writing, built up simulation system, and analysed results. Di Che (overall percentage: 4%): aided with the simulation work, and contributed to the manuscript revision. Robert Schmid (overall percentage: 4%): evaluated and revised the manuscript. William Shieh (overall percentage: 7%): supervised the overall project, evaluated and revised the manuscript.

Publications arising from Chapter 4:

(1) W. Shieh, C. Sun, and H. Ji, "Carrier-assisted differential detection," Light: Science & Applications, vol. 9, no. 1, pp. 1–9, Feb. 2020.

William Shieh (overall percentage: 60%): conceived the receiver structure, proposed the algorithm of mitigating SSBI, manuscript writing, and analysed results. Chuanbowen Sun (overall percentage: 30%): built the theoretical

model, proposed the algorithm of the double sideband signal field recovery, conducted the system simulation, identified the optimal parameters, contributed to the manuscript writing. Honglin Ji (overall percentage: 10%): contributed to the algorithms and manuscript writing.

(2) C. Sun, T. Ji, H. Ji, Z. Xu, and W. Shieh, "Experimental demonstration of complex-valued DSB signal field recovery via direct detection," IEEE Photonics Technology Letters, vol. 32, no. 10, pp. 585-588, May. 2020.

Chuanbowen Sun (overall percentage: 85%): manuscript writing, conducted the experimental demonstration, collected data, carried out signal processing, and analysed results. Tonghui Ji (overall percentage: 3%): aided with the experimental setup, manuscript revision and result analysis. Honglin Ji (overall percentage: 3%): aided with the experimental setup, manuscript revision and result analysis. Zhaopeng Xu (overall percentage: 3%): aided with the experimental setup, manuscript revision and result analysis. William Shieh (overall percentage: 6%): supervised the overall project, evaluated and revised the manuscript.

(3) C. Sun, H. Ji, T. Ji, Z. Xu, and W. Shieh, "Impacts of IQ imbalance on carrier assisted direct detection," Pacific Rim Conference on Lasers and Electro-Optics (CLEO-PR 2020), paper 4F.6.

Chuanbowen Sun (overall percentage: 85%): manuscript writing, built up simulation system, and analysed results. Honglin Ji (overall percentage: 3%): aided with the setup of simulation model and result analysis. Tonghui Ji (overall percentage: 3%): aided with the setup of simulation model and result analysis. Zhaopeng Xu (overall percentage: 3%): aided with the setup of simulation model and result analysis. William Shieh (overall percentage: 6%): supervised the overall project, evaluated and revised the manuscript.

Publications arising from Chapter 5:

(1) C. Sun, D. Che, H. Ji, and W. Shieh, “Towards low carrier-to-signal power ratio for Kramers-Kronig receiver,” Optical Fiber Communication Conference (OFC) 2019, paper M1H. 6.

Chuanbowen Sun (overall percentage: 85%): manuscript writing, conducted the experimental demonstration, collected data, carried out signal processing, and analysed results. Di Che (overall percentage: 4%): aided with the setup of the experiment, and contributed to the manuscript revision. Honglin Ji (overall percentage: 4%): aided with the setup of the experiment, and contributed to the manuscript revision. William Shieh (overall percentage: 7%): supervised the overall project, evaluated and revised the manuscript.

(2) C. Sun, D. Che, H. Ji, and W. Shieh, “Virtual carrier-to-signal power ratio enhancement for Kramers-Kronig receivers,” European Conference on Optical Communication (ECOC) 2019, paper Tu.1.D.3.

Chuanbowen Sun (overall percentage: 85%): manuscript writing, built up simulation system, and analysed results. Di Che (overall percentage: 4%): aided with the setup of the experiment, and contributed to the manuscript revision. Honglin Ji (overall percentage: 4%): aided with the setup of the experiment, and contributed to the manuscript revision. William Shieh (overall percentage: 7%): supervised the overall project, evaluated and revised the manuscript.

(3) C. Sun, H. Ji, T. Ji, Z. Xu, and W. Shieh, “Power loading for carrier assisted differential detection,” Asia Communications and Photonics Conference (ACP) 2020, paper M3B.4.

Chuanbowen Sun (overall percentage: 85%): manuscript writing, built up simulation system, and analysed results. Honglin Ji (overall percentage: 3%): aided with the simulation, and contributed to the manuscript revision. Tonghui Ji (overall percentage: 3%): aided with the simulation, and contributed to the manuscript revision. Zhaopeng Xu (overall percentage: 3%): aided with the result analysis, and contributed to the manuscript revision. William Shieh

(overall percentage: 6%): supervised the overall project, evaluated and revised the manuscript.

Content

Chapter 1 Introduction 1
1.1. Introduction 1
1.2. Motivations for field recovery via direct detection 3
1.3. Thesis outline 6
1.4. Contributions 7
1.5. Publications 8
Chapter 2 Basic principle and literature review 11
2.1. Introduction 11
2.2. Optical signal generation for optic-fiber transmission 12
2.2.1. Intensity modulation using DML 13
2.2.2. Intensity modulation using EML 16
2.2.3. Intensity modulation using dual-drive MZM 17
2.2.4. IQ modulation using coherent IQ MZM 19
2.2.5. Optical SSB signal generation 21
2.3. Receiver for optical transmission systems 26
2.3.1. Direct detection 26
2.3.2. Coherent detection 28
2.4. Self-coherent system 31
2.5. Techniques of SSBI mitigation 33
Chapter 3 Field recovery of SSB signal via direct detection 43
3.1. Introduction 43
3.2. KK vs. SSBI iterative cancellation receiver scheme 44
3.2.1. Principle of KK receiver 44
3.2.2. Principle of SSBI iterative cancellation 46
3.3. Investigation of modulation formats: single- or multi-carrier modulation? 47

3.4. Chromatic dispersion impacts 56
3.5. Polarization mode dispersion impacts 62
Chapter 4 Field recovery of DSB signal via direct detection 66
4.1. Introduction 66
4.2. Structure and principle of CADD receiver 68
4.3. Simulation and experimental demonstration of CADD 72
4.3.1. Transfer function for CADD 72
4.3.2. Length of optical delay 73
4.3.3. Optimal CSPR 75
4.3.4. Simulated OSNR sensitivity 77
4.3.5. Experimental demonstration and results 83
4.4. IQ imbalance impacts on CADD 86
Chapter 5 Towards low CSPR for direct detection schemes 90
5.1. Introduction 90
5.2. Enhanced SSBI mitigation 92
5.3. Virtual CSPR enhancement 96
5.4. Power loading scheme for CADD 101
Chapter 6 Conclusions 109
6.1. Summary of this work 109
6.1.1. Field recovery of SSB signal 109
6.1.2. Field recovery of DSB signal 110
6.1.3. Techniques of reducing CSPR 111
6.2. Future work and perspectives 111

List of Figures

Fig. 2.1(a) Fabry-Perot optical cavity. (b) Transmittance as a function of frequency. *13*
Fig. 2.2 Operation principle of DFB laser diode. *14*
Fig. 2.3 Measured optical power vs bias current curve of a DML. Insets(i) and (ii) are the eye diagrams of electrical and optical PAM-4 signals, respectively. *15*
Fig. 2.4 Conceptual structure of a dual-drive Mache-Zander modulator. *17*
Fig. 2.5 Power transfer function of an MZM. *18*
Fig. 2.6 Conceptual structure of a coherent IQ modulator. Insets (i) and (ii) are the in-phase and quadrature modulated PAM-4 signals, and inset (iii) presents the corresponding constellation of QAM 16 signals. *19*
Fig. 2.7 Field transfer function of the coherent IQ modulator. *20*
Fig. 2.8 (a) Amplitude response of the Hilbert transform. (b) Phase response of the Hilbert transform. *22*
Fig. 2.9 SSB signal generation and the corresponding spectra using optical Hilbert transformer. *24*
Fig. 2.10 Transmitter schemes for carrier assisted SSB signal generation with the corresponding spectra and bias points. DAC: digital to analog converter. PC: polarization controller. *25*
Fig. 2.11 A basic coherent receiver structure. PC: polarization controller. *28*
Fig. 2.12 Structure of a phase-diversity homodyne receiver using a 90-degree optical hybrid. *30*
Fig. 2.13 Spectra of SSB signal with (a) guard band (b) interleaved loading (c) no frequency gap before and after direct detection. *34*
Fig. 2.14 DSP flow chart for the single-stage linearization. *36*
Fig. 2.15 Transmitter structure of optical SSBI mitigation scheme. *37*
Fig. 2.16 Optical SSBI mitigation at the receiver. *38*
Fig. 2.17 Transmitter structure for block-wise phase switching scheme. *39*
Fig. 2.18 Three approaches of data sequence for block-wise phase switching scheme. *40*
Fig. 2.19 Receiver structure for signal-carrier interleaved direct detection scheme. *41*
Fig. 2.20 Two approaches of data sequence for signal-carrier interleaved direct detection scheme. *41*
Fig. 3.1 DSP flow chart for (a) single carrier using KK receiver, (b) OFDM using KK receiver, (c) single carrier using IC receiver, and (d) OFDM using IC receiver. *48*
Fig. 3.2 System performance of KK receiver with single-carrier and OFDM modulation formats at btb. *49*
Fig. 3.3 BER performance as a function of CSPR for KK receiver at btb for (a) single-carrier and (b) OFDM signals. *50*
Fig. 3.4 PAPR of OFDM and single-carrier signals versus the transmission distance. *51*
Fig. 3.5 System performance of KK receiver using single-carrier and OFDM signals after (a) 40- and (b) 1000-km transmission. *52*
Fig. 3.6 System performance of IC receiver with single-carrier and OFDM modulation formats at btb. *53*
Fig. 3.7 System performance of IC receiver versus iteration number at btb. *54*
Fig. 3.8 BER as a function of CSPR for IC receiver at btb for (a) single-carrier and (b) OFDM. *54*
Fig. 3.9 System performance of IC receiver using single-carrier and OFDM signals after (a) 40- and (b) 1000-km transmission. *55*
Fig. 3.10 Experimental setup of KK and IC receiver. ECL: external cavity laser. *58*
Fig. 3.11 Q-factor as a function of iteration number at btb for (a) OFDM, and (b) single-carrier signals with various CSPRs. (c-h) are the OFDM signal constellations without the iterative cancellation and with 1-, 2-, 3-, 4-, 5-times iterations, respectively. *59*
Fig. 3.12 Q-factor as a function of CSPR at various OSNRs for the IC receiver (a) at btb, (b) after 160-km transmission. *60*
Fig. 3.13 Q-factor as a function of CSPR at various OSNRs for the KK receiver (a) at btb, (b) after 160-km transmission. *61*

Fig. 3.14 Required OSNR versus transmission distance for both KK and IC receiver (@BER=1.0×10^{-3}). *61*
Fig. 3.15 BER versus OSNR for 25Gbaud QAM16 signals using KK receiver with various DGD. *64*
Fig. 3.16 Q-factor penalty as a function of DGD @BER=4×10^{-3}. *64*
Fig. 4.1 Conceptual diagram of the TIR based receiver. D indicates the dispersive medium, and DSF represents dispersion shifted fiber. *67*
Fig. 4.2 Conceptual diagram of CADD receiver. *68*
Fig. 4.3 DSP flow chart for CADD receiver. Inset(i) is the spectrum of DSB signals, where S_l and S_u are the lower and upper sideband signals, respectively. FFT: fast Fourier transform. IFFT: inverse fast Fourier transform. *70*
Fig. 4.4 Magnitude of transfer function H(f) for CADD with the optical delay of 50 ps. SSBI suppression is defined as |H(f)|>1. ..... *72*
Fig. 4.5 (a) Signal spectra before and after implementing transfer function H(f). (b) SSBI spectra before and after implementing transfer function H(f). *73*
Fig. 4.6 BER performance versus OSNR with varying optical delays. *74*
Fig. 4.7 BER as a function of iteration number for 25-Gbaud QAM 16 signals @ CSPR of 8 dB, optical delay of 60 ps, and frequency gap of 10%. Insets are the corresponding constellations for each iteration @ OSNR=28 dB. *75*
Fig. 4.8 BER versus CSPR for 25-Gbaud signals (a) with 5% frequency gap, (b) with 20% frequency gap. *76*
Fig. 4.9 OSNR sensitivity of CADD and KK receiver with varying frequency gaps at back-to-back.. *78*
Fig. 4.10 Mutual information of CADD and KK receiver with varying frequency gaps at back-to-back. *78*
Fig. 4.11 SNR versus frequency for 25-Gbaud signals with 10% frequency gap, 60-ps optical delay, 8-dB CSPR, and 30-dB OSNR. *80*
Fig. 4.12 Transmission performance of CADD and KK receivers with each optimal parameter. *81*
Fig. 4.13 Experimental setup for CADD scheme. *83*
Fig. 4.14 Scaled coefficient η used in the experimental demonstration versus CSPR. *84*
Fig. 4.15 BER versus the number of iterations for various CSPRs after transmission of 160-km SSMF. Insets (i-iv) are corresponding constellations for each iteration with the CSPR of 8 dB. *85*
Fig. 4.16 (a) Optimization of CSPR at various OSNRs. (b) BER versus OSNR for various CSPRs. *86*
Fig. 4.17 OSNR sensitivity @BER=4×10^{-3} versus amplitude and phase imbalance. *88*
Fig. 4.18 (a) BER as a function of OSNR for the cases with no IQ imbalance (alpha=1, beta=0) and with IQ imbalance (alpha=0.8, beta=0.2), respectively. (b) BER as a function of iteration number for two bold diamond points shown in (a). *88*
Fig. 5.1 DSP flow chart of the modified KK receiver scheme with the corresponding spectra. *91*
Fig. 5.2 Interleaved subcarrier loading for CADD receiver. *91*
Fig. 5.3 DSP flow chart for the proposed enhanced SSBI mitigation scheme. *94*
Fig. 5.4 Q-factor versus OSNR for different CSPRs. (a) 4-, (b) 6-, (c) 8-dB CSPR. Scheme 1: conventional KK receiver. Scheme 2: proposed enhanced SSBI mitigation based on KK relation. *94*
Fig. 5.5 (a)System performance after 40- and 160-km transmission. (b) Required OSNR as a function of transmission distance for various CSPRs. Scheme 1: conventional KK receiver. Scheme 2: proposed enhanced SSBI mitigation based on KK relation. *95*
Fig. 5.6 DSP flow chart for the proposed virtual CSPR enhancement scheme. *98*
Fig. 5.7 Required OSNR and optimal ΔCSPR as a function of original CSPR in the btb configuration. *98*
Fig. 5.8 Required OSNR and optimal ΔCSPR as a function of original CSPR after 160-km transmission. *100*
Fig. 5.9 BER performance versus OSNR for the CADD receiver with uniform power loading. *101*
Fig. 5.10 Required OSNR for each CSPR. *102*
Fig. 5.11 Schematic diagram of triangular power loading scheme. Sl *and* Su *are lower and upper sideband signals, respectively.* *103*

Fig. 5.12 Optimization of bandwidth of the frequency region to implement triangular power loading. 104
Fig. 5.13 Joint optimization of amplitude and bandwidth for the triangular power loading. 105
Fig. 5.14 SNR versus frequency for 25Gbaud signals with 5% frequency gap with triangular power loading @ optical delay=60 ps, CSPR=9 dB, and OSNR=28 dB. 106
Fig. 5.15 (a) BER versus OSNR. (b) Mutual information versus OSNR for uniform and triangular power loading. 107

List of Tables

Table 1.1 Trans-Atlantic telephone cable (TAT) *2*
Table 4.1 Optimal delay and CSPRs for 25-Gbaud 16 QAM signals with each frequency gap. *77*
Table 4.2 Cost metrics of 200-Gb/s net interface rate per wavelength per polarization detection systems with field recovery. This table is reproduced from ref [94], and OSNR is set to be 30dB. BW: bandwidth *82*

Chapter 1 Introduction

1.1. Introduction

Modern civilization has witnessed the evolution of communication, and human beings have never stopped exploring the possibility of various communication approaches. Face-to-face oral conversation is primitive with very limited speed and reach, as such, for centuries people are consistently pursuing for solutions of constant connections over long distance with low latency [1].

Optical communication can be traced back to 800 BC, when fire signals were used by the Greeks. After that, fire signal relay was developed to enable signal transmission over a distance. In the modern society, the system of semaphore relay, which is regarded as optical telegraph was demonstrated in France by Claude Chappe in 1792 [2]. This semaphore relay was a mechanical system. Along with the industrial revolution, the electrical telegraph system was invented by Samuel Morse. Followed with the telegraph, one milestone of telecommunication is the invention of telephone by Alexander Graham Bell in 1876. To enable transmission over long distance, first underwater coaxial cable was deployed in Australia between Apollo Bay and Stanley, and first trans-Atlantic coaxial cable TAT-1 was deployed in 1956 as shown in Table 1.1. However, the intrinsic characteristics of the conventional transmission medium including copper wires and coaxial cables pose the limitations of low bandwidth and high cost.

In 1960s, techniques of lasers were developed rapidly. The first working laser with the wavelength of 694 nm was developed by T. Maiman at Hughes Research Labs in 1960, and the first semiconductor laser diode working at 850 nm was demonstrated by R. Hall's team in 1962. The development of lasers triggered the usage of lightwave to carry information, in other words, the evolution of semiconductor laser technologies paved the way for optical communication. To support the lightwave, namely, optical signals, the optical fiber is a promising choice. Compared with the conventional communication medium such as copper wires, optical fiber possesses several key

merits such as wide bandwidth, and cost-effectiveness due to the abundant resource of raw material. To enable optical fiber an appropriate transmission medium for the lightwave, the insertion loss of the fiber is a major concern. In 1966, one milestone work of developing low-loss optical fiber was accomplished by Charles K. Kao and G. Hockham [3]. The insertion loss of the optical fiber per kilometer was reduced to be lower than 20 dB at that time by Corning [4]. This record of fiber loss is constantly being refreshed along with the new techniques. Nowadays, at the wavelength of 1550 nm, the insertion loss of standard single mode fiber is generally lower than 0.2 dB/km. The low insertion loss enables the optical fiber an appropriate medium for long-haul transmission systems [4].

Table 1.1 Trans-Atlantic telephone cable (TAT)

Year	Cable	Type	Capacity
1956	TAT-1	Galvanic	36 channels
1959	TAT-2	Galvanic	48 channels
1963	TAT-3	Galvanic	138 channels
1965	TAT-4	Galvanic	138 channels
1970	TAT-5	Galvanic	845 channels
1976	TAT-6	Galvanic	4000 channels
1978	TAT-7	Galvanic	4000 channels
1988	TAT-8	Fiber-optic	40000 channels
1992	TAT-9	Fiber-optic	80000 channels
1992	TAT-10	Fiber-optic	2×565 Mbit/s
1993	TAT-11	Fiber-optic	2×565 Mbit/s
1996	TAT-12/13	Fiber-optic	12×2.5 Gbit/s
2001	TAT-14	Fiber-optic	3.2 Tbit/s

Thanks to the low transmission loss, in 1988 the first trans-Atlantic fiber-optic cable was demonstrated to carry 40000 voice channels, with the bit rate of 280 Mb/s.

Given that the optical fiber possesses the wide bandwidth, to further improve the capacity, the wave division multiplexing (WDM) was proposed. The first commercial WDM system was in the region of 1.3 μm & 1.5 μm, and the bit rate of this system can reach 3.4 Gb/s. Although the low insertion loss of the transmission medium (e.g., the optical fiber) is highly desirable for short-reach transports, to elongate the transmission distance, an effective approach to boost the light power is indispensable for long-haul transmission. Among various optical amplifiers, the semiconductor optical amplifier (SOA) is advantageous in terms of the small size, easy integration with other semiconductor devices, and the wide wavelength region of amplification. Both Raman amplifiers and Erbium-doped fiber amplifiers (EDFAs), however, are fiber-based optical amplifiers. Compared with Raman amplifiers, EDFAs can provide relatively large optical gain, although EDFAs only amplify C- or L-band signals. Since optical amplifiers inevitably introduce amplified spontaneous emission (ASE) noise while amplifying desired signals, low noise figure is preferable while designing the long-haul transmission system.

1.2. Motivations for field recovery via direct detection

The recent decade has witnessed the explosive advent of cloud computing, data center networks, and people have easier access to the multimedia applications such as TikTok, YouTube, high-definition videos, and high-fidelity sound quality music. In 2010 the number of connected devices per person is merely 1.84, while after ten years this number increases to 6.58 [5]. Besides, it is predicted that machine-to-machine (M2M) connections would rise from 33% to 50% in next five years, corresponding to 14.7 billion connections of M2M in 2023 [6]. These data-hungry applications drive the need for the high-capacity data traffic [7]. In the past centuries, due to the low cost of optical fiber and the development of optical communication technologies, telecommunication products using the transmission medium of optical fibers have already been extensively exploited and widely implemented. Furthermore, in the modern fiber-optic transmission systems, the digital signal processing (DSP) for both direct detection and coherent detection enables the superior system performance [8-10]. Direct detection, due to the simple structure, has been a promising solution for

price sensitive transmission links. The direct detection based transmission system generally consists of a directly modulated laser, optical fibers, and a single-ended photodiode (PD). Due to the square-law detection of the PD, only intensity information can be obtained from the detected photocurrent, and hence the transmitted signal in the conventional direct detection is commonly intensity modulated signal, which corresponds to intensity modulation with direct detection (IMDD) [11]. One major limitation for the IMDD system is the nonnegligible chromatic dispersion in the window of 1550 nm. Since the phase information is lost in the intensity-only detection schemes, chromatic dispersion cannot be digitally compensated. As such, IMDD systems are commonly implemented in short-reach applications, given that chromatic dispersion is linear to the transmission distance. Though the window of 1310 nm can provide negligible chromatic dispersion, the fiber loss in this region poses the limitation for the medium-reach optical networks [12-14], such as inter-data center networks. For the connectivity between data centers, the transmission distance can be up to several spans of optical fiber [15-16], and currently commercialized IMDD products can hardly realize such reach. However, the coherent receiver is still extravagant for such medium-reach application scenarios, due to the hardware and DSP complexity.

To cope with the high-capacity data traffic driven by various cloud services, massive optical transceivers are in demand in the warehouse-scale data centers [17]. As such, primary concerns for the data center interconnect (DCI) are twofold: achieve high capacity, meanwhile, the cost-effectiveness cannot be sacrificed [18]. To achieve the high data rate, in-phase/quadrature (IQ) modulation is preferable since it provides two dimensions of modulation, while intensity modulation merely has one degree of freedom. Regarding the cost, direct detection is a favourable solution for the receiver structure. To explore the possibility of direct detection system for such medium-haul links, chromatic dispersion compensation is indispensable to elongate the transmission distance, and hence the recovery of field information is required.

To recover complex-valued signals via direct detection, an optical carrier is needed to obtain the signal-carrier beating term. Due to the square-law detection of the PD,

the distortion term of signal-signal beat interference (SSBI) is inevitable [19]. Consequently, the mitigation of SSBI is a major task for the field recovery via direct detection. Though when the carrier power is sufficiently large, the SSBI distortions can be ignored compared with the signal-carrier beating term. The carrier does not carry any information and hence it is essentially not power-efficient. To deal with SSBI, one approach is retaining the frequency gap between the optical carrier and modulated signals, and the bandwidth of the gap should be wide enough to accommodate SSBI, for example, the bandwidth of the gap equals to that of information-bearing signals [20]. Similarly, for OFDM signals the even-numbered subcarriers can be set to null and the signals are only loaded to the odd-numbered subcarriers [21], as such after square-law detection, the SSBI would only exist on the null even-numbered subcarriers. Nevertheless, these two approaches waste the electrical spectral efficiency, as the required receiver bandwidth is generally twice of the signal bandwidth. To enhance the spectral efficiency, the frequency gap between the carrier and signals is removed, and various algorithms of mitigating SSBI were proposed. For example, single-stage linearization and iterative cancellation schemes were proposed and effective SSBI mitigation was demonstrated. Besides, Kramers-Kronig (KK) relations were investigated to show the ability to recover the phase of signals using detected intensity information [22]. Although single sideband (SSB) modulation is adopted for the KK receiver, it doubles the spectral efficiency compared with the approach using frequency gap. As such, it can be concluded that pursuing the high spectral efficiency is the trend. Furthermore, it is expected to develop a direct detection system scheme which can be applied for double sideband (DSB) modulation. In this way, the high electrical spectral efficiency is achieved, and accordingly, the requirement of receiver bandwidth is relaxed, which leads to the cost reduction.

In brief, the receiver schemes supporting the field recovery of SSB and DSB signals via direct detection are major research contents in this thesis. For the SSBI which extensively exists in direct detection, algorithms of SSBI mitigation are studied. Besides, although the carrier is generally required to be sufficiently strong to obtain the desired signal-carrier beating term, it is preferable to load more power on information-bearing signals rather than the carrier. Hence, it is highly desirable to

develop the algorithms to reduce the required carrier power, which is another focus of this thesis.

1.3. Thesis outline

The structure of this thesis is as follows:

Chapter 1 introduces the evolution of fiber-optic communication, and the merits of optical fiber over conventional cables are covered. The data traffic demand for high-capacity optic-fiber based transports such as DCIs which can be up to several hundred kilometers is discussed. The necessity of field recovery for such medium-reach transmission links is explained, and the motivation of exploring direct detection rather than coherent detection to achieve the field recovery is given.

Chapter 2 is the literature review. The generation of intensity modulated signals, optical SSB signals, and DSB signals is introduced first, including the working principle of directly modulated lasers (DMLs), electro-absorption modulated lasers (EMLs), and Mach-Zehnder modulators (MZMs). Then the conventional direct detection system and coherent receiver structure with the respective working principles are presented. The techniques of self-coherent system are also covered in this chapter. Finally, various proposed algorithms to deal with SSBI are reviewed.

Chapter 3 focuses on the field recovery of SSB signals via direct detection. The working principles of KK receiver and SSBI iterative cancellation (IC) receiver are explicated. The modulation formats, for example single- and multi-carrier modulation, for KK and IC receivers are investigated and compared. To verify the capability of field recovery using KK and IC receivers, CD is digitally compensated at the receiver side, and system performance of these two receivers is simulated and experimentally demonstrated. Chromatic dispersion impacts on both receiver schemes are studied. Besides, the polarization mode dispersion (PMD) impacts are also covered in this chapter.

Chapter 4 focuses on the field recovery of DSB signals via direct detection. The motivation of turning to DSB modulation is explained first. After illustrating the

receiver structure of carrier assisted differential detection (CADD), the algorithms of recovering complex-valued DSB signals are presented. Several key parameters for the CADD receiver are thoroughly discussed and via simulation the corresponding optimization of optical delay, CSPR along with the frequency gap is conducted. First-time experimental demonstration of CADD receiver is covered in this chapter. Finally, since IQ modulator is implemented in the CADD system, IQ imbalance impacts including amplitude and phase imbalance are investigated.

Chapter 5 focuses on the reduction of the required carrier power, namely, relaxation of the high carrier-to-signal power ratio (CSPR) requirement for both SSB and DSB based direct detection systems with field recovery. One approach for SSB signal field recovery system is the hybrid of KK and SSBI iterative cancellation, which is proposed to mitigate SSBI more effectively at low CSPRs, namely, reduce the required CSPR. Another approach to reduce the required optical carrier power for SSB direct detection system is the virtual CSPR enhancement scheme. For the DSB based direct detection system, a simple but effective power loading scheme is proposed to reduce the carrier power for CADD receiver.

Chapter 6 summarizes the key findings of this thesis, and proposes the direction of further optimization and work related to the field recovery via direct detection.

1.4. Contributions

The contributions of this thesis are as follows:

Chapter 3 We investigate modulation formats for the KK and IC receiver. Single carrier modulation is found to be superior to multi-carrier modulation for the KK receiver, and this phenomenon is due to the high peak-to-average power ratio (PAPR) of multi-carrier signals. For the IC receiver, OFDM signals outperform single-carrier signals. Experimental demonstration is carried out to study the CD impacts on the KK and IC receiver. The IC receiver is shown to be robust to CD, while KK receiver requires the high CSPR to be insensitive to CD. For the short- to medium-reach application scenarios, the first-order PMD impacts are found to be negligible for the KK receiver.

Chapter 4 Based on the receiver scheme called CADD, we propose the algorithm of complex-valued DSB signal field recovery and conduct the simulation of CADD receiver. Besides, the first-time transmission system using CADD receiver is presented in this chapter. To be specific, in order to enhance the spectral efficiency of CADD receiver, the frequency gap with small frequency gap is preferred. To strike the balance between system performance and frequency gap, the joint optimization of the optical delay line length, the bandwidth of frequency gap, and the CSPR for the CADD receiver has been conducted. Correspondingly, a guidance for designing the CADD receiver is provided according to simulation results. For the first-time experimental demonstration, signal transmission over 160-km standard single-mode fiber (SSMF) has been conducted to verify the capability of field recovery for DSB signals. Besides the receiver side, one practical issue of IQ imbalance for the CADD scheme is theoretically investigated, and results show that the IQ imbalance degrades the system performance as a whole, while the processing of SSBI cancellation alone does not bring in extra optical signal-to-noise ratio (OSNR) penalty in the presence of IQ imbalance.

Chapter 5 We propose three novel algorithms to enable more power loaded on modulated signals rather than the carrier. For the SSB based schemes, enhanced SSBI mitigation is proposed to effectively reduce the optimal CSPR by 2-3 dB. Besides, another approach called virtual CSPR enhancement scheme is able to increase the CSPR at the receiver side, and hence the required power of the carrier transmitted over the fiber can be reduced. For the DSB based CADD system, a simple but effective power loading scheme is demonstrated to be effective to help make more accurate symbol decisions. Accordingly, the requirement of high carrier power for CADD at the transmitter side is relaxed.

1.5. Publications

1. C. Sun, T. Ji, H. Ji, Z. Xu, and W. Shieh, “Experimental demonstration of complex-valued DSB signal field recovery via direct detection,” *IEEE Photonics Technology Letters*, vol. 32, no. 10, pp. 585-588, May. 2020.

2. C. Sun, D. Che, H. Ji, and W. Shieh, “Investigation of single- and multi-carrier modulation formats for Kramers-Kronig and SSBI iterative cancellation receivers,” *Optics Letters*, vol. 44, no. 7, pp. 1785-1788, Apr. 2019.

3. C. Sun, D. Che, H. Ji, and W. Shieh, “Study of chromatic dispersion impacts on Kramers-Kronig and SSBI iterative cancellation receiver,” *IEEE Photonics Technology Letters*, vol. 31, no. 4, pp. 303-306, Jan. 2019.

4. C. Sun, H. Ji, T. Ji, Z. Xu, and W. Shieh, “Power loading for carrier assisted differential detection,” Asia Communications and Photonics Conference (ACP) 2020, paper M3B.4.

5. C. Sun, H. Ji, T. Ji, Z. Xu, and W. Shieh, “Impacts of IQ imbalance on carrier assisted direct detection,” Pacific Rim Conference on Lasers and Electro-Optics (CLEO-PR 2020), paper 4F.6.

6. C. Sun, D. Che, H. Ji, and W. Shieh, “Virtual carrier-to-signal power ratio enhancement for Kramers-Kronig receivers,” European Conference on Optical Communication (ECOC) 2019, paper Tu.1.D.3.

7. C. Sun, D. Che, H. Ji, and W. Shieh, “Towards low carrier-to-signal power ratio for Kramers-Kronig receiver,” Optical Fiber Communication Conference (OFC) 2019, paper M1H. 6.

8. C. Sun, D. Che, and W. Shieh, “Comparison of chromatic dispersion sensitivity between Kramers-Kronig and SSBI iterative cancellation receiver,” Optical Fiber Communication Conference (OFC) 2018, paper W4E. 4.

9. C. Sun, D. Che, R. Schmid, and W. Shieh, “Polarization mode dispersion impacts on Kramers-Kronig receiver,” Optoelectronics and Communications Conference (OECC) 2018, paper 4B4-3.

W. Shieh, C. Sun, and H. Ji, “Carrier-assisted differential detection,” *Light: Science & Applications*, vol. 9, no. 1, pp. 1–9, Feb. 2020 is also related to this thesis, and the contributions of each author in this publication are claimed in the Preface.

Chapter 2 Basic principle and literature review

2.1. Introduction

Driven by various applications and services such as Internet of things (IoT) and cloud computing, the era of fifth-generation (5G) mobile network has arrived [23-26]. 5G is expected to provide the ultra-fast internet with low latency and improved reliability. For short-reach optic-fiber transports, the conventional IMDD system is a cost-effective solution and the corresponding products have been widely implemented [27-28]. The transmitted signals in IMDD systems are limited to one degree of modulation, namely, only the amplitude of the signal is modulated. To support the networks with ever-increasing data rate, the dimension of modulation freedom has attracted much research interests. For optical signals, four dimensions can be modulated: intensity, phase, frequency, and polarization [29]. Out of the four dimensions, the amplitude-only intensity modulation is the simplest one, and one typical example is pulse amplitude modulation (PAM), which is widely adopted in the passive optical network (PON) [30-33]. Beyond that, both in-phase and quadrature components can be independently modulated for the IQ modulation, corresponding to the quadrature amplitude modulation (QAM). High order IQ modulation has been extensively investigated in the recent years [34-38], and the state-of-the-art progress is up to 16384 QAM [39]. Furthermore, one intrinsic characteristic of the optical fiber is that two polarization states are accommodated. As such, the system capacity can be doubled via polarization multiplexing [40]. Generally, coherent receivers are implemented to detect the dual-polarization signals. For the conventional coherent receiver, the local oscillator is required at the receiver side, which distinguishes from the direct detection. Besides the single-mode fiber (SMF), multi-mode fiber (MMF) serves as an approach to increase the capacity via more than one mode [41]. To further enhance the system capacity, WDM was proposed to take the advantage of the wide bandwidth of the fiber [42-44]. In optic-fiber systems, the system bandwidth is commonly determined by the opto-electronic and electronic devices, and whether the

cost of the high-speed electronic devices is comparable to the choice of multiple channels consisting of relatively low-speed devices is a concern. Correspondingly, the WDM scheme provides a promising compromise between single channel with high-speed components and multiple channels with low-speed components. Furthermore, WDM systems can rapidly realize high capacity by fully utilizing C and O bands for the medium and long-haul transmission [45-46].

As discussed above, besides the data rate, the transmission distance is another key parameter while designing the optic-fiber system. For the long-haul transmission, the cost of coherent receiver with the complicated structure can be amortized by the long distance. While for the intensity-only direct detection, it is worth noting that the CD is linear to the transmission distance, and CD induced power fading hinders the transmission reach of the IMDD system [47-49]. In contrast, the coherent detection can recover the field, which enables digital CD compensation at the receiver side, and hence enables long-haul transmission [8][50]. Besides, due to the utilization of the local oscillator the receiver sensitivity of coherent detection is commonly superior to that of direct detection. In this chapter, the transmitters for direct and coherent detection are discussed, and the generation of optical SSB signals will be thoroughly studied. To bridge the gap between conventional direct and coherent detection, self-coherent systems are of great necessity to be reviewed. Finally, various proposed SSBI mitigation schemes to deal with second-order distortions which commonly exist in direct detection systems are reviewed.

2.2. Optical signal generation for optic-fiber transmission

To transmit information-bearing signals over optical fibers, baseband electrical signals need to be converted to the optical signals. This mapping procedure can be either linear or nonlinear depending on the characteristics of lasers and modulators at the transmitter side. According to the application scenarios, either IMDD or coherent systems can be adopted. To construct a transmitter for the optic-fiber system, some widely used modulators include DML, EML, and MZM [51-52]. The optical signal

generation schemes using corresponding modulators are discussed in the following sections.

2.2.1. Intensity modulation using DML

DMLs have been widely implemented for short- to medium-reach transmission links due to the simple structure and low cost compared to external modulators [53-55]. Although distributed feedback (DFB) laser diodes are commonly used for DMLs, Fabry-Perot (FP) laser diodes and vertical cavity surface emitting lasers (VCSELs) can also enable direct modulation [56]. The FP laser has an active region at the center and

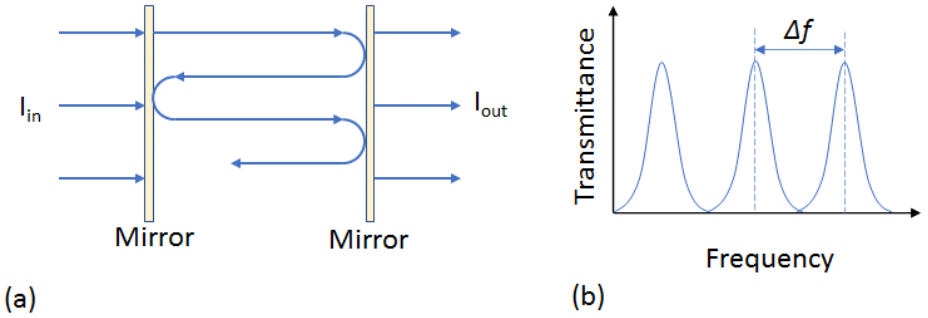

Fig. 2.1(a) Fabry-Perot optical cavity. (b) Transmittance as a function of frequency.

two parallel mirrors on both sides, and accordingly, this structure is also called Fabry Perot resonator as shown in Fig. 2.1(a). The transmittance of the Fabry-Perot cavity can be described using the following equation

$$I_{out} = I_{in} \frac{(1-R)^2}{(1-R)^2 + 4R\sin^2(4\pi nL/\lambda)} \tag{2.1}$$

where I_{out} and I_{in} denote the output and input currents, respectively, n denotes the refractive index inside the cavity, L denotes the length of the cavity, the reflectance of the cavity facets is represented by R, and λ is the wavelength. The resonator can only support certain wavelengths, and each of them serves as a standing wave. It can be derived from Eq.(2.1) that the frequency difference Δf between two standing waves is a function of the refractive index and the cavity length

$$\Delta f = \frac{c}{2nL} \tag{2.2}$$

where c denotes the velocity of light. The active region gain helps to shape the power of each Fabry-Perot mode, and eventually only several lasing modes with gain larger than loss can survive. As such, FP lasers generate many longitudinal modes, and result in relatively large spectral width. Although FP laser can provide relatively large optical power and small divergence angle, the multi-mode characteristic is not favorable for optic-fiber communication.

To obtain single-longitudinal mode outputs, DFB lasers can be utilized. The built-in Bragg grating features the DFB lasers as shown in Fig. 2.2. The selective

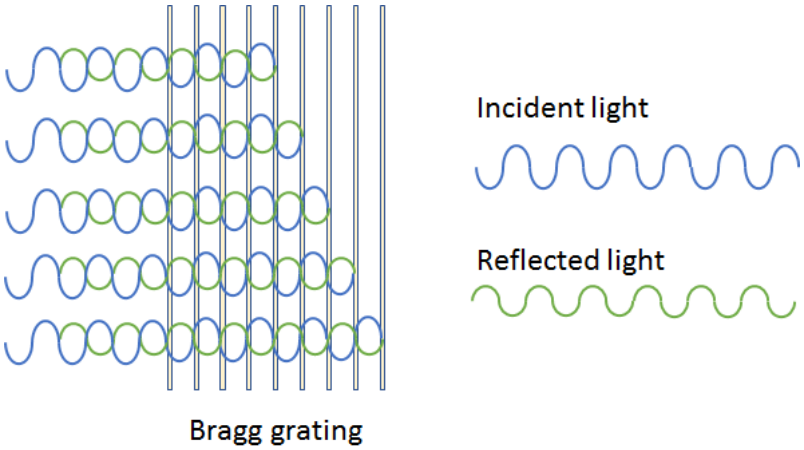

Fig. 2.2 Operation principle of DFB laser diode.

wavelength satisfies the following condition

$$\Lambda_B = \frac{m\lambda}{2\bar{n}} \tag{2.3}$$

where m is the order of Bragg diffraction, and the effective refractive index is represented by $\bar{n}$ [9]. One merit of the DFB laser is the linearity, which is highly desirable for upconverting the baseband signal. As shown in Fig. 2.3 [57], the bias current is much higher than the threshold current, and from the perspective of four-level (PAM-4) modulation the mapping processing is almost linear, though with some distortions mainly due to the limited bandwidth of the DFB laser. As such, PAM-4 optical signals can be obtained shown in the inset (ii) of Fig. 2.3. Other intensity modulated baseband signals such as on-off keying (OOK), duobinary, and multi-level PAM can be approximately linearly mapped to the optical intensity with the linear

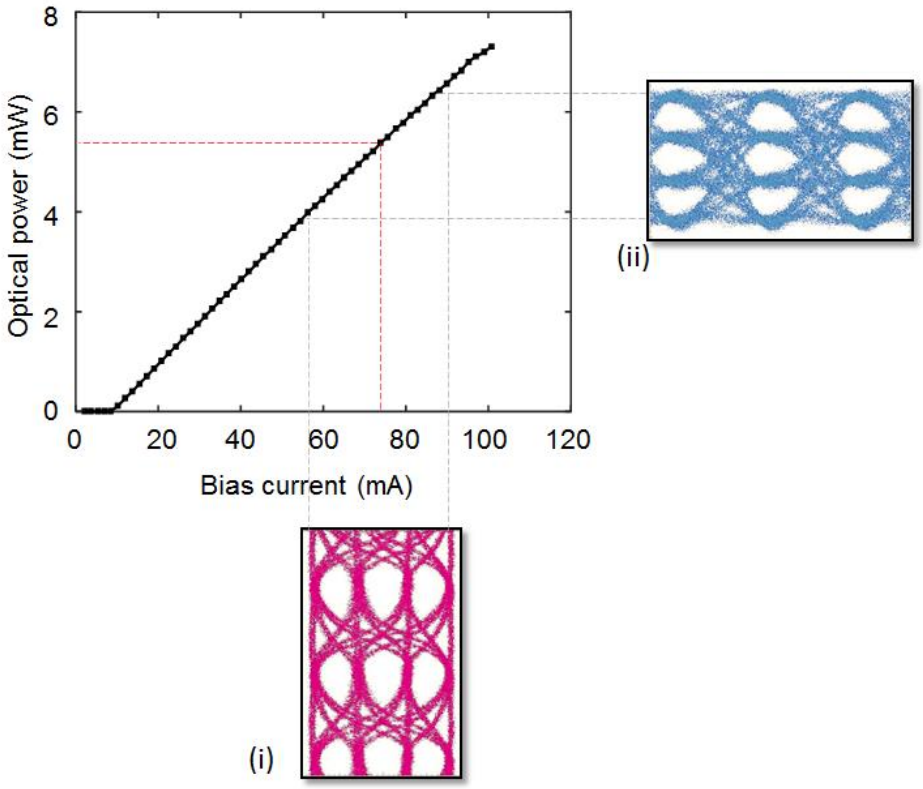

Fig. 2.3 Measured optical power vs bias current curve of a DML. Insets(i) and (ii) are the eye diagrams of electrical and optical PAM-4 signals, respectively.

optical power vs bias current curve of such DMLs. However, the frequency chirp is one of the common limitations for DMLs. The frequency chirp is induced by the injected current, which could change the refractive index of the active region, leading to the wavelength drift, which is generally a detrimental factor for DMLs. The frequency chirp including both transient and adiabatic chirp can be described using the following equation [58]

$$\Delta f = \frac{\alpha}{4\pi}\{\frac{d}{dt}[\ln P(t) + \kappa P(t)]\} \tag{2.4}$$

where α is the laser linewidth enhancement factor, κ denotes the adiabatic chirp coefficient, and P(t) represents the laser output power [59].

Besides FP and DFB laser diodes, the VCSEL can serve as a DML. DFB lasers generally can provide high output power, and the L-I curve is linear, which is highly desirable for the multi-level intensity modulation. In contrast, the linearity of the

VCSEL is poor, and the output power of one single VCSEL is relatively low. However, different from the DFB laser, VCSEL can emit light from the top surface, which enables the on-wafer testing. Furthermore, the characteristic of emitting light in the vertical direction of the surface facilitates two-dimensional array, which contributes to high power and reliability. Although the manufacturing techniques of VCSELs have been mature, VCSELs are relatively difficult to fabricate long-wavelength devices. Accordingly, VCSELs are preferable for the short-reach O-band optic-fiber transmission links from the perspective of wavelength [60-62]. For both DFB lasers and VCSELs temperature control is one solution to obtain constant wavelength or optical power. Generally, as the temperature increases, the optical power decreases with the threshold current rises. Given that DFB lasers and VCSELs are sensitive to the temperature, the thermoelectric cooler (TEC) is commonly implemented to stabilize the temperature for the DMLs, although the TEC is not favorable for compact products.

2.2.2. Intensity modulation using EML

Electro-absorption modulator (EAM) is a semiconductor-based optical modulator, and it can be integrated with other semiconductor devices [14]. To construct the transmitter for the optic-fiber transmission system, a laser source is required besides the EAM. When EAM is integrated with light source such as DFB lasers, the integrated product is called EML. The integrated DFB laser is biased at one certain point to obtain a continuous wave mode, and the baseband signals are modulated by applying a voltage onto the EAM, as such, the modulated optical signals are generated using EML. Since EML separates the functions of the laser source and modulator, the limited bandwidth of DMLs is alleviated, and the adiabatic chirp does not apply for the EML, only transient chirp exists for the EML. Consequently, the EML based system is a promising solution of the high-capacity C-band applications. Since the frequency chirp of EML is alleviated compared to DMLs, the EML tolerates more CD impacts. However, the corresponding trade-off is that the insertion loss of the modulator is not negligible due to the characteristic of electro-absorption (e.g., around 10 dB), and hence the output optical power of the EML is relatively low. Besides, the linearity of

the EML is generally not as good as DFB based DMLs, for example, the transmittance of the EAM is not a linear function of injected electric voltage. Regarding the practical product, the EAM can be manufactured using multi-quantum-well structure to pursue the compact size.

2.2.3. Intensity modulation using dual-drive MZM

Although the EAM is an external modulator, the transient chirp is inevitable and broadens the signal spectrum, which limits the EAM to be implemented for the long-haul transmission. To realize intensity modulation without the detrimental chirp impacts, MZM is extensively studied and demonstrated [4,9].

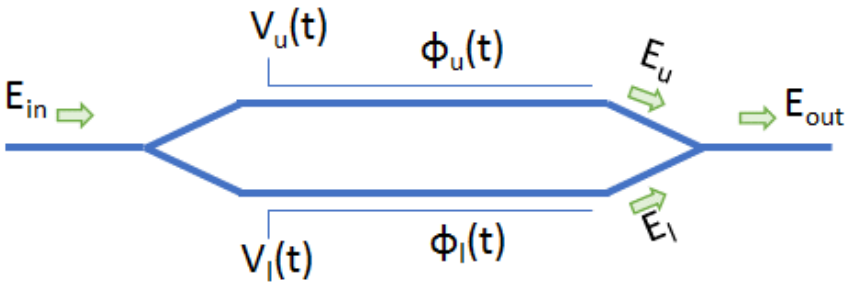

Fig. 2.4 Conceptual structure of a dual-drive Mache-Zander modulator.

The conceptual structure of a dual-drive MZM is shown in Fig. 2.4. The input light is split into two paths, which are upper and lower waveguides. The input optical signal is denoted by E_{in}, $V_u(t)$ and $V_l(t)$ are the applied RF signals on upper and lower arms, respectively. The phase delay of $\phi_u(t)$ and $\phi_l(t)$ induced by the driving voltages can be expressed as follows

$$\phi_u(t) = \eta V_u(t), \qquad \phi_l(t) = \eta V_l(t) \tag{2.5}$$

where η is proportional to the electro optic coefficient. As such, the optical signals on the upper and lower arms E_u and E_l can be written as

$$E_u = \frac{E_{in}}{2}\exp(j\phi_u), \qquad E_l = \frac{E_{in}}{2}\exp(j\phi_l) \tag{2.6}$$

At the output of the MZM, signals on the upper and lower arms are combined, which can be denoted by E_{out}

$$\begin{aligned} E_{out} &= \frac{E_{in}}{2}\exp(j\phi_u) + \frac{E_{in}}{2}\exp(j\phi_l) \\ &= E_{in}\cos(\frac{\phi_u - \phi_l}{2})\exp(j\frac{\phi_u + \phi_l}{2}) \end{aligned} \tag{2.7}$$

For intensity modulation, it is worthwhile to derive the output intensity I_{out} rather than end up with E_{out}, and I_{out} is given by

$$\begin{aligned} I_{out} \propto |E_{out}|^2 &= \frac{|E_{in}|^2}{2}\{1+\cos(\phi_u - \phi_l)\} \\ &= \frac{I_{in}}{2}\{1+\cos(\eta V_u - \eta V_l)\} \end{aligned} \tag{2.8}$$

The transmittance of the MZM is defined as the ratio between I_{out} and I_{in}, and the voltage difference between the applied voltages on the upper and lower arms is denoted by V, namely, $V = V_u - V_l$. As such, the phase and the transmittance are illustrated in Fig. 2.5.

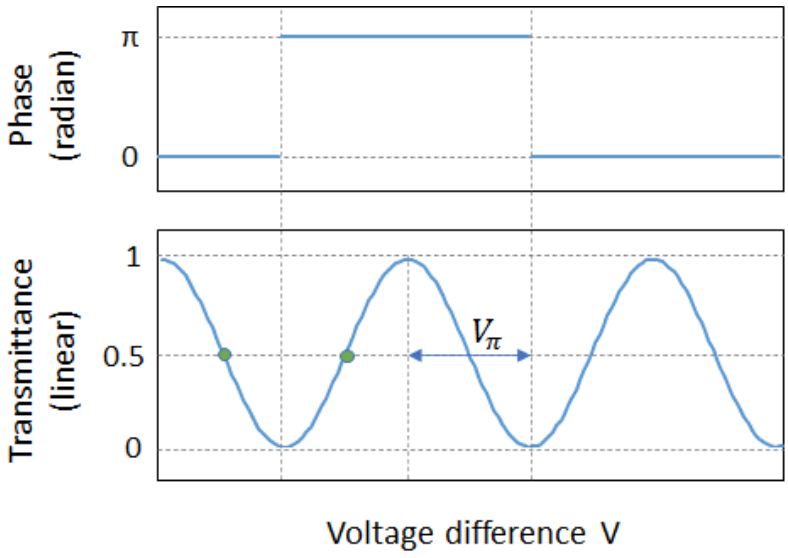

Fig. 2.5 Power transfer function of an MZM.

When the MZM works in push-pull operation, the applied voltages satisfy $V_u = -V_l = V$, and the Eq. (2.7) can be rewritten as $E_{out} = E_{in}\cos(\eta V)$. The green solid

points shown in the transmittance curve of Fig. 2.5 are quadrature points. For intensity modulation, the MZM is generally biased at the quadrature point since the vicinity of the quadrature point is relatively linear, and hence the intensity-modulated signals can be linearly mapped onto the optical field. At the quadrature bias point, the transmittance is 0.5, corresponding to at least 3-dB insertion loss. The switching voltage V_π is shown in Fig. 2.5, which represents the half period of the transmittance curve. The value of the switching voltage typically ranges from 3 to 8 volts, as such, the MZM requires relatively large driving voltages, and electrical amplifiers are needed to drive the modulated signals. The principal axis of the MZM is defined by the principal axis of the electro-optic crystal, and hence a polarization controller is commonly implemented for the MZM to ensure that the polarization state of incident light coincides with the principal axis of the electro-optic crystal [63].

2.2.4. IQ modulation using coherent IQ MZM

Based on the basic structure of dual-drive MZM shown in Fig. 2.4, the coherent IQ modulator is depicted in Fig. 2.6 [8]. Each of two MZMs works as an intensity modulator, which enables the separate amplitude modulation. As such, the applied data

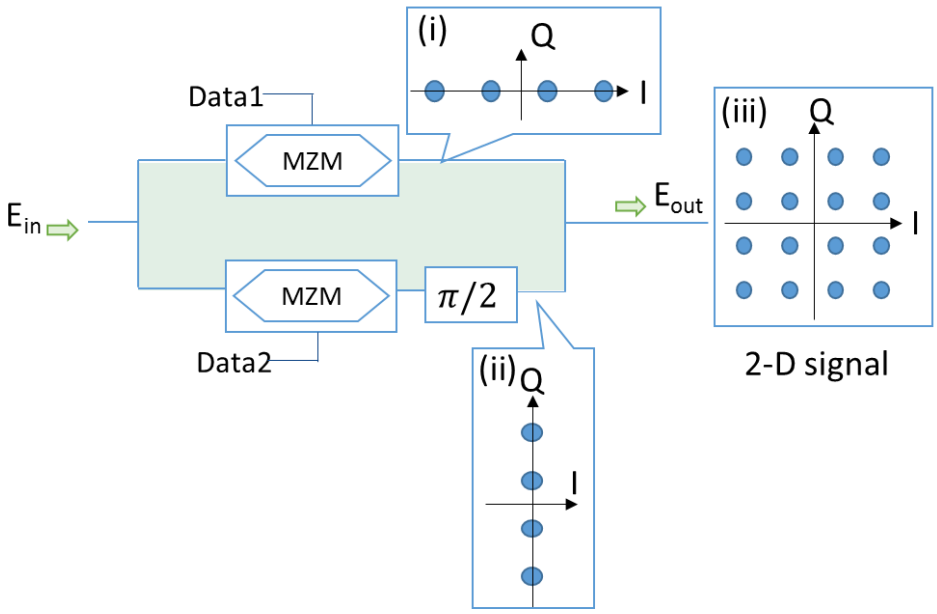

Fig. 2.6 Conceptual structure of a coherent IQ modulator. Insets (i) and (ii) are the in-phase and quadrature modulated PAM-4 signals, and inset (iii) presents the corresponding constellation of QAM 16 signals.

on each arm is separately modulated amplitude signal, for example, PAM-4 signals shown in the inset(i) of Fig. 2.6. With the aid of one 90-degree optical phase shifter, the signals on the lower arm are orthogonal to the signals loaded on the upper arm. When these two arms are combined, the output of the two combined PAM signals becomes IQ modulated signals, as shown in the inset (iii) of Fig. 2.6.

For intensity modulation, the transfer function is defined as the intensity ratio I_{out}/I_{in}, while for IQ modulation, it is reasonable to choose E_{out}/E_{in} as the transfer function. From Eq. (2.7), the transfer function can be expressed as

$$E_{out} / E_{in} \propto \cos(\eta V) \tag{2.9}$$

Analogous to the dual-drive intensity MZM modulator, the transfer function of a coherent IQ modulator is depicted in Fig. 2.7.

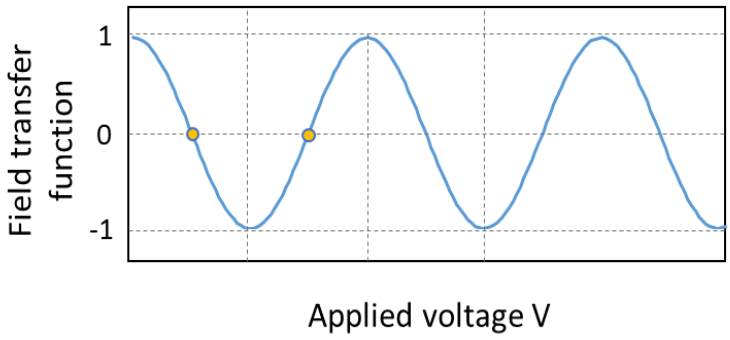

Fig. 2.7 Field transfer function of the coherent IQ modulator.

The generally used bias points for the coherent IQ modulator are marked in Fig. 2.7. It is worth noting that the bias point for the coherent IQ modulator is the null point, where the transmittance equals to zero, while the bias point for the intensity dual-drive MZM is the quadrature point. That is because in the vicinity of the null point, the transfer function of a coherent IQ modulator is approximately linear. Compared with intensity modulation, IQ modulation provides one more dimension to modulate, and hence increases the system capacity. The corresponding trade-off is that such external modulators including the dual-drive MZM and IQ modulators are generally bulky in size and the insertion loss is larger than that of DMLs. Accordingly, the IQ modulator

is suitable for the long-haul transmission systems. Besides, to further increase the system capacity, dual polarizations can be exploited. The dual-pol MZM consists of two coherent IQ modulators shown in Fig. 2.6 and one polarization beam combiner (PBC).

2.2.5. Optical SSB signal generation

The real-valued RF signal is generally DSB, when the DSB signal is mapped into the optical domain the modulated optical signal has two sidebands, with the optical carrier in the center. After transmission over the fiber, the CD introduces different phase shift on two sidebands. Since the two sidebands are conjugate symmetric, after square-law detection of a single-ended PD we can observe destructive cancellation at some certain frequencies, and the destructive frequency f_d can be expressed as [64]

$$f_d = \sqrt{\frac{2n+1}{2}} \cdot \sqrt{\frac{c}{\lambda^2 DL}} \qquad n = 0,1,2... \tag{2.10}$$

where c denotes the light speed, λ denotes the wavelength, D is the chromatic dispersion parameter, which is generally 17 ps/nm/km for the SSMF in the C window, and L is the transmission distance. As transmission distance increases, more destructive frequencies can be observed within the signal spectrum, leading to severe distortions. As such, conventional DSB-based IMDD systems suffer from the spectral power fading, and thus hinders the product of transmission reach and data rate [65-67].

One of the promising solutions to deal with the power fading issue is SSB modulation. Since the information carried on two sidebands of the real-valued signals is redundant, either upper or lower sideband can be removed. The merits of adopting SSB modulation are twofold: (i) the CD induced power fading is avoided, and the transmission distance can be elongated for the DD system [68]; (ii) optical spectral efficiency is enhanced, which is favorable for the WDM system. Consequently, it is highly desirable to discuss various schemes of SSB signal generation.

To realize the SSB modulation, one sideband of DSB signals can be suppressed either electrically or optically. Via Hilbert transform DSB baseband signals can be transformed to SSB signals. For the real-valued baseband signal $m(t)$, in the

frequency domain the corresponding upper and lower sidebands are denoted by $M_u(f)$ and $M_l(f)$, which are given by

$$\begin{aligned} M_u(f) &= \frac{1}{2}M(f)[1+sign(f)] \\ M_l(f) &= \frac{1}{2}M(f)[1-sign(f)] \end{aligned} \tag{2.11}$$

where $sign(f)$ is the sign function. It is defined that $M_h(f) = M(f) \cdot [-jsign(f)]$, as such, the Eq. (2.11) can be rewritten as

$$\begin{aligned} M_u(f) &= \frac{1}{2}[M(f)+jM_h(f)] \\ M_l(f) &= \frac{1}{2}[M(f)-jM_h(f)] \end{aligned} \tag{2.12}$$

The Hilbert transform $H(f)$ can be extracted from the definition of $M_h(f)$

$$H(f) = -jsign(f) = \begin{cases} -j & (f \geq 0) \\ j & (f < 0) \end{cases} \tag{2.13}$$

The Hilbert transform can be regarded as a phase shifter, since it does not change the amplitude of signals, and only introduces 90° phase shift. The amplitude and phase responses are illustrated as follows

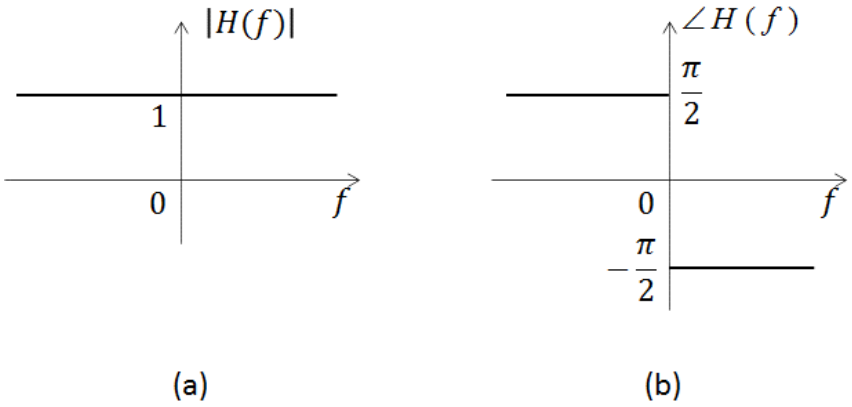

Fig. 2.8 (a) Amplitude response of the Hilbert transform. (b) Phase response of the Hilbert transform.

As such, by utilizing Hilbert transform the phase of upper sideband signals is delayed by 90°, and the phase of lower sideband signals is expedited by 90°. Eq. (2.13) can be

substituted into Eq. (2.11), after implementing inverse Fourier transformation in the time domain upper and lower sideband signals are given by

$$\begin{aligned} m_u(t) &= \frac{1}{2}[m(t) + jm_h(t)] \\ m_l(t) &= \frac{1}{2}[m(t) - jm_h(t)] \end{aligned} \tag{2.14}$$

where $m_h(t)$ denotes the phase-shifted baseband signals, namely, the Hilbert transform of the baseband signals [69]. When the baseband signals and the corresponding Hilbert transformation are summed as shown in Eq. (2.14), one sideband can be suppressed. Correspondingly, the modulated upper and lower SSB signals (e.g., s_{USB} and s_{LSB}) in the time domain can be expressed as

$$\begin{aligned} s_{USB}(t) &= m(t)\cos(\omega_c t) - m_h(t)\sin(\omega_c t) \\ s_{LSB}(t) &= m(t)\cos(\omega_c t) + m_h(t)\sin(\omega_c t) \end{aligned} \tag{2.15}$$

where ω_c is the carrier frequency. Such processing can be conducted electrically, and the SSB signals are fed into a coherent IQ modulator to accomplish the optical SSB signal generation.

Analogous to the electrical SSB signal generation approach, the Hilbert transform can be implemented in the optical manner. The generation of SSB signals using optical Hilbert transformer is shown in Fig. 2.9 [70]. The input of the structure shown in Fig. 2.9 is DSB signals, and an optical coupler is used to split signals into two paths. The upper path serves as the in-phase dimension. In the lower path one 90-degree phase shifter and an optical Hilbert transformer (OHT) are implemented. The corresponding spectra are illustrated in Fig. 2.9, revealing that in the lower path the phase of upper sideband signals is shifted by 180 degree, with no phase change for the lower sideband signals. The sum of I and Q components shown in Fig. 2.9 forms the SSB modulation, with the upper sideband suppressed and lower sideband unchanged. For the practical implementation, the OHT can be realized by the fiber Bragg grating (FBG) [66][71-72].

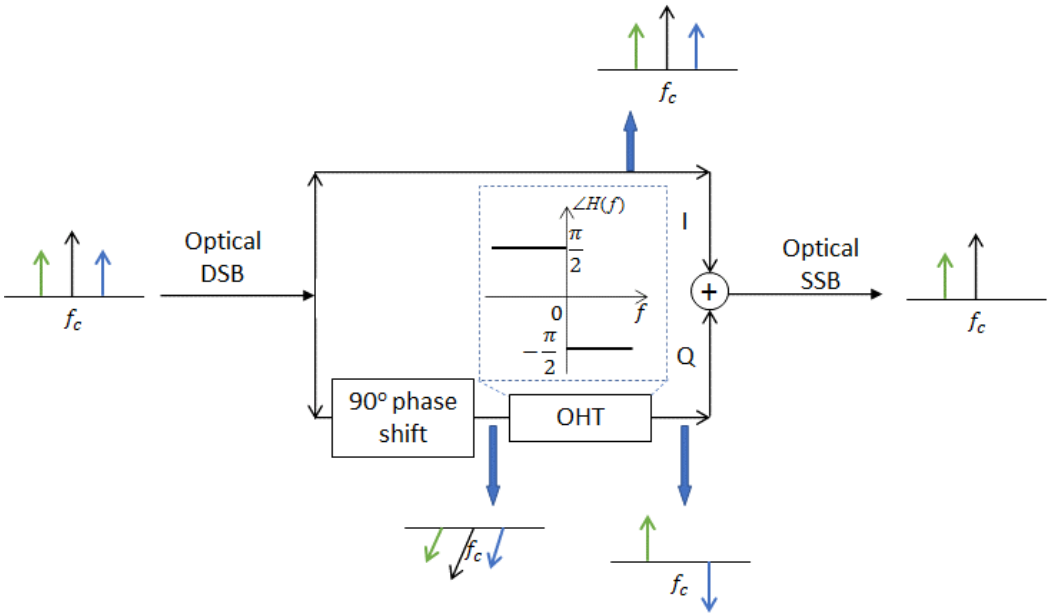

Fig. 2.9 SSB signal generation and the corresponding spectra using optical Hilbert transformer.

The scheme of OHT can be categorized into the phase shift approach, besides, the optical SSB can be obtained via selective filtering method, in other words, using an optical filter to suppress one sideband of DSB signals. However, it requires the optical filter to have a flat transmittance region and sharp cutoff frequency [73].

For the field recovery via direct detection, an optical carrier is commonly implemented to obtain the beating term between the signal and the carrier, namely, the replica of the information-bearing signal. As such, one alternative method to generate SSB signals is inserting the optical carrier at one side of the modulated signals. Fig. 2.10 shows three transmitter schemes to generate the carrier assisted SSB signals. For the first scheme shown in Fig. 2.10 (a), digitally generated SSB signals are fed into a coherent IQ modulator with the bias point above the null point, as such, the optical carrier is obtained and the CSPR can be varied via tuning the bias point. Some medium- to long-haul transmission systems using the transmitter scheme as shown in Fig. 2.10 (a) have been demonstrated, the transmission distance of C-band 112-Gb/s SSB signals was reported to be 960 km over SSMF [74]. For WDM systems, 800-Gb/s (8×100 Gb/s) SSB signals have been transmitted up to 320 km [75], and 5 × 240 Gb/s

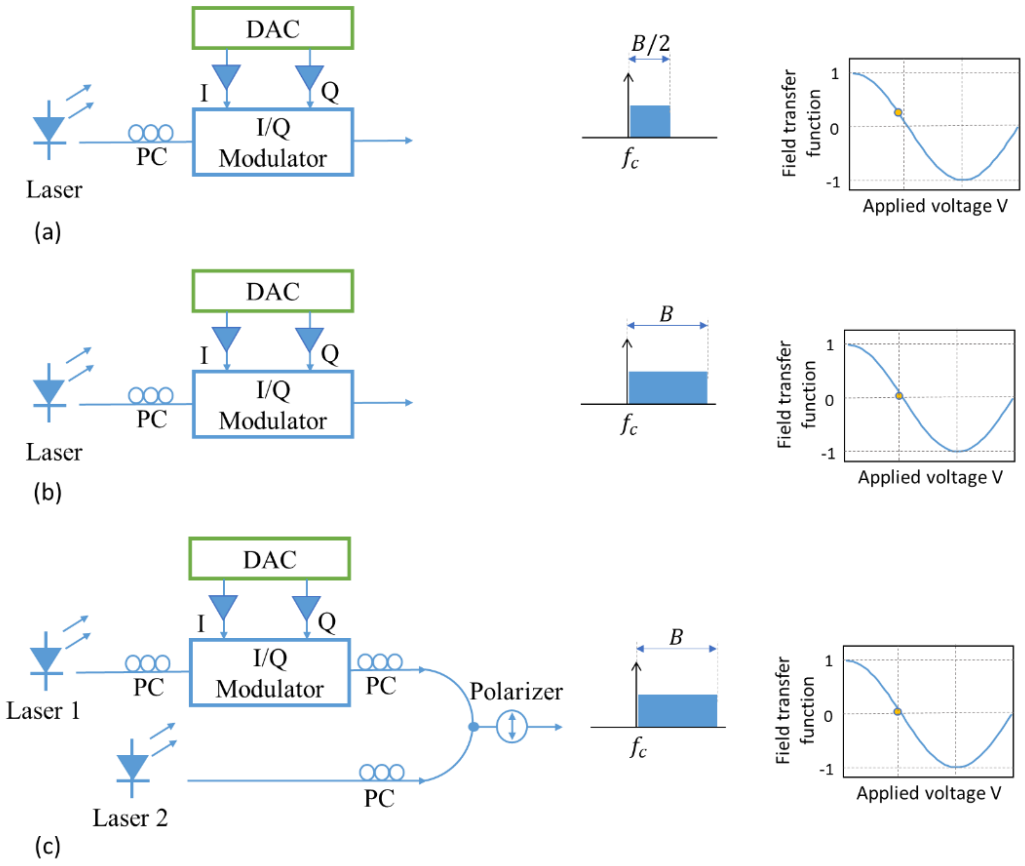

Fig. 2.10 Transmitter schemes for carrier assisted SSB signal generation with the corresponding spectra and bias points. DAC: digital to analog converter. PC: polarization controller.

signal transmission over 80-km SSMF has been reported with the spectral efficiency of 5.25 bit/s/Hz [76]. However, the bandwidth of the digital to analog converter (DAC) is wasted by half due to the SSB modulation. The transmitter scheme shown in Fig. 2.10(b) can fully take the advantage of the DAC bandwidth. The bias point of the IQ modulator is null point, and the carrier along with the information-bearing signals are digitally generated and then fed into the IQ modulator. Generally, the optical carrier power is much larger than the signal power. When both carrier and signals are generated using the DAC, the resolution of DAC is relatively sacrificed. Accordingly, the transmitter scheme shown in Fig. 2.10 (c) was proposed. The continuous wave (CW) from a second laser serves as the optical carrier, and there exists a frequency shift of B/2 with respect to the wavelength of laser 1. An optical coupler can be implemented to combine information-bearing signals and the carrier from two paths.

A polarizer is utilized to guarantee the polarization state of signals and the carrier is coincident. Although neither the bandwidth nor the resolution of DAC is sacrificed, the implementation of one more laser is the limitation for cost-sensitive direct detection systems. One alternative solution to replace the extra laser is employing a frequency shifter [77], while it requires another modulator to shift the carrier frequency.

Beyond the generation of SSB signal at the transmitter side, one state-of-the-art scheme is detecting one sideband of PAM signals at the receiver side [78]. In other words, the SSB signals are obtained via the bandwidth-limited PD. Since two sidebands of PAM signals are Hermitian symmetric, one missing sideband due to the limited bandwidth can be reconstructed via the residual sideband, which provides a novel direction of obtaining SSB signals.

2.3. Receiver for optical transmission systems

The key feature to distinguish direct and coherent detection is whether a local oscillator is implemented at the receiver. Conventionally, the direct detection is accompanied with intensity modulation, while coherent detection enables IQ modulation. In recent years, with the development of advanced DSP the capability of direct detection is increasing rapidly and becoming comparable to coherent detection. Before reviewing the up-to-date DSP techniques, it is highly desirable to elaborate the fundamentals of conventional direct and coherent detection.

2.3.1. Direct detection

Due to its simple and cost-effective structure, direct detection has been widely implemented in the short-reach transmission link [79-84]. The conventional and most basic receiver using direct detection consists of a PD and an analog to digital converter (ADC). The PD is an essential component to convert optical signals into electrical ones. To be specific, the PD senses the luminescent power falling upon it and converts the varying optical power into the corresponding electrical current, namely, detected photocurrent. As such, the PD follows square-law detection, and the direct detection intrinsically fits for the intensity modulation, which corresponds to the IMDD system. IMDD system has been widely employed in PON, where the receiver sensitivity is a

proper metric to determine how many users can be supported [85-89]. Accordingly, the origins of noise and the noise power are worthy of attention.

Two types of dominating noises for the PD are shot and thermal noise. The shot noise is induced by the quantum properties of photons. Shot noise follows Poisson statistics, and hence shot noise is also called Poisson noise. The variance of the shot noise σ_s^2 is shown in Eq. (2.16)

$$\sigma_s^2 = 2qI \cdot \Delta f \tag{2.16}$$

where I is the photocurrent, q is the electric charge, which equals to 1.6×10^{-19} C, and Δf denotes the bandwidth [90]. The thermal noise, also known as Johnson or Nyquist noise, generates from the agitation of mobile carriers in resistive electrical materials. The thermal noise exists even when no external electrical power source is applied, since the thermal agitation of carriers happens at finite temperatures. Different from the shot noise, thermal noise is demonstrated to possess a flat power spectral density over a THz-magnitude frequency region, which is regarded to be white. As such, the thermal noise follows Gaussian statistics. Eq. (2.17) presents the variance of the thermal noise σ_{th}^2

$$\sigma_{th}^2 = \frac{4k_B T \cdot \Delta f}{R_L} \tag{2.17}$$

where k_B denotes the Boltzmann constant, which equals to 1.38×10^{-23} J/K, T is the temperature, and R_L denotes the load resistor [90]. The noise figure, defined as at the standard noise temperature the ratio of output noise power to the thermal noise power at the input termination, is therefore related to the thermal noise, and the noise figure is presented hereafter.

Two main types of PDs are PIN and avalanche photodiode (APD) [91]. The structure of a PIN is simple, and it is essentially a p-n junction diode with the reverse bias. The receiver sensitivity of the PIN, however, is poor due to the limited output photocurrent, and hence a transimpedance amplifier (TIA) is generally integrated with

the PIN to enhance the photocurrent. To identify the noise power impacts, the signal-to-noise ratio (SNR) of a PIN is given by

$$SNR_{PIN} = \frac{R^2 P_{in}^2}{2qRP_{in}\Delta f + 4k_B TF_n \Delta f / R_L} \approx \frac{R^2 P_{in}^2 R_L}{4k_B TF_n \Delta f} \tag{2.18}$$

where R is the responsivity of the PD, P_{in} denotes the input power, F_n is the amplifier noise factor. Since the thermal noise is commonly the dominating noise for the PIN, the SNR expression can be approximated shown in Eq. (2.18). For the APD, it is also a reverse-biased p-n junction diode, while compared with the PIN, APD possesses the internal current gain R, leading to the better receiver sensitivity. The SNR of the APD is given by

$$SNR_{APD} = \frac{(MR)^2 P_{in}^2}{2qM^{2+x} RP_{in}\Delta f + 4k_B TF_n \Delta f / R_L} \approx \frac{RP_{in}}{2qM^x \Delta f} \tag{2.19}$$

where M^x is the excess noise factor and x denotes the coefficient which depends on the structure and material. The receiver sensitivity of APD is generally limited by the shot noise rather than the thermal noise, the corresponding approximation is presented in Eq. (2.19) [92].

2.3.2. Coherent detection

Distinguish from the direct detection, the coherent receiver is capable of the phase recovery, and hence not only supports M-ary phase-shift keying and QAM modulation,

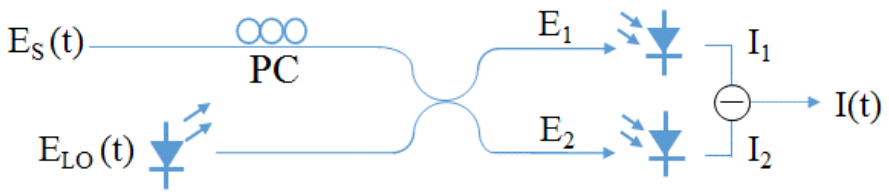

Fig. 2.11 A basic coherent receiver structure. PC: polarization controller.

but also enables the compensation of various linear impairments including the group-velocity dispersion (GVD) and PMD [8]. Compared with the direct detection, the structure of a coherent receiver is complicated partially due to the implementation of the local oscillator (LO). A basic coherent receiver structure is depicted in Fig. 2.11, where the electric field of the transmitted signal and LO are denoted by $E_s(t)$ and $E_{LO}(t)$, respectively. With the notation of the corresponding amplitude, angular frequency, and phase of the signals and LO, $A_s(t)$, ω_s, θ_s, and $A_{LO}(t)$, ω_{LO}, θ_{LO}, the electrical fields can be expressed as

$$\begin{aligned} E_s(t) &= A_s(t)\exp(j\omega_s t + \theta_s) \\ E_{LO}(t) &= A_{LO}(t)\exp(j\omega_{LO} t + \theta_{LO}) \end{aligned} \tag{2.20}$$

For the simplicity, the power of signal P_s and LO P_{LO} is written as

$$\begin{aligned} P_s &= |A_s|^2 / 2 \\ P_{LO} &= |A_{LO}|^2 / 2 \end{aligned} \tag{2.21}$$

With the aid of a polarization controller (PC), the state of polarization of transmitted signals are in line with that of LO. After a 3-dB optical coupler, without considering the insertion loss, two electric fields E_1 and E_2 fed into the PDs are given by

$$\begin{aligned} E_1 &= \frac{1}{\sqrt{2}}(E_s + E_{LO}) \\ E_2 &= \frac{1}{\sqrt{2}}(E_s - E_{LO}) \end{aligned} \tag{2.22}$$

As such, the photocurrents I_1 and I_2 given by two PDs can be expressed as

$$\begin{aligned} I_1 &= \frac{R}{2}[P_s + P_{LO} + 2\sqrt{P_s P_{LO}}\cos(\omega_{IF} t + \theta_s - \theta_{LO})] \\ I_2 &= \frac{R}{2}[P_s + P_{LO} - 2\sqrt{P_s P_{LO}}\cos(\omega_{IF} t + \theta_s - \theta_{LO})] \end{aligned} \tag{2.23}$$

where R is the responsivity, and $\omega_{IF} = \omega_s - \omega_{LO}$. Two PDs shown in Fig. 2.11 work as a balanced PD (BPD), and the output photocurrent of such a balanced PD is given by

$$
\begin{aligned}
I(t) &= I_1 - I_2 \\
&= 2R\sqrt{P_s P_{LO}}\cos(\omega_{IF}t + \theta_s - \theta_{LO})
\end{aligned}
\tag{2.24}
$$

For the heterodyne detection, $|\omega_{IF}| \gg 2\pi/T$ where T denotes the symbol duration, namely, ω_{IF} needs to be much larger than the modulation bandwidth of the signal. To detect single-polarized IQ modulated signals, the heterodyne detection using one BPD as shown in Fig. 2.11 is sufficient, however, it requires the receiver bandwidth to be larger than ω_{IF} plus modulated signal bandwidth, which is at least twice of modulated signal bandwidth. For the homodyne detection, $\omega_{IF} = 0$, and one BPD is not capable to recover the full field of IQ modulated signals. Another LO path with 90° phase shift is needed for the phase-diversity homodyne receiver as shown in Fig. 2.12.

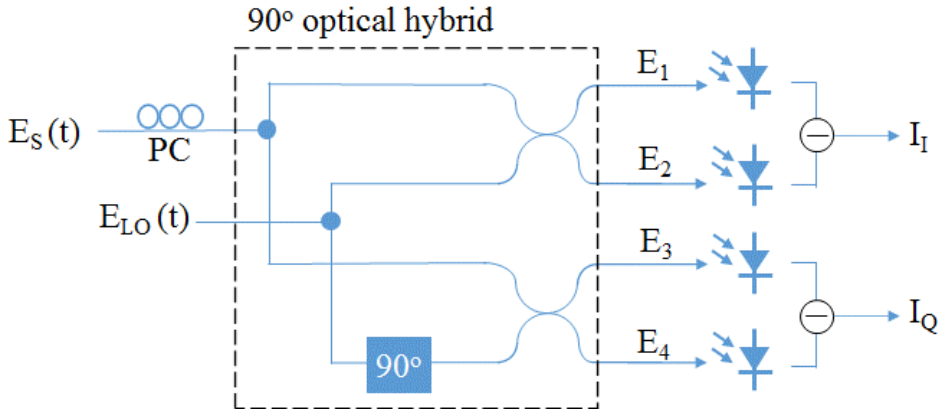

Fig. 2.12 Structure of a phase-diversity homodyne receiver using a 90-degree optical hybrid.

The 90° optical hybrid has two inputs and four outputs, and the four outputs can be expressed as

$$
\begin{aligned}
E_1(t) &= \frac{1}{2}\{E_s(t) + E_{LO}(t)\} \\
E_2(t) &= \frac{1}{2}\{E_s(t) - E_{LO}(t)\} \\
E_3(t) &= \frac{1}{2}\{E_s(t) + jE_{LO}(t)\} \\
E_4(t) &= \frac{1}{2}\{E_s(t) - jE_{LO}(t)\}
\end{aligned}
\tag{2.25}
$$

Two photocurrents I_I and I_Q detected by a pair of BPD are given by

$$I_I(t) = R\sqrt{P_s P_{LO}}\cos\{\theta_s(t) - \theta_{LO}(t)\}$$
$$I_Q(t) = R\sqrt{P_s P_{LO}}\sin\{\theta_s(t) - \theta_{LO}(t)\} \quad (2.26)$$

As such, signals can be reconstructed via

$$I(t) = I_I(t) + jI_Q(t) \quad (2.27)$$

The phase noise shown in Eq. (2.26) can be estimated and compensated using various DSP techniques, correspondingly, both in-phase and quadrature components of the optical field are extracted. It is also worth noting that the conceptual diagram shown in Fig. 2.12 can be updated for detecting dual-polarization signals. One key merit of the homodyne over heterodyne receiver is that homodyne receiver can relax the required bandwidth of the electronics circuits by one half [8][93]. The corresponding cost is that the frequency of LO needs to strictly track the frequency shift of the laser at the transmitter [94], plus the number of required PDs is doubled.

2.4. Self-coherent system

The utilization of LO at the receiver enables coherent detection to extract the full field of signals, and hence elongate the transmission distance with the aid of DSP. However, the LO with the narrow linewidth at the receiver not only increases the overall system cost, but also introduces the carrier phase and state of polarization alignment issues. To deal with these two issues and relax the requirement of hardware, the LO is waived and the CW tone analogous to the LO is generated at the transmitter side, corresponding to the self-coherent system [95-96]. The advantages of such self-coherent system are twofold: first, one laser serving as the LO in conventional coherent detection is saved, and second, co-polarized CW can be simply generated at the transmitter.

Correspondingly, the CW is generated using the same laser as the modulated signals, and the CW, namely, the carrier is denoted by C, and S presents the modulated signal field. In this way, the phase mismatch between the carrier and signals which exists in the conventional coherent systems is avoided. At the receiver of such a self-

coherent scheme, after square-law detection of a single-ended PD, the detected photocurrent I is given by

$$\begin{aligned} I &= \left|C+S\right|^2 \\ &= \left|C\right|^2 + \left|S\right|^2 + 2\,\mathrm{Re}[C^* \cdot S] \end{aligned} \tag{2.28}$$

where the responsivity of the single-ended PD is assumed to be 1 for simplicity, Re[] represents the real part of a complex value, and superscript * stands for the conjugation function. The first term of the right-hand side of Eq. (2.28) is the DC term, which can be simply removed, the second term is SSBI which is the second-order distortion. The SSBI distortion extensively exists in self-coherent systems, as such, the accommodation and mitigation of SSBI is a significant focus in this thesis. The last term $2Re[C^*S]$ is the linear replica of modulated signals, which is the desired term to recover the optical field of signals.

To investigate the capacity or the data rate R of self-coherent systems, Shannon's formula is introduced [97]

$$\begin{aligned} R &= \alpha B \log_2(1+SNR) \\ &= \alpha B \log_2(1+\frac{\beta_1}{\beta_2}\frac{OSNR}{1+CSPR}\frac{B_{ref}}{B}) \end{aligned} \tag{2.29}$$

where α denotes the coefficient due to the polarization multiplexing, and α equals to 2 for polarization-division multiplexed signals, for other schemes α is not larger than 1. B is the required bandwidth of ADC, and the expression of SNR can be further derived as shown in Eq. (2.29), where B_{ref} commonly equals to 12.5 GHz, which is the OSNR reference bandwidth. β_1 is the coefficient of signal power, which equals to 2 for single-polarization signals, and equals to 1 for dual-polarization signals. β_2 is the factor related to noise mitigation scheme [97-98]. It can be noted that for a certain OSNR, a large CSPR would reduce the data rate, in other words, the high CSPR is a limitation for the high-capacity systems. Besides, the bandwidth of frequency gap, namely, the bandwidth of the guard band between the carrier and the information-bearing signal is another factor to affect the required receiver bandwidth.

Correspondingly, SSBI mitigation at low CSPRs with low requirement of receiver bandwidth is the pursuit of this thesis.

2.5. Techniques of SSBI mitigation

The continuous growth of data center applications drives the investigation of short-reach transmission systems [99 - 101]. In the recent years, the fiber-optic transmission system is regarded as a promising solution for the inter- or intra-data center interconnects, which are generally up to several hundreds of kilometers transmission. In fact, fiber-optic transmission links using direct detection have already been widely employed for such price-sensitive application scenarios. Compared with conventional coherent receiver, the simple structure and cost-effectiveness of the direct detection enables it to be the choice for short-reach links [102-105]. The direct detection was initially proposed to detect the amplitude of the modulated signals, and hence intrinsically fits for the intensity modulation [106-108]. Despite the fact that IMDD system is one of the choices for the short-reach transports, to keep up with the capacity of the next-generation high-speed requirements, intensity modulation has the limitation of one modulation dimension and hence it hinders IMDD system to upgrade the capacity. Furthermore, the transmission distance is commonly up to tens of kilometers for IMDD systems, as the optical field cannot be extracted from the intensity-only direct detection and CD impairments are not resilient to be compensated. As such, self-coherent schemes which are capable of recovering the optical field was extensively studied in the recent decade. As shown in Eq. (2.28), SSBI is inherently involved in the detected photocurrent, and this section will thoroughly introduce various proposed SSBI accommodation and mitigation algorithms.

In terms of modulation formats, the field recovery via direct detection can be categorized into SSB and DSB. However, SSBI distortions commonly exist for both SSB and DSB signals. To deal with second-order distortions for SSB based direct detection, SSBI can be accommodated or mitigated using a frequency gap [109-110], and the corresponding spectra are shown in Fig. 2.13 (a) (b). Besides, one extra optical

path, or one extra polarization along with the DSP techniques can serve as a solution to deal with SSBI.

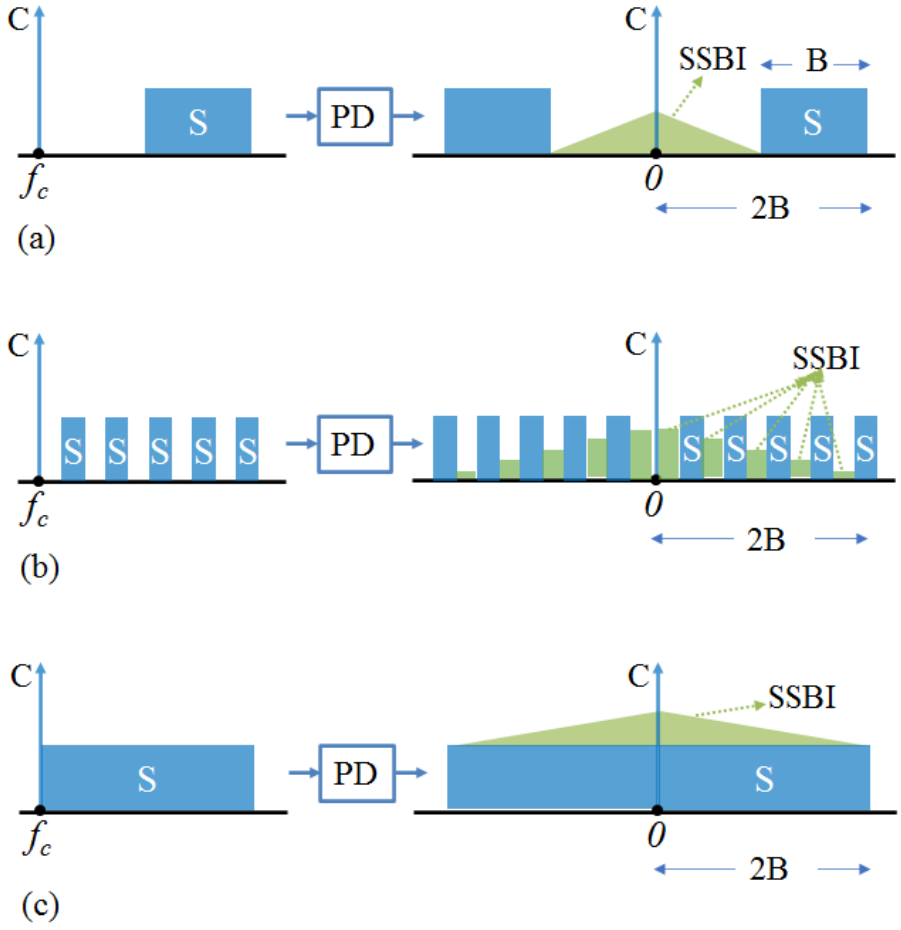

Fig. 2.13 Spectra of SSB signal with (a) guard band (b) interleaved loading (c) no frequency gap before and after direct detection.

For the SSB signal direct detection scheme, one effective approach is inserting the guard band between the carrier and modulated signals to accommodate SSBI. OFDM signals are chosen to present the spectrum of SSBI. As shown in Fig. 2.13 (a), for the OFDM signals with N subcarriers, half of the subcarriers are loaded with information and the other half are unfilled. As such, the modulated signals are in the frequency region of $[\omega_{N/2}, \omega_N]$, while the bandwidth of guard band is same as the bandwidth of modulated signals, corresponding to $[0, \omega_{N/2}]$. In this way, the modulated signals S can be written as

$$S = \sum_{i=N/2}^{N} E_i \exp[j(\omega_i + \omega_c)t] \tag{2.30}$$

where ω_i and ω_c denote the frequencies of the i-th subcarrier and optical carrier, respectively. Consequently, the photocurrent detected by the single-ended PD shown in Eq. (2.28) can be further expressed as

$$\begin{aligned} I = |C|^2 + \sum_{i=N/2}^{N} E_i \exp(j\omega_i t) \cdot \sum_{i=N/2}^{N} E_i^* \exp(-j\omega_i t) \\ + C\sum_{i=N/2}^{N} E_i \exp(j\omega_i t) + C\sum_{i=N/2}^{N} E_i^* \exp(-j\omega_i t) \end{aligned} \tag{2.31}$$

The second term at the right-hand side of the Eq. (2.31) is SSBI. It can be seen that SSBI occupies the frequency region of $[-\omega_{N/2}, \omega_{N/2}]$, and the replica of information-bearing signals are the third and fourth term of the Eq. (2.31). Correspondingly, the modulated signals and SSBI are separated in the frequency domain. The bandwidth of the guard band is needed to be the same as information-bearing signal bandwidth to sufficiently accommodate SSBI. Namely, to detect the information-bearing signal with the bandwidth of B, it requires the receiver bandwidth to be 2B. Furthermore, considering SSBI is more severe at low frequency region rather than the high frequency counterpart as depicted in Fig. 2.13 (a), some compromise can be made to enhance the spectral efficiency, for example, the bandwidth of guard band is 2/3 of the information-bearing signal bandwidth to accommodate most of the SSBI distortions [111]. Similarly, the wide guard band can be divided into each subcarrier of the OFDM signals. As depicted in Fig. 2.13(b), for OFDM signals only odd-numbered subcarriers are loaded and even-number subcarriers are null, such OFDM signals can be expressed as $\sum_{i=0}^{N} E_{2i+1} \exp[i(\omega_{2i+1} + \omega_c)t]$. The photocurrent I shown in Eq. (2.28) is given by

$$\begin{aligned} I = |C|^2 + \sum_{i=0}^{N} E_{2i+1} \exp(j\omega_{2i+1} t) \cdot \sum_{i=0}^{N} E_{2i+1}^* \exp(-j\omega_{2i+1} t) \\ + C\sum_{i=0}^{N} E_{2i+1} \exp(j\omega_{2i+1} t) + C\sum_{i=0}^{N} E_{2i+1}^* \exp(-j\omega_{2i+1} t) \end{aligned} \tag{2.32}$$

Different from the SSBI presented in Eq. (2.31), SSBI for the interleaved OFDM signals are located in the even-numbered subcarriers, and hence information-bearing signals are free from SSBI distortions. The interleaved loading approach possesses the same spectral efficiency as the guard band approach, and both of these two approaches

sacrifice the spectral efficiency to accommodate SSBI. Besides, the interleaved scheme was demonstrated to tolerate more nonlinear effects than the scheme shown in Fig. 2.13 (a), and this phenomenon was attributed to the large subcarrier spacing induced suppression of four wave mixing (FWM) [21].

To enhance the spectral efficiency, SSBI accommodation which sacrifices receiver bandwidth can be updated to SSBI mitigation with no guard band or interleaved loading. As depicted in Fig. 2.13 (c), the frequency gap between the carrier and modulated signals is negligible, and SSBI contamination is overlapped with signals in the frequency domain. As such, two methods to recover the signals are (i) enhancing linear replica of signals, (ii) removing SSBI distortions from signals. For the first method, the CSPR needs to be sufficiently high to weaken distortions, in other words, using a strong carrier C to enhance the last term of Eq. (2.28), as such, the second term of Eq. (2.28) SSBI is not comparable to the desired term. The required CSPR is 15 dB in the demonstration of OFDM signal direct detection [112]. For the second method which is estimation and mitigation of SSBI, the requirement of high CSPR can be correspondingly alleviated. Several promising algorithms were proposed to deal with SSBI impacts. One simple scheme is the single-stage linearization as depicted in Fig. 2.14. Since the detected signals are DSB due to the square-law detection, one sideband

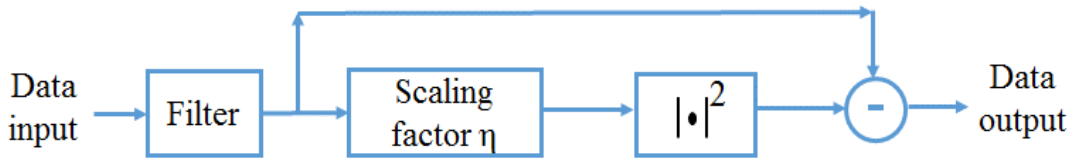

Fig. 2.14 DSP flow chart for the single-stage linearization.

filter is implemented to shape received DSB into SSB signals. One path of the corresponding DSP flow chart is scaled SSB signals are fed into the square-law function to reconstruct SSBI, and then subtracted from the shaped signals. To be specific, the corresponding formulas are given as follows, and the signals after the filter are denoted as E_F

$$E_F = E_s + L[|E_s|^2] \tag{2.33}$$

where E_s represents the modulated signals, and $L[\cdot]$ is the sideband filter function. The output signal E_{out} after the subtraction shown in Fig. 2.14 can be expressed as

$$\begin{aligned} E_{out} &= E_F - \eta \left| E_F \right|^2 \\ &= E_s + L[\left| E_s \right|^2] - \eta \left| E_s \right|^2 - 2\eta \,\mathrm{Re}[E_s^* \cdot L[\left| E_s \right|^2]] - \eta \left| L[\left| E_s \right|^2] \right|^2 \end{aligned} \tag{2.34}$$

where η is the scaling factor shown in Fig. 2.14. The first term on the right-hand side of Eq. (2.34) is the desired term, the second and third terms are SSBI. One sideband of SSBI can be mitigated via tuning the scaling factor η. The rest terms are high-order distortions, which are believed to be relatively small. Based on single-stage linearization, two-stage linearization scheme [113] was proposed to deal with the signal-SSBI beating term (e.g., the fourth term on the right-hand side of Eq. (2.34)). Furthermore, the estimation and subtraction of SSBI can be employed several times to enhance the accuracy, as such, the iterative linearization scheme was proposed. It is worth mentioning that symbol decisions are not made in the above discussed methods.

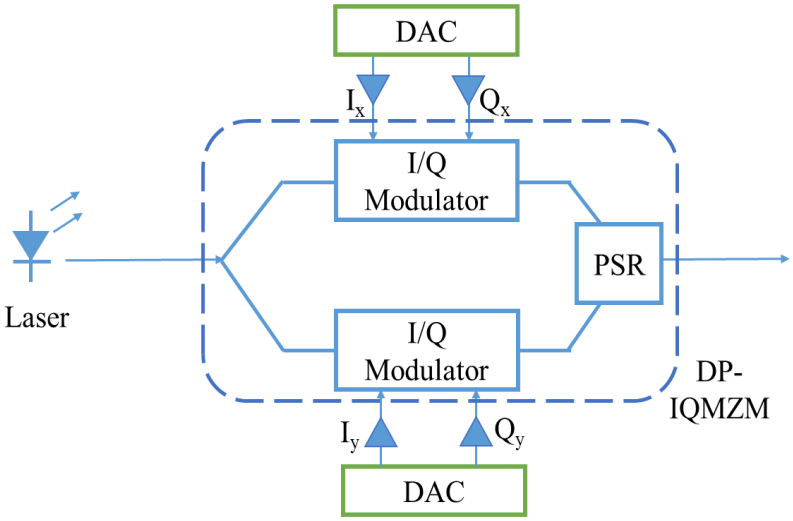

Fig. 2.15 Transmitter structure of optical SSBI mitigation scheme.

Beyond the above-mentioned DSP, SSBI can also be mitigated optically. One novel approach is taking the advantage of polarization, and the corresponding transmitter structure is illustrated in Fig. 2.15 [114], where the dotted box presents a DP-IQMZM, and PCs are not shown for the concise illustration. The SSBI mitigation is conducted optically at the transmitter side. Specifically, the information-bearing

signals and carrier are loaded on x polarization, denoted as $E_{x,sig}$ and $E_{x,c}$, respectively. The field of x and y polarization represented by E_x and E_y are given by

$$\begin{aligned} E_x &= E_{x,sig} + E_{x,c} \\ E_y &= \sqrt{\left|E_{y,c}\right|^2 - \left|E_{x,sig}\right|^2} \end{aligned} \tag{2.35}$$

The photocurrent can be expressed as

$$\begin{aligned} I &= \left|E_x\right|^2 + \left|E_y\right|^2 \\ &= 2\,\mathrm{Re}(E_x E_{x,c}^*) + \left|E_{x,c}\right|^2 + \left|E_{y,c}\right|^2 \end{aligned} \tag{2.36}$$

As shown in Eq. (2.36), the components in the detected photocurrent are the replica of information-bearing signals and two DC terms $\left|E_{x,c}\right|^2$, $\left|E_{y,c}\right|^2$. It can be found that the SSBI term is mitigated with the aid of well-designed y-pol signals while being fed into a single-ended PD.

Besides the mitigation scheme at the transmitter, SSBI can be cancelled optically at the receiver side [115-116]. The receiver structure is depicted in Fig. 2.16, with corresponding spectra presented. Transmitted signals are information-bearing SSB signals along with the carrier. One 3-dB optical coupler provides two paths, with one path fed into a single-ended PD (e.g., illustrated as PD1 in Fig. 2.16), and another path

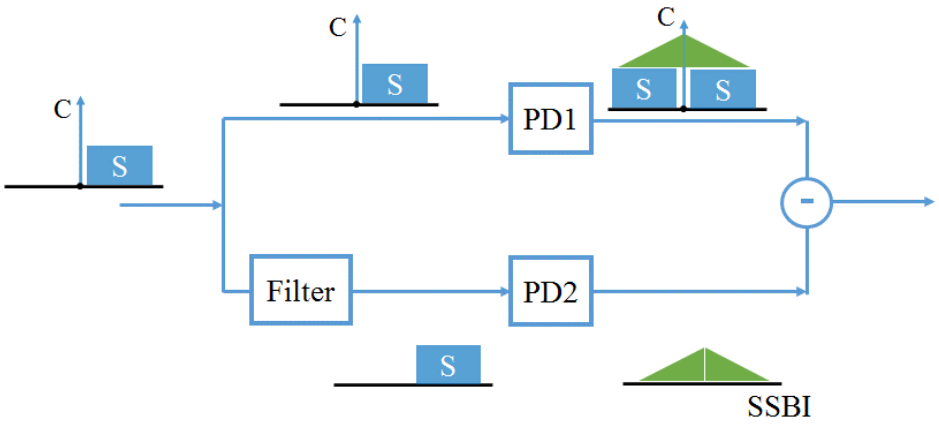

Fig. 2.16 Optical SSBI mitigation at the receiver.

fed into a filter to suppress the carrier, and then detected by PD2. The filter can be realized by a micro ring resonator (MRR) with the frequency response notch designed at the carrier frequency to sufficiently suppress SSBI.

Beyond the SSB modulation, the investigation of DSB signal field recovery via direct detection has attracted extensive research interests in the recent years. Block-wise phase shift direct detection has been proposed and the transmission of 40-Gb/s OFDM signal transmission over 80-km SSMF was demonstrated [117-119]. The main idea of the block-wise phase switching scheme is separating the carrier and signals at the transmitter, as such, the transmitter for the block-wise phase switching scheme consists of two paths as depicted in Fig. 2.17.

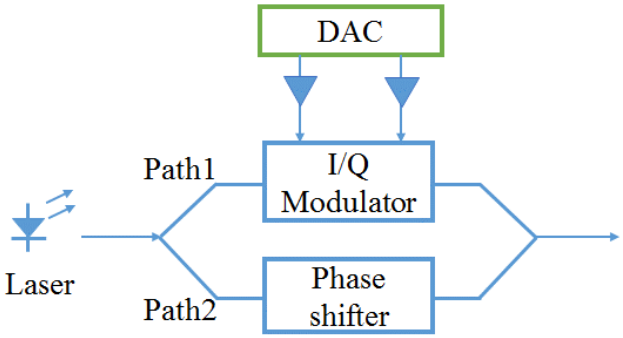

Fig. 2.17 Transmitter structure for block-wise phase switching scheme.

The corresponding data sequence in the time domain is shown in Fig. 2.18. For the data sequence shown in Fig. 2.18 (a), the data on path 1 is modulated DSB signals fed into the IQ modulator, and the data on path 2 is carrier with phase shift enabled by a phase shifter. The photocurrents of two time-domain blocks T_1 and T_2 can be given by

$$\begin{aligned} I_1 &= |S + C|^2 = |C|^2 + 2\,\mathrm{Re}[SC^*] + |S|^2 \\ I_2 &= |S + jC|^2 = |C|^2 + 2\,\mathrm{Im}[SC^*] + |S|^2 \end{aligned} \tag{2.37}$$

The combination of I_1 and I_2 contains the replica of modulated signals as follows

$$I = I_1 + jI_2 = (1+j)|C|^2 + 2SC^* + (1+j)|S|^2 \tag{2.38}$$

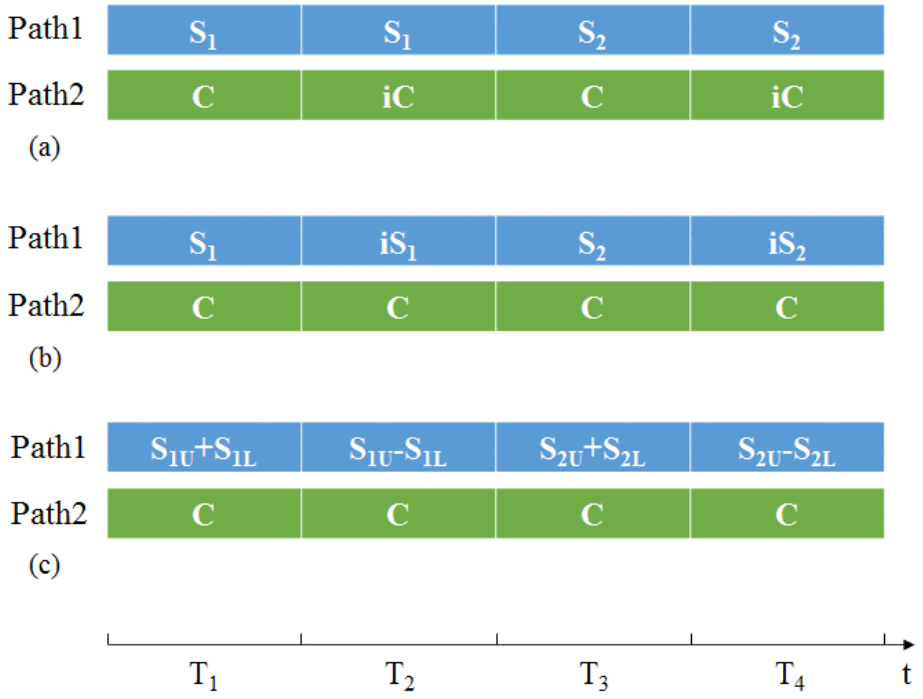

Fig. 2.18 Three approaches of data sequence for block-wise phase switching scheme.

where the second term is the reconstructed signal, and the third term is SSBI for block-wise phase switching scheme. The SSBI impacts can be either relatively weakened via a large CSPR or mitigated using the iterative cancellation scheme [120]. Analogous to the data sequence shown in Fig. 2.18 (a), the phase shift can be employed on path 1 modulated signals as presented in Fig. 2.18 (b). Fig. 2.18 (c) displayed another alternative phase shift scheme which is employed to one sideband of DSB signals. For example, the upper sideband in block T_2 stays the same as in block T_1, and the lower sideband is shifted by 180 degree, which constructs $S_{1U} - S_{1L}$. As such, the photocurrents for two consecutive time blocks can be expressed as

$$\begin{aligned} I_1 &= \left|S_U + S_L + C\right|^2 = \left|C\right|^2 + 2\,\mathrm{Re}[(S_U + S_L)C^*] + \left|S_U + S_L\right|^2 \\ I_2 &= \left|S_U - S_L + C\right|^2 = \left|C\right|^2 + 2\,\mathrm{Re}[(S_U - S_L)C^*] + \left|S_U - S_L\right|^2 \end{aligned} \tag{2.39}$$

The upper and lower sideband signals can be recovered via I_3 and I_4 as follows

$$\begin{aligned} I_3 &= I_1 + I_2 = 2\left|C\right|^2 + 4\,\mathrm{Re}[S_U C^*] + 2\left|S_U\right|^2 + 2\left|S_L\right|^2 \\ I_4 &= I_1 - I_2 = 4\,\mathrm{Re}[S_L C^*] + 4\,\mathrm{Re}[S_U S_L^*] \end{aligned} \tag{2.40}$$

Besides the desired term and DC term, the rest SSBI term still exists. Correspondingly, the signal-carrier interleaved direct detection was proposed to cancel SSBI via balanced PDs [121-122] as depicted in Fig. 2.19. The corresponding data sequence is

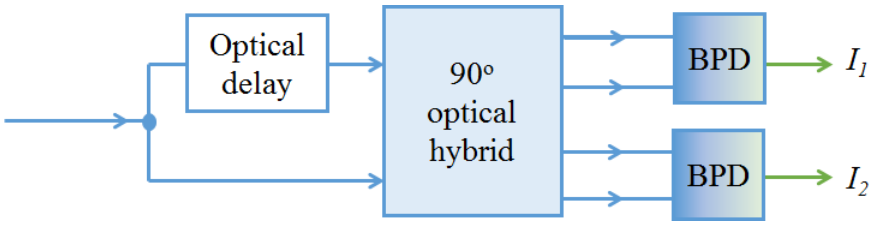

Fig. 2.19 Receiver structure for signal-carrier interleaved direct detection scheme.

signals and carrier separated in the time domain, as given in Fig. 2.20. The length of

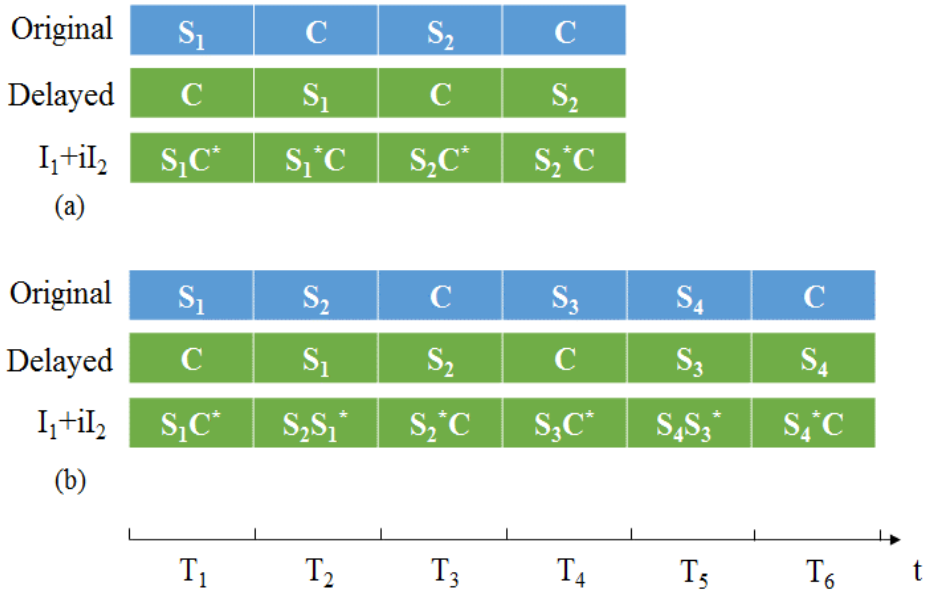

Fig. 2.20 Two approaches of data sequence for signal-carrier interleaved direct detection scheme.

optical delay is designed to be one block of either signals or carrier, and hence signals and the carrier are separated into two paths. For the data sequence shown in Fig. 2.20 (a), the DSB signals can be recovered either from block T_1 or T_2, such time-domain redundancy results in the 50% sacrifice of electrical spectral efficiency. The second approach shown in Fig. 2.20 (b) was proposed to increase the spectral efficiency. Two blocks of signals S_1 and S_2 are recovered from the time block T_1 and T_3, respectively,

with the redundancy of the time block T_2 which contains SSBI. Compared with the data sequence shown in Fig. 2.20 (a), this approach sacrifices only 1/3 of the electrical spectral efficiency [66]. With no redundancy of time or waste of spectral efficiency, the most up to date DSB signal field recovery via direct detection schemes will be discussed in Chapter 4.

Chapter 3 Field recovery of SSB signal via direct detection

3.1. Introduction

Due to the simple structure, IMDD system has been widely implemented in the short-reach transports. Intensity-modulated signals, however, are DSB signals and CD incurs the power fading issues on DSB signals. As such, CD limits the transmission distance and data rate of IMDD systems. To deal with the CD impacts and elongate the transmission distance, one promising solution is reconstructing the optical field at the receiver to digitally compensate CD. As discussed in Chapter 2, the inevitable distortion in direct detection is the beating term between signals, namely, SSBI. To enhance the optical spectral efficiency, the approaches using frequency gap to accommodate SSBI are not desirable. As such, this chapter concentrates on the direct detection schemes of SSB signals with high optical spectral efficiency, in other words, the carrier is inserted at the edge of information-bearing signals in the frequency domain.

In the recent years, KK relations have been revived in fiber-optic systems. The KK relations were initially investigated for analog radio systems [123] and then applied in optical communications recently [22]. Since KK relations can recover the phase of signals via the detected photocurrent obtained by a single-ended PD, which contributes to a simple structure. Accordingly, such receiver scheme using KK relations, namely, KK receiver has attracted extensive research interests. Theoretical derivations along with simulations of KK receiver for IQ and PAM signals were presented in [16] and [124], respectively. The experimental demonstration of 218-Gb/s single-wavelength, single-polarization transmission over 125-km SMF using KK receiver was conducted in [125], where the modulation format was OFDM. As the SNR is relatively low in the vicinity of the carrier, QPSK signals are loaded in the low-SNR region and high-order QAM16 signals are loaded in the high-frequency region. WDM systems using KK receiver have been carried out to increase the system capacity with the direct detection based simple structure [126-128]. Beyond the single polarization, dual-polarization

KK receiver has been proposed and demonstrated [129-131]. Besides KK receiver, another alternative solution of optical field recovery via direct detection is SSBI iterative cancellation. Distinguish from the linearization schemes discussed in Section 2.5, symbol decisions are made for the SSBI iterative cancellation scheme as elaborated in this chapter, and the detailed working principle will be presented in the following sections.

3.2. KK vs. SSBI iterative cancellation receiver scheme

3.2.1. Principle of KK receiver

The core of the KK receiver is utilizing the detected intensity to reconstruct the phase of SSB signals, which requires the signals to be minimum phase, namely, KK receiver relies on the minimum phase condition. Accordingly, it is desirable to introduce the minimum phase signals and KK relations.

First, to demonstrate that real and imaginary parts of SSB signals satisfy the KK relation, SSB signal is denoted as $u(t)$, and $u(t) = u_r(t) + ju_i(t)$, where $u_r(t)$ and $u_i(t)$ are the real and imaginary parts of the SSB signal $u(t)$, respectively. Via Fourier transform the SSB signal in the frequency domain is represented as $\tilde{u}(\omega)$,

$$\tilde{u}(\omega) = \frac{1}{2}[1 + sign(\omega)]\tilde{u}(\omega) \tag{3.1}$$

where $sign(\omega)$ is the sign function. As $u(t)$ is SSB, $\tilde{u}(\omega < 0) = 0$. Given the fact that the Fourier transform pair of sign function is $-j/(\pi t)$, the inverse Fourier transform of Eq. (3.1) can be given by

$$u(t) = \frac{1}{2}u(t) + jp.v.\int_{-\infty}^{\infty} dt' u(t') / [2\pi(t - t')] \tag{3.2}$$

which can be simplified as

$$u(t) = jp.v.\int_{-\infty}^{\infty} dt' u(t') / [\pi(t - t')] \tag{3.3}$$

The equation of $u(t) = u_r(t) + ju_i(t)$ can be substituted into Eq. (3.3), and it can be found the real and imaginary parts follow the KK relation as follows

$$\begin{aligned} u_r(t) &= -p.v.\int_{-\infty}^{\infty} \frac{u_i(t')}{\pi(t-t')} dt' \\ u_i(t) &= p.v.\int_{-\infty}^{\infty} \frac{u_r(t')}{\pi(t-t')} dt' \end{aligned} \tag{3.4}$$

The above discussion essentially demonstrates that the relations between real and imaginary parts of the SSB signals. In practice, for KK receiver one carrier is inserted at zero frequency and the carrier propagates along with the SSB signal. As such, the second step is taking both carrier and SSB signals into consideration, and investigating the relations between the detected photocurrent and the corresponding phase. The carrier is emulated by the constant '1', and the information-bearing signal along with the carrier are denoted as $1 + u(t)$. The real and imaginary parts of $1 + u(t)$ are defined as $|1 + u(t)|$ and $\varphi(t)$, respectively. The logarithm of $1 + u(t)$ is defined as $U(t)$, and it follows

$$U(t) = \ln[1+u(t)] = \ln\left|1+u(t)\right| + j\varphi(t) \tag{3.5}$$

As verified previously, when $U(t)$ is SSB $ln|1 + u(t)|$ and $\varphi(t)$ satisfy the KK relation. According to Taylor's expansion, with the condition of $u(t) < 1$ Eq. (3.5) can be represented as

$$U(t) = \ln[1+u(t)] = \sum_{n=1}^{\infty} (-1)^{n+1} u^n(t)/n \tag{3.6}$$

As $u(t)$ is SSB, the expansion shown in Eq. (3.6) indicates that $U(t)$ is SSB. Therefore, the real and imaginary parts of $U(t)$ follow the KK relations, which can be given by

$$\varphi(t) = p.v.\int_{-\infty}^{\infty} \frac{\ln\left|1+u(t')\right|}{\pi(t-t')} dt' = p.v.\int_{-\infty}^{\infty} \frac{\ln\left|1+u(t')\right|^2}{2\pi(t-t')} dt' \tag{3.7}$$

To fit for the optical communication system, $E_s(t)$ and E_0 are utilized to denote the information-bearing SSB signal and carrier, respectively. Since the carrier E_0 is a positive constant, Eq. (3.7) can be rewritten as

$$\varphi_E(t) = p.v.\int_{-\infty}^{\infty} \frac{\ln\left|E_0 + E_S(t)\right|^2}{2\pi(t-t')} dt' \tag{3.8}$$

where $|E_0 + E_S(t)|^2$ can be obtained from the detected photocurrent. Hence, the field recovery of SSB signals is achieved via KK relations.

It is worth noting that the above derivations are subject to two conditions, signals are required to be SSB and the carrier power should be stronger than that of information-bearing signal power, namely, the minimum phase condition should be satisfied for KK receiver.

3.2.2. Principle of SSBI iterative cancellation

For the SSBI iterative cancellation, a strong carrier is also required. Followed with the notations in Section 3.2.1, without considering the impairments in the channel the photocurrent detected by a single-ended PD in the time domain can be given by

$$\begin{aligned} I(t) &= \left|E_0 + E_S(t)\right|^2 \\ &= \left|E_0\right|^2 + 2\,\mathrm{Re}[E_0^{*} E_S(t)] + \left|E_S(t)\right|^2 \end{aligned} \tag{3.9}$$

The first term of DC can be removed simply, and with the SSBI distortions, preliminary symbol decisions are made. To obtain the relatively accurate symbol decisions, it requires the desired term to combat the second-order distortions. For OFDM signals, preliminary symbol decisions denoted by $D_0(f)$ are made in the frequency domain. To eliminate the SSBI shown in Eq. (3.9) in the time domain IFFT is implemented to estimate SSBI

$$SSBI_0(t) = \left|IFFT[D_0(f)]\right|^2 \tag{3.10}$$

where the subscript 0 indicates the preliminary process, and for the iterations shown as follows the iteration number is represented by i. With the estimated SSBI, the updated symbol decisions are made via the equation of $FFT[I(t) - SSBI_i(t)]$. The

iterations are conducted with $i = i + 1$. After several iterations of SSBI mitigation, the system performance converges, indicating that SSBI has been effectively eliminated.

Similar to KK receiver, this SSBI iterative cancellation scheme is applied for SSB signals. Besides, though the minimum phase condition does not exist, SSBI iterative cancellation relies on the feedback of symbol decisions to reconstruct second-order distortions, and hence to avoid the error propagation issue it requires a high CSPR to obtain relatively accurate preliminary symbol decisions.

3.3. Investigation of modulation formats: single- or multi-carrier modulation?

As discussed in Section 3.2, OFDM signals are taken as the example to elaborate the working principle of SSBI iterative cancellation scheme. In practice, single-carrier signals can also be applied for this scheme. In various demonstrations of KK receiver, both single- and multi-carrier modulated signals are applied. Accordingly, it is desirable to analyse which modulation format (e.g., either single- or multi-carrier modulation) fits better for the KK and SSBI iterative cancellation receiver.

To investigate the system performance of KK and IC receiver with single-carrier and OFDM modulation format, the simulation of 25Gbaud QAM16 signal transmission over 1000-km SSMF is carried out. For both single-carrier and OFDM signals, the pseudo-random binary sequence (PRBS) with the length of 2^{15}-1 is generated and repeated 10 times in order to obtain reasonable statistics. Single-carrier QAM16 signals are digitally generated with the roll-off factor of 0. For OFDM signals, 512 out of 2048 subcarriers are loaded with data and one subcarrier can be used as a carrier. For single-carrier signals, the carrier is inserted at one edge of the information-bearing signals in the frequency domain, with the frequency gap of 0.39 GHz, which is the same as the bandwidth of guard band applied for OFDM signals. In practice, the inserted carrier with the offset frequency can be implemented using an intensity modulator. The information-bearing signals and carrier are combined via an optical coupler, and the various CSPRs are obtained by tuning the carrier power. Signals along with the carrier are transmitted over 1000-km SSMF, and the CD parameter is set to

be 17 ps/(nm×km). It is worth noting that to focus on the CD impacts, fiber losses are neglected, and no optical filters are utilized in the transmission link. As optical filters are power-hungry devices, and the laser wavelength drift induced by the temperature change needs to be deliberately avoided once optical filters were implemented. After transmission over the fiber, signals are fed into the single-ended PD, which is emulated by a square-law detector. At the receiver, the sample rate is 100 Gsample/s, corresponding to the oversample rate of 4, Although the KK receiver requires the high sample rate due to the logarithm operation, the oversample rate of 4 is generally

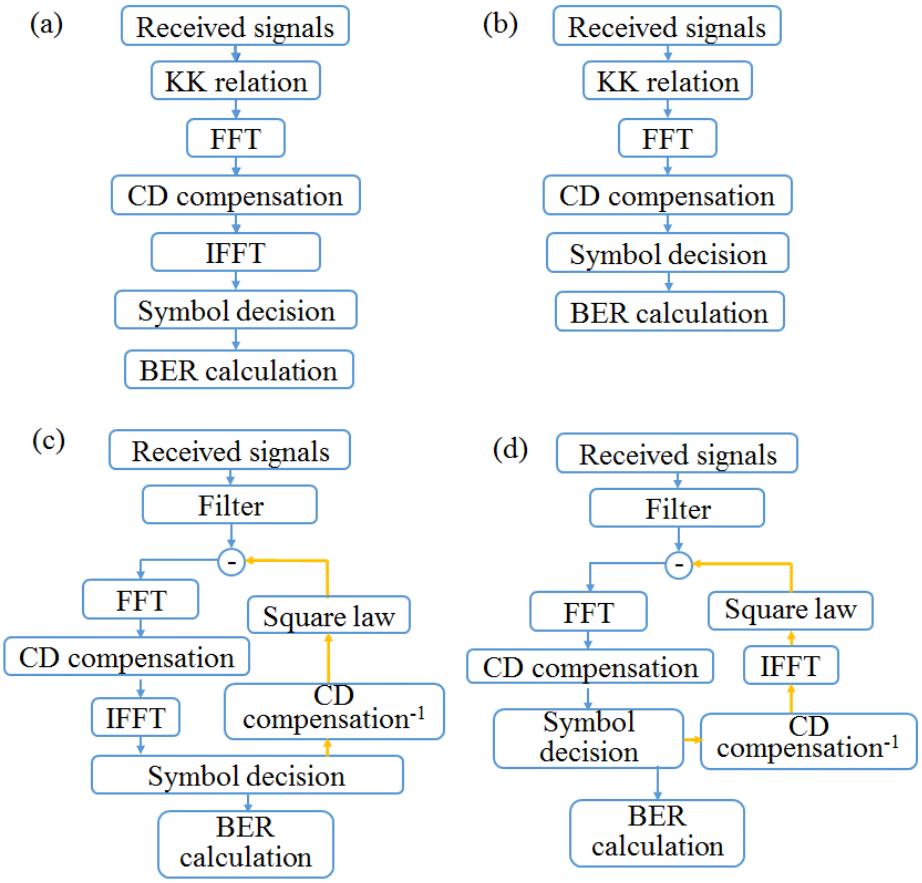

Fig. 3.1 DSP flow chart for (a) single carrier using KK receiver, (b) OFDM using KK receiver, (c) single carrier using IC receiver, and (d) OFDM using IC receiver.

sufficient. For KK and IC receiver with either single-carrier or OFDM modulation formats, the corresponding DSP flow chart is depicted in Fig. 3.1.

Due to the square-law detection, the received signals are DSB. For the KK receiver, after implementing the KK relation one sideband is suppressed and the data is

recovered from the remained sideband. Given that CD compensation is conducted in the frequency domain, FFT is utilized to transform signals to the frequency domain as shown in Fig. 3.1(a) and (b). For the single-carrier modulation, symbol decisions are made in the time domain which requires the IFFT operation as presented in Fig. 3.1(a). Finally, BER calculations are conducted. For the IC receiver, a digital SSB filter is employed to truncate one sideband of received DSB signals. To make preliminary symbol decisions, a pair of FFT and IFFT along with the CD compensation is utilized for single-carrier modulation. In the iteration of SSBI cancellation, the CD impacts are required to be reloaded to emulate CD distorted signals, and reconstruct CD distorted SSBI. The reconstructed SSBI is removed from received signals, and then sent to the decision processing to obtain updated symbol decisions and BERs as shown in Fig. 3.1(c). For the OFDM signal using IC receiver, the corresponding DSP flow chart is depicted in Fig. 3.1(d). At the output of the iteration loop, updated BER is obtained,

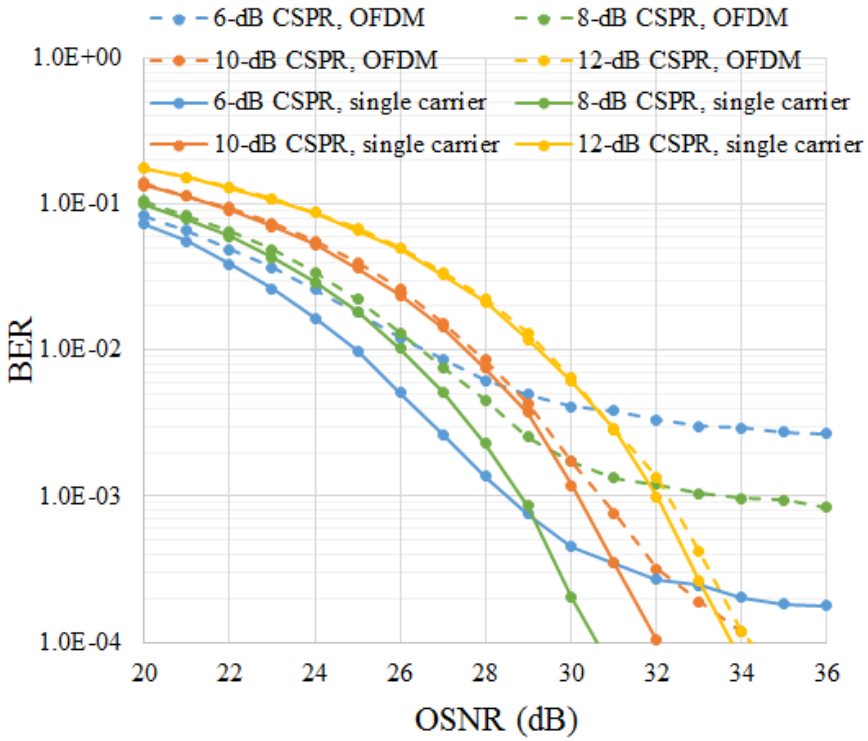

Fig. 3.2 System performance of KK receiver with single-carrier and OFDM modulation formats at btb.

which can be used as a metric of whether the system performance converges and the termination of iterative cancellation.

Fig. 3.2 presents the system of KK receiver for the btb condition. At low CSPRs (e.g., 6 dB), the minimum phase condition is not fully satisfied, and the error floors can be observed in Fig. 3.2 regardless of the modulation format. With the CSPR of 6 dB, the error floors of single-carrier and OFDM signals are around 1.7×10^{-4} and 2.6×10^{-3}, respectively. At the level of 7% HD-FEC (4×10^{-3}) with the CSPR of 6 dB, the OSNR sensitivity is 26.4 dB and 30 dB for single-carrier and OFDM signals, respectively. As the CSPR increases, the performance difference of two modulation formats decreases. When the CSPR increases from 8 dB to 10 dB, the OSNR sensitivity difference of two modulation formats decreases from 0.9 dB to 0.1 dB. At

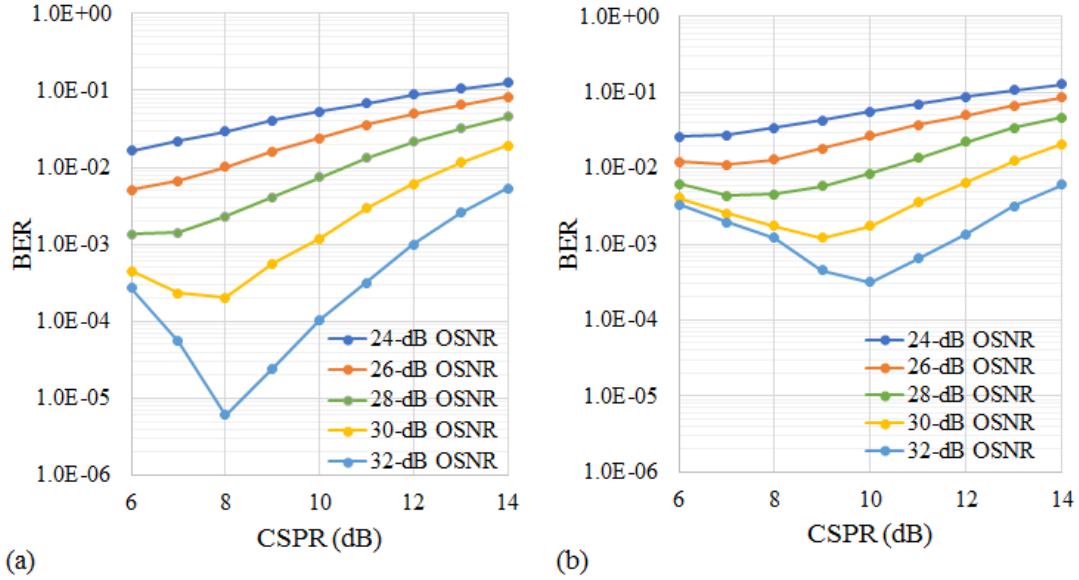

Fig. 3.3 BER performance as a function of CSPR for KK receiver at btb for (a) single-carrier and (b) OFDM signals.

high CSPRs like 12 dB, the performance of single carrier and OFDM signals is generally the same.

To identify the optimal CSPR at various OSNRs, Fig. 3.3 presents the BER versus CSPR for the KK receiver. At high OSNRs, for example 32 dB, the optimal CSPR is found to be 8 dB and 10 dB for single-carrier and OFDM signals, respectively. Besides, the 8-dB CSPR enables KK receiver with single-carrier modulation superior performance to that of OFDM counterpart with 10-dB CSPR, which indicates that for the btb condition single-carrier modulation requires a lower CSPR than that of OFDM

signals without the sacrifice of BER performance. As the OSNR decreases, the optimal CSPRs for both single-carrier and OFDM signals decrease correspondingly, and the performance of single-carrier and OFDM signals tends to be similar. The reason of single-carrier modulation better fits for KK than OFDM is attributed to the PAPR. As the field reconstruction of KK receiver relies on the minimum phase condition, which

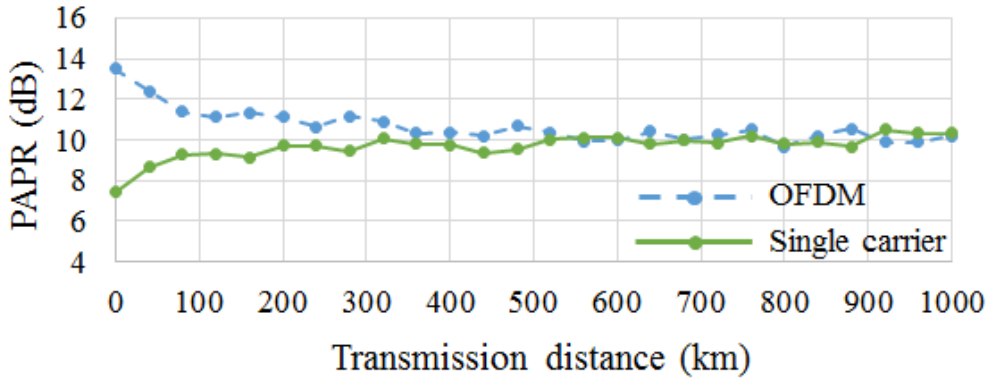

Fig. 3.4 PAPR of OFDM and single-carrier signals versus the transmission distance.

requires that the time trajectory of signals in the complex plane does not encircle the origin, signals with high PAPR are more likely to violate the minimum phase condition.

To study the PAPR impacts, the PAPR as a function of transmission distance is presented in Fig. 3.4. At btb, the PAPR of OFDM signals is evidently much larger than that of single-carrier signals due to the nature of multi carriers. As the transmission distance increases, the PAPR tends to be dominated by the CD impacts rather than the characteristics of either single- or multi-carrier modulation formats, and hence after transmission over 1000-km SSMF the PAPRs of both single-carrier and OFDM signals converge to around 10 dB. This PAPR variation trend shown in Fig. 3.4 generally agrees with the statistical PAPR distribution over the fiber [132].

To verify the PAPR impacts on KK receiver after transmission, the transmission performance is depicted in Fig. 3.5. After 40-km transmission, it can be seen from Fig. 3.4 that the PAPR of OFDM signals is still higher than that of single-carrier signals, and Fig. 3.5 (a) shows that at various OSNRs the system performance of single-carrier signals is better than OFDM signals. When the PAPR is almost the same after 1000-km transmission, the BER curves of two modulation formats are overlapped as shown in Fig. 3.5 (b). This phenomenon reveals that the intrinsic high PAPR of OFDM

signals is detrimental to the KK receiver. Accordingly, compared with OFDM, single-carrier modulation is appropriate for the KK receiver based short-reach applications.

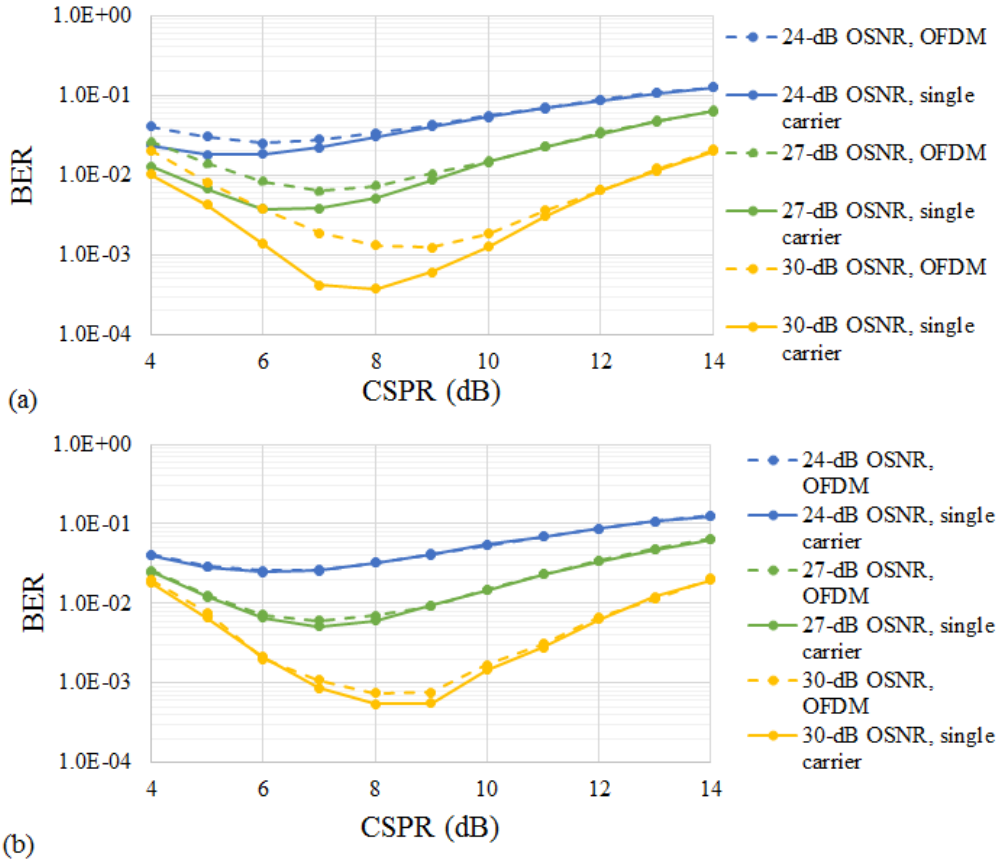

Fig. 3.5 System performance of KK receiver using single-carrier and OFDM signals after (a) 40- and (b) 1000-km transmission.

For the IC receiver, since the SSBI mitigation relies on the iterative cancellation, four iterations are employed, and the BER performance of both OFDM and single-carrier signals is presented in Fig. 3.6. At the low CSPR such as 6 dB, the error floor is observed starting from the OSNR of 28 dB. That is because at low CSPRs, the preliminary symbol decisions are not accurate, leading to the reconstructed SSBI with errors, and hence the SSBI is not effectively mitigated. When the OSNR is low, such error propagation issue is not prominent, while at high OSNRs, the dominant limitation in the system is SSBI rather than the optical noise. As such, increasing the OSNR does not bring in more improvement, namely, the error floor at low CSPRs indicates that IC receiver also requires a strong carrier to enable relatively accurate symbol decisions.

As the CSPRs increase, no error floors are observed in Fig. 3.6, which indicates that IC receiver works properly. For the 8-dB CSPR case, OFDM signals evidently outperforms single-carrier signals. When the CSPR increases to 14 dB, the performance of two modulation formats tends to be the same.

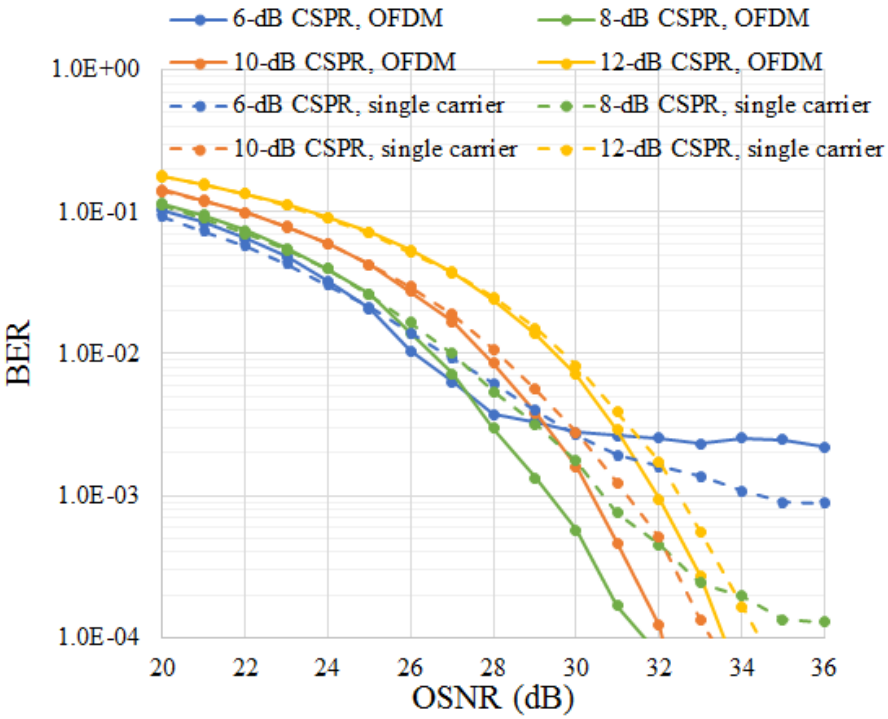

Fig. 3.6 System performance of IC receiver with single-carrier and OFDM modulation formats at btb.

For the optimal CSPR of 8 dB for the IC receiver, the BER performance as a function of iteration number is presented in Fig. 3.7. For single-carrier signals, at various OSNRs, only first two iterations are effective in mitigating SSBI, the third and fourth iterations do not contribute to the improvement of the system performance. While for OFDM signals, the fourth iteration can still bring in some marginal improvement. As such, it can be concluded that the SSBI mitigation of IC receiver is more effective for OFDM signals than single-carrier signals. This phenomenon can be elaborated as follows. In the frequency domain, SSBI is more severe at low frequencies. As such, the low-frequency subcarriers of OFDM signals are more distorted than the high-frequency subcarriers. While for single-carrier signals, symbol decisions are made in the time domain, SSBI is also formed and spread in the time domain. Accordingly, the preliminary symbol decisions (e.g., iteration number equals to 0) of

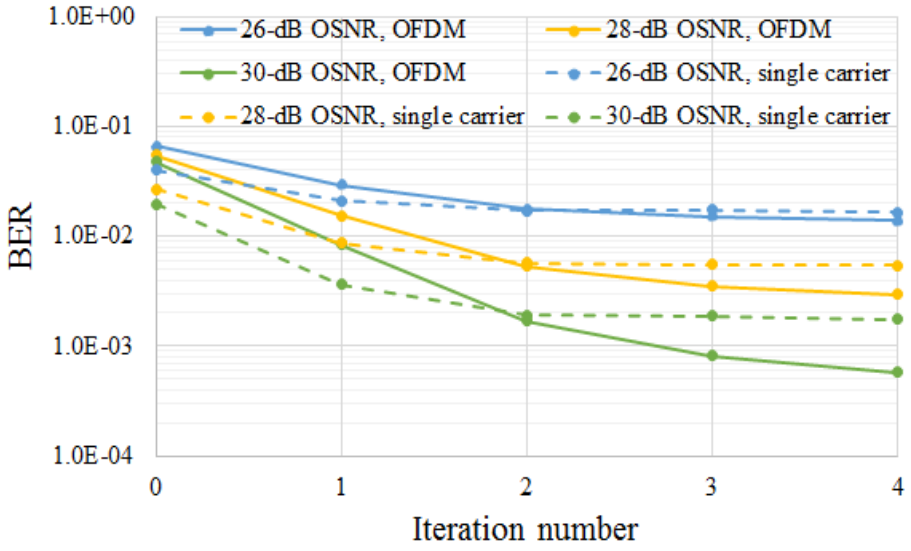

Fig. 3.7 System performance of IC receiver versus iteration number at btb.

single-carrier signals are more accurate than those of OFDM signals. Besides, the more effectiveness of iterative SSBI cancellation for OFDM than single-carrier signals is attributed to the correlation between estimated SSBI and symbol decisions. As symbol decisions of single-carrier signals and estimated SSBI are made and subtracted in the time domain, the high correlation between the symbol decisions and reconstructed SSBI involves error propagation in the iterations, and hence only two iterations are

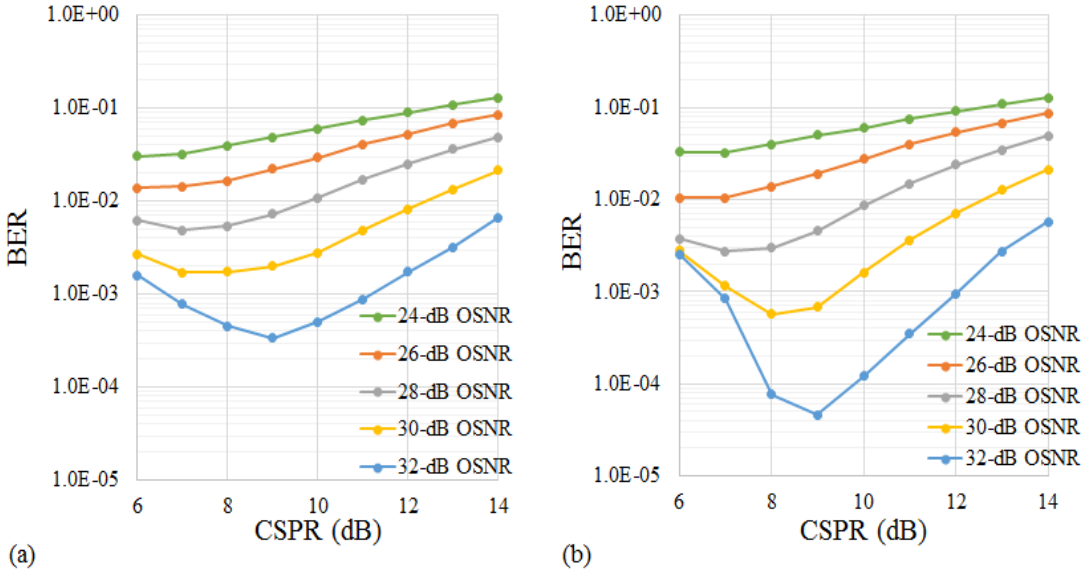

Fig. 3.8 BER as a function of CSPR for IC receiver at btb for (a) single-carrier and (b) OFDM.

effective in mitigating SSBI for single-carrier signals. On the other hand, the low correlation between OFDM symbol decisions and reconstructed SSBI enables the superior performance of the IC receiver using OFDM signals.

The BER performance as a function of CSPR for the IC receiver is depicted in Fig. 3.8 for the btb condition. Although the optimal CSPR is 9 dB for both single-carrier and OFDM signals at 32-dB OSNR, the BER of OFDM signals is much lower than that of single-carrier signals, which reveals that OFDM is the better fit for the IC receiver.

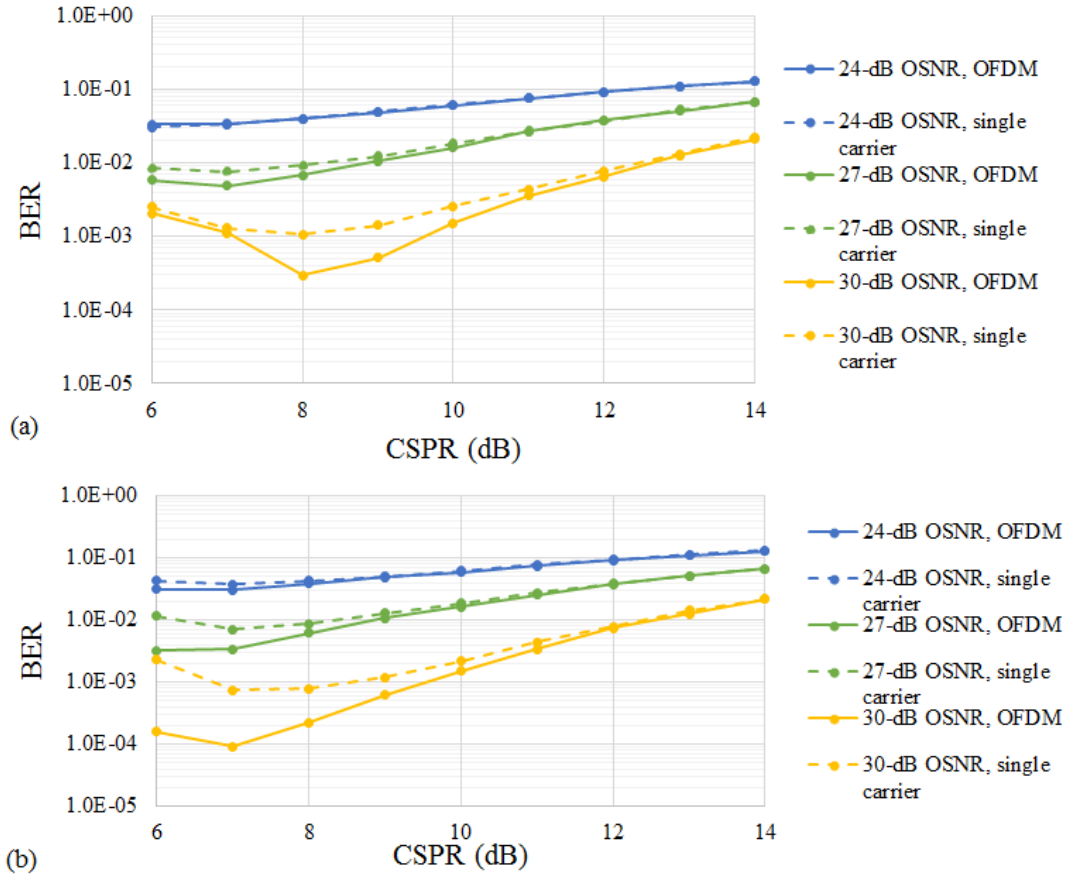

Fig. 3.9 System performance of IC receiver using single-carrier and OFDM signals after (a) 40- and (b) 1000-km transmission.

The transmission performance of IC receiver is presented in Fig. 3.9. For both 40- and 1000-km transmission, OFDM signals evidently outperform single-carrier signals at high OSNRs due to the low correlation between reconstructed SSBI and

OFDM symbol decisions made in the frequency domain. At low OSNRs, the dominant limitation in the system is the optical noise rather than the second-order distortions, and hence the performance of single-carrier and OFDM signals tends to be the same.

To conclude, the single-carrier signal fits better for the KK receiver due to the inherent low PAPR of the single-carrier signal, while OFDM signal is the preferable modulation for the IC receiver.

3.4. Chromatic dispersion impacts

Among various impairs during the transmission over the fiber, dispersion is one of the major factors limiting the system capacity and transmission reach. The dispersion refers to the phenomenon that each spectral component of the signal travels at different velocities over the fiber and cannot reach the receiver at the same time. The dispersion includes modal dispersion, chromatic dispersion, and polarization mode dispersion. The modal dispersion refers to the fact that different modes travel with different velocities, which exists in the MMF [133-135]. For the SMF, chromatic dispersion is generally the main limitation of the transmission distance, and this section concentrates on the chromatic dispersion impacts on the direct detection schemes with field recovery.

The chromatic dispersion involves the material and waveguide dispersion [136]. The material of the fiber core is the silica, whose refractive index varies according to the signal frequency. The waveguide dispersion is a function of fiber parameters including the normalized frequency and normalized propagation constant. Although the waveguide dispersion can be tuned by tailoring the waveguide structure, for the SSMF working in the C band, the chromatic dispersion is not negligible [137].

Due to the material and waveguide dispersion, signal components of different frequency travel at different velocities. The group velocity v_g is defined as

$$v_g = \left(\frac{d\beta}{d\omega}\right)^{-1} \tag{3.11}$$

where β is the propagation constant, and ω denotes the frequency of the signal. For the fiber length of L, the time delay is expressed as L/v_g. To express the pulse broadening ΔT, source spectral width is denoted as $\Delta\omega$, and ΔT is given by

$$\begin{aligned}\Delta T &= \frac{dT}{d\omega}\Delta\omega \\ &= \frac{d}{d\omega}\left(\frac{L}{v_g}\right)\Delta\omega \\ &= L\frac{d^2\beta}{d\omega^2}\Delta\omega \\ &= L\beta_2\Delta\omega\end{aligned} \tag{3.12}$$

where β_2 is the GVD coefficient. Eq. (3.12) expresses the extent of pulse broadening as a function of spectral width. To identify the relation between pulse broadening and the range of wavelength $\Delta\lambda$, Eq. (3.12) can be derived as

$$\Delta T = \frac{d}{d\lambda}\left(\frac{L}{v_g}\right)\Delta\lambda = DL\Delta\lambda \tag{3.13}$$

where D is the dispersion parameter, which is given by

$$D = \frac{d}{d\lambda}\left(\frac{1}{v_g}\right) = -\frac{2\pi c}{\lambda^2}\beta_2 \tag{3.14}$$

The dispersion parameter D is in the unit of ps/nm/km, which implies the pulse broadening extent is 1 ps when the signal with 1-nm bandwidth transmits over 1-km fiber. Followed with the expression of dispersion parameter D, the channel response $H(L,\omega)$ induced by chromatic dispersion is expressed as

$$H(L,\omega) = \exp(j\beta_2\omega^2 L/2) = \exp\left(-\frac{j\omega^2 LD\lambda^2}{4\pi c}\right) \tag{3.15}$$

One choice of compensation of the chromatic dispersion shown in Eq. (3.15) is implementing the fiber with the opposite dispersion value, namely, the dispersion compensation fiber (DCF). However, the insertion loss and bending loss of the DCF are higher than those of the SSMF, which is not desirable for the short-reach applications. Another solution is the electronic dispersion compensation (EDC), which

refers to either time-domain or frequency-domain compensation. In [138], it has been reported that for high-capacity and long-reach application scenarios, frequency-domain compensation is preferable.

For the KK and IC receiver, as the optical field can be reconstructed, the transmission distance of the link using these receiver schemes is up to several spans of fiber, and hence the corresponding chromatic dispersion impacts are desirable to be studied. To demonstrate the chromatic dispersion impacts, the experiment of 80-Gb/s QPSK signal transmission over 160-km SSMF is conducted, and the experimental setup is depicted in Fig. 3.10.

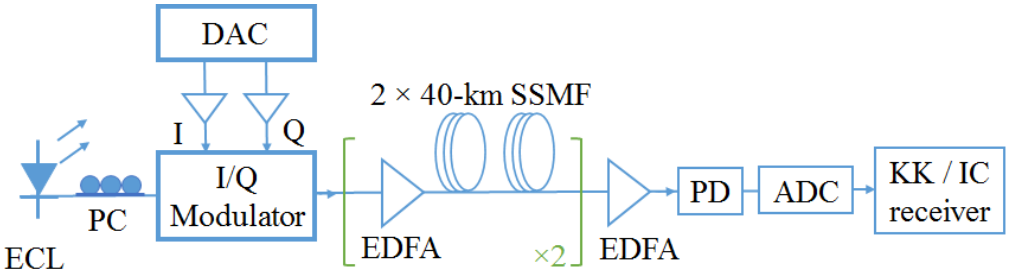

Fig. 3.10 Experimental setup of KK and IC receiver. ECL: external cavity laser.

Both single-carrier and OFDM signals are analysed in the experimental demonstration. For single-carrier modulation, the digitally generated 40-Gbaud QPSK signals along with the carrier are fed into the DAC. For OFDM signals, the FFT size is 4096 and 2176 subcarriers are loaded with the data, which corresponds to the 42.5 Gbaud raw data rate. The cyclic prefix (CP) is inserted with the ratio of 1/16, as such, the data rate is 40 Gbaud after removing the CP. The carrier amplitude is digitally tuned to obtain various CSPRs, ranging from 4 to 14 dB. The laser is an external cavity laser, with the wavelength of 1550 nm. The I and Q components of signals are fed into a pair of electrical amplifiers to fit for the MZM. As the MZM is biased at null point, an EDFA is implemented at the output of the MZM. Two loops of 40-km SSMF constitute the 80-km span, and two spans are employed in the link. At the receiver, a 43-GHz PD is utilized, and the sampling rate of the ADC is 160 GSa/s, which generally satisfies the requirement of high oversample rate of KK receiver, otherwise the digital upsampling before conducting KK relations is a necessity. The DSP flow chart for

both single-carrier and OFDM signals generally follows the procedure shown in Fig. 3.1.

As IC receiver requires several iterations to mitigate SSBI, which definitely increases the system complexity, it is preferable to strike the balance between the required iteration number and the system performance. Fig. 3.11 depicts the Q-factor

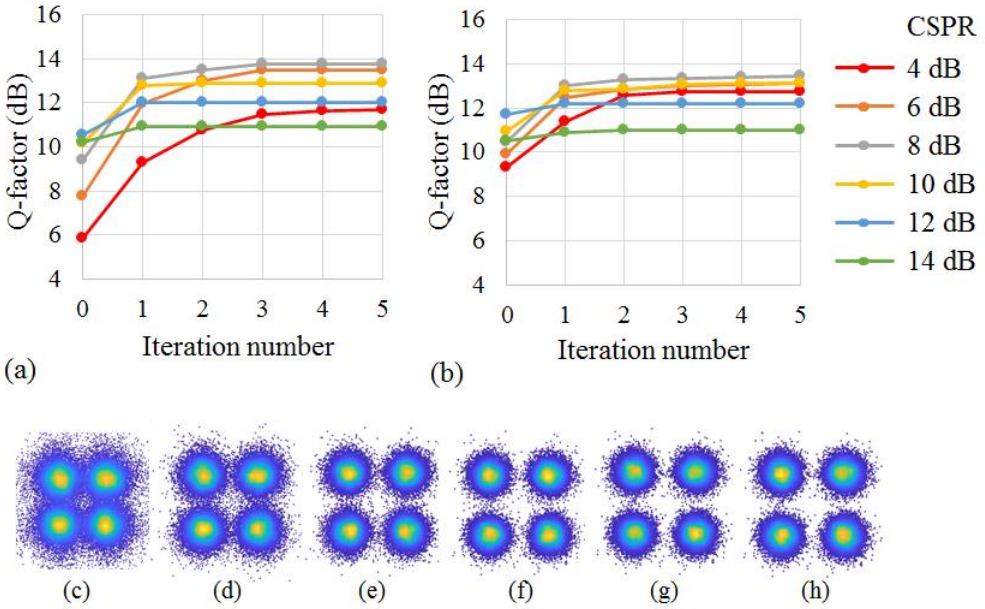

Fig. 3.11 Q-factor as a function of iteration number at btb for (a) OFDM, and (b) single-carrier signals with various CSPRs. (c-h) are the OFDM signal constellations without the iterative cancellation and with 1-, 2-, 3-, 4-, 5-times iterations, respectively.

versus iteration number for both OFMD and single-carrier signals. When the CSPR is as low as 4 dB, SSBI is the major limitation of the performance, and after four iterations, the Q-factor is improved by 5.8 and 3.4 dB for OFDM and single-carrier signals, respectively. The corresponding constellations of the OFDM signals are shown in Fig. 3.11(c-h), which verify the improvement due to the iterative cancellation of SSBI. The optimal CSPR for both modulation formats is found to be 8 dB, and OFDM signals outperform the single-carrier signals. Accordingly, it is reasonable to adopt OFDM signals for the IC receiver. Besides, at the optimal CSPR of 8 dB, only the first two iterations evidently bring in improvements, the third and

following iterations do not continue to provide predominant contributions. As such, the iteration number is set to be two to reduce the computational complexity.

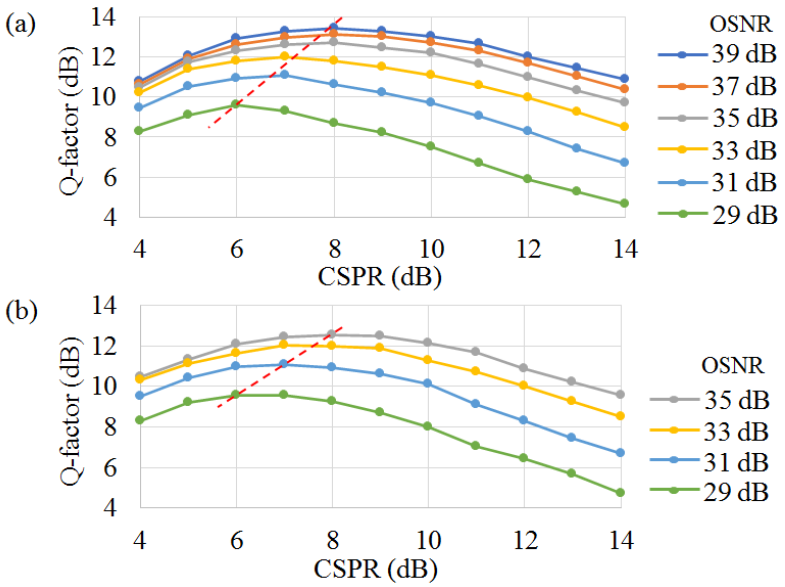

Fig. 3.12 Q-factor as a function of CSPR at various OSNRs for the IC receiver (a) at btb, (b) after 160-km transmission.

The btb and transmission performance of OFDM signal using IC receiver is depicted in Fig. 3.12. After 160-km transmission, the highest achievable OSNR reduces from 39 dB to 35 dB. The optimal CSPRs at various OSNRs as illustrated by the red dashed line in Fig. 3.12 (a) and (b), namely, before and after transmission, are generally the same, which range from 6 to 8 dB according to the OSNR. In addition, it is noted that at the same OSNR, the Q-factor almost remains unchanged before and after transmission.

The system performance of KK receiver with the single-carrier modulation format is presented in Fig. 3.13. Distinguish from the IC receiver, the optimal CSPRs for the KK receiver increase after transmission, namely, the KK receiver requires a higher CSPR after 160-km transmission. This phenomenon is due to the increase of PAPR as the transmission distance increases, and the signals with higher PAPR require a stronger carrier to not encircle the origin in the complex plane.

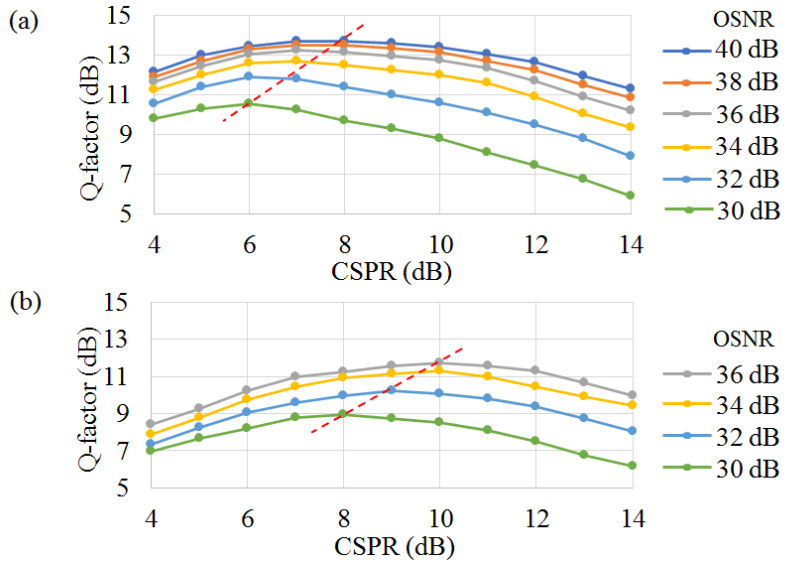

Fig. 3.13 Q-factor as a function of CSPR at various OSNRs for the KK receiver (a) at btb, (b) after 160-km transmission.

The CD impacts on KK and IC receiver can be observed and compared from the OSNR sensitivity at various transmission distances, as shown in Fig. 3.14. The BER threshold is set to be 1×10^{-3}, and the required OSNR for the btb, 40-, 80-, 120-, and 160-km transmission cases is depicted. At btb, the KK receiver outperforms IC receiver for various CSPRs. However, the required OSNR of KK receiver increases as the transmission distance increases. For example, the required OSNRs of signals with

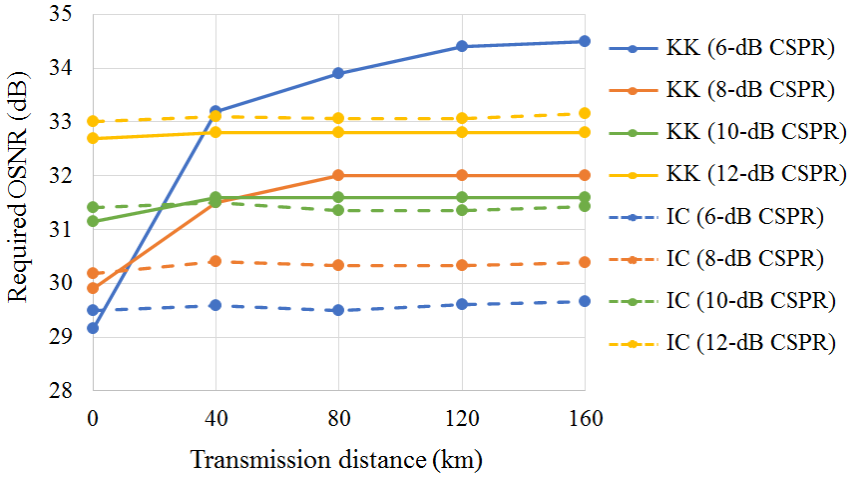

Fig. 3.14 Required OSNR versus transmission distance for both KK and IC receiver (@BER=1.0×10^{-3}).

6- and 8-dB CSPR increase by 4.1 dB and 1.6 dB after 40-km transmission compared with the btb condition, indicating that the KK receiver is sensitive to the CD impacts. This phenomenon is attributed to the increase of PAPR as single-carrier signals propagate over the fiber, which has been elaborated in Section 3.3. When the CSPR is high (e.g., 10 and 12 dB), the required OSNR curve of the KK receiver tends to be flat. While the required OSNRs for the IC receiver almost remain unchanged after transmission regardless of the CSPR, which verifies that IC receiver is robust against CD.

3.5. Polarization mode dispersion impacts

As the SSMF supports two orthogonal modes, signals on one polarization would degrade another polarization due to the polarization crosstalk, leading to the impairments upon direct detection. The PMD impacts on OFDM signals direct detection have been studied in [139], and the degradation of SNR resulted by the PMD induced frequency-dependent fading is observed [140 - 142]. The KK receiver proposed in the recent years is another novel scheme to recover IQ signals via direct detection. As KK receiver is a promising solution of short- to medium-reach transports, given that the transmission distance can be several spans of fibers, PMD impacts are worth investigating, and this section concentrates on the PMD impacts on the single-polarization KK receiver.

The initially proposed KK receiver in optical communications is a single-polarization system, where the signals are aligned in one polarization state with another null polarization state at the transmitter side. However, the first-order PMD is a widely existing detrimental factor in SSMF, and at the receiver side both principal polarization states contain ‘signals’, which can be expressed in the Jones space. Under the approximation of first-order PMD, the polarization rotation matrix U is given by

$$U(\omega) = T^{-1}\begin{bmatrix} e^{-j\omega\Delta\tau/2} & 0 \\ 0 & e^{j\omega\Delta\tau/2} \end{bmatrix} T \tag{3.16}$$

where T is the Jones matrix denoting the polarization rotation in output and input of the fiber, ω denotes the frequency, and $\Delta\tau$ is the time delay between two principal polarization states induced by the PMD effects. Correspondingly, at the frequency of ω_c the received signal can be expressed as

$$\begin{bmatrix} X_i \\ Y_i \end{bmatrix} = U^{-1}(\omega_c)U(\omega_c + \omega_i)\begin{bmatrix} S_i \\ 0 \end{bmatrix} \tag{3.17}$$

where ω_i is the signal frequency of the i-th subcarrier, and S_i denotes the signals of the i-th subcarrier. It can be learned from Eq. (3.17) that for the input single-polarization signals, after transmission over the fiber the PMD impairs the signals to be dual-polarization at the output of fiber, as both X and Y polarization components are not null. For the KK receiver, the single-ended PD used in the KK receiver is polarization insensitive, and gives the output of $|X_i|^2 + |Y_i|^2$ due to square-law detection. To be specific, X polarization suffers from attenuation at high frequency, and Y polarization has crosstalk from X polarization, both of them are detrimental to the performance of KK receiver. To assess the performance degradation of KK receiver due to the first-order PMD, Q-factor is utilized as an approximate indicator.

The simulation of KK receiver with PMD effects is conducted. To focus on first-order PMD impairments, CD impacts are neglected in the simulation. The modulation format used in this simulation is single-carrier QAM16, as the PAPR of single-carrier signals is generally lower than that of multi-carrier signals, which is preferable for the KK receiver. For the baud rate varying from 10 to 50 Gbaud, the oversample rate is consistently set to be four times to meet the requirement of high sample rate. At the transmitter, information-bearing signals along with the carrier are aligned on the same polarization, with another polarization set to be null. It is defined that the transmitted SSB signals are on the X polarization, and the principal state of polarization is 45^o with respect to the X polarization. The CSPR is set to be 10 dB to fully satisfy the minimum phase condition. At the receiver, one SSB filter is utilized to mitigate the noise of the null sideband, and hence provide the OSNR improvement of 3 dB compared with the simulation results without using SSB filters.

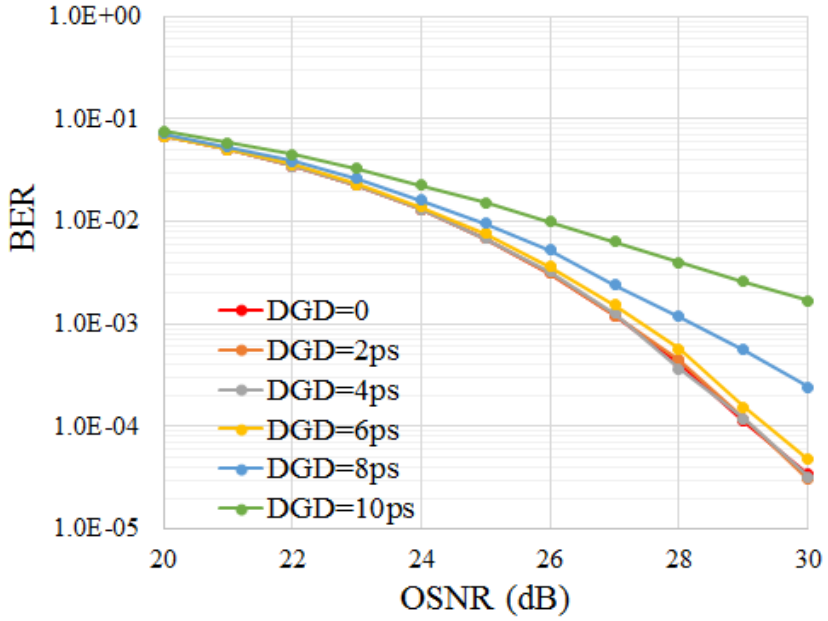

Fig. 3.15 BER versus OSNR for 25Gbaud QAM16 signals using KK receiver with various DGD.

For various differential group delays (DGDs), the BER performance versus OSNR for 25 Gbaud QAM16 signals using KK receiver is depicted in Fig. 3.15. When the DGD is lower than 6 ps, the OSNR penalty is negligible. When the DGD increases to 8 ps, at the BER threshold of 4×10^{-3} the OSNR penalty is less than 1 dB compared to the 0-ps DGD case.

For various baud rates the Q-factor penalty as a function of DGD is presented in Fig. 3.16 with the BER threshold of 4×10^{-3}. Given that PMD effects are frequency

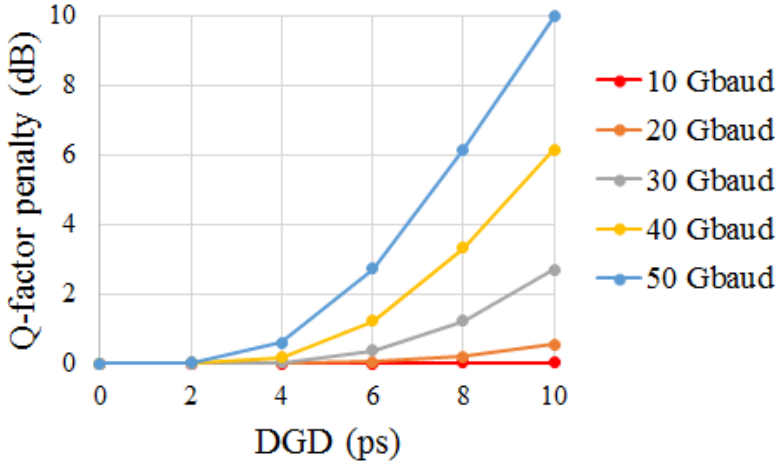

Fig. 3.16 Q-factor penalty as a function of DGD @BER=4×10^{-3}.

dependent, it is expected that signals with wider bandwidth are more sensitive to the polarization rotation due to the PMD effects. The DGD value is set to be from 0 to 10 ps in the simulation. Assuming the PMD efficient of SSMF is 0.1 $ps/\sqrt{km}$, and the maximum instantaneous DGD is estimated to be the worst case, namely, 3 times of the mean DGD [143], the transmission over 100-km SSMF corresponds to 3-ps DGD, and the 10-ps DGD is an appropriate estimation of the transports using KK receiver (e.g., several spans of SSMF). For the baud rate up to 50Gbaud, the first-order PMD induced Q-factor penalty is less than 1 dB when the DGD is less than 4 ps. Beyond the DGD of 6 ps, the Q-factor penalty is conspicuous especially for the high-speed transmission system. One example is that the Q-factor penalty is 10 dB when the DGD is 10 ps for the 50Gbaud system.

To conclude, the first-order PMD is detrimental even for the single-polarization KK receiver, however, given that the KK receiver is designed for the transmission links of up to several spans, the PMD effects are not a major limiting factor of the system performance.

Chapter 4 Field recovery of DSB signal via direct detection

4.1. Introduction

Coherent detection has created profound impacts on optical communications due to its superior capability of recovering both optical intensity and phase, namely, field recovery [144]. Although as elaborated in the previous chapters direct detection can realize the field recovery of SSB signals as the coherent detection does, only one sideband of SSB signals carries information, which is a waste of spectral efficiency. Spectral efficiency covers both optical and electrical spectral efficiency. It has been reported that the optical spectral efficiency can be enhanced using either WDM technique [145-148] or twin SSB modulation [149-151], however, the optical spectrum is not a comparatively precious resource especially for short- and medium-reach link. As for electrical spectral efficiency, the characteristics of SSB inevitably sacrifice half of the receiver bandwidth. Besides, the optical filter is required for SSB signals, otherwise the square-law detection involves noise-folding issues. Given that DSB signals are generally employed for coherent systems to fully utilize the receiver bandwidth, it is highly desirable to achieve the analogical function using cost-effective direct detection, in other words, enable the field recovery of DSB signal via direct detection.

In the recent years, several novel direct detection schemes of DSB signal field recovery have been proposed and demonstrated. The intensity of signals is detected by the PD, and phase recovery of DSB signals is the crux. One approach of optical signal phase reconstruction is using temporal transport-of-intensity equation (TIE), the corresponding conceptual diagram is depicted in Fig. 4.1 [152-153]. The complex amplitude of the DSB signal is denoted as $E(t)$,

$$E(t) = \sqrt{P_0(t)}\exp[j\phi_0(t)] \tag{4.1}$$

where $P_0(t)$ and $\emptyset_0(t)$ are the power and phase of the signal, respectively. The signals are split into two paths as shown in Fig. 4.1, in the upper path the dispersive medium

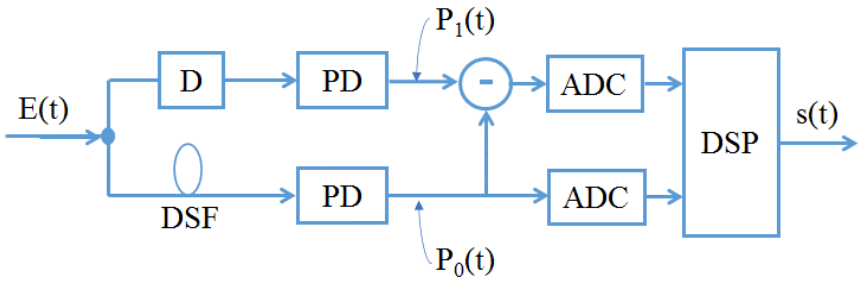

Fig. 4.1 Conceptual diagram of the TIR based receiver. D indicates the dispersive medium, and DSF represents dispersion shifted fiber.

is employed, and dispersion shifted fiber (DSF) is implemented on the lower path. One-dimensional TIE equation is given by

$$\frac{\partial}{\partial t}\left(P\frac{\partial \phi}{\partial t}\right)=\frac{1}{\beta_2}\frac{\partial P}{\partial z} \tag{4.2}$$

As such, the signal phase and power has been related. The right-hand side of the Eq. (4.2) can be approximated using

$$[P(t,d)-P(t,0)]/(\beta_2 d)=[P_1(t)-P_0(t)]/(\beta_2 d) \tag{4.3}$$

where $P_1(t)$ and $P_0(t)$ are the power shown in Fig. 4.1, and β_2 is the group-velocity dispersion of the dispersive medium. Eq. (4.3) can be substituted into Eq. (4.2) and the optical signal phase is extracted from two photocurrents given by two single-ended PDs. This TIE based approach relies on the detected power including both carrier-signal beating and SSBI power, and hence the receiver bandwidth needs to be wide enough to detect the power of all the beating terms. Another scheme of DSB signal field reconstruction is based on the modified Gerchberg-Saxton (GS) algorithm [154]. The phase can be retrieved via two temporal intensity photocurrents, however, it requires several hundred iterations to enable the algorithm to converge. Using this algorithm, transmission of dual-polarized 30-Gbaud QPSK signal over 520-km SSMF has been demonstrated.

In this chapter, after illustrating the structure of CADD receiver, the algorithm of recovering DSB signals is presented. No time-domain redundancy is needed for CADD scheme, and for DSB signals the lower and upper sidebands are filled with uncorrelated information-bearing signals. Given the fact that there exists a small

frequency gap between two sidebands, and the bandwidth of frequency gap along with the optical delay and CSPR are related to the system performance, the joint optimization of these parameters is conducted. The first-time experimental demonstration of CADD receiver is carried out, and the IQ imbalance impacts on the CADD receiver are analysed.

4.2. Structure and principle of CADD receiver

Before elaborating the algorithm of recovering DSB signals via CADD receiver, it is necessary to briefly introduce the receiver structure of CADD as presented in Fig. 4.2. To obtain the replica of modulated signals, the carrier is required to obtain the beating term between signals and the carrier. As such, the optical field can be

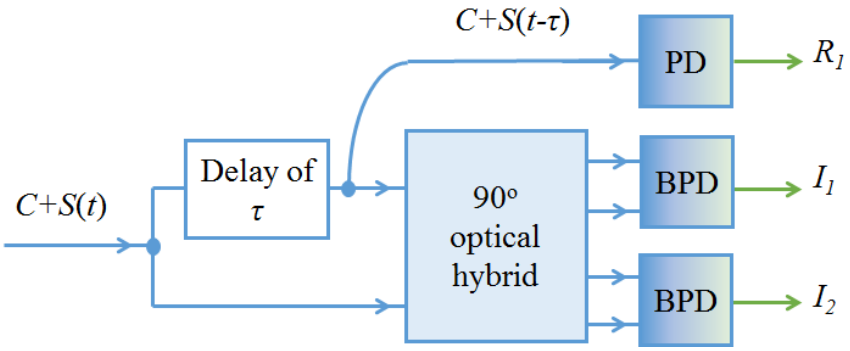

Fig. 4.2 Conceptual diagram of CADD receiver.

recovered. The information-bearing signals along with the carrier are fed into the CADD receiver. The input signals are split into two paths using a 3-dB optical coupler, and an optical delay line is implemented in one path with well-designed length which will be discussed in the next section. After the optical delay line, another optical coupler is used to split delayed signals, and then one path is fed into a single-ended PD. The original and delayed signals are fed into a 90-degree optical hybrid followed with a pair of BPDs. Given that the carrier is a CW, which is denoted as C, the information-bearing signals are denoted as $S(t)$, the input of the single-ended PD can be expressed as $C + S(t-\tau)$, and two inputs of the optical hybrid are $C + S(t)$ and $C + S(t-\tau)$, respectively. As such, three photocurrents shown in Fig. 4.2 are given by

$$
\begin{aligned}
R_1 &= \left|C + S(t-\tau)\right|^2 \\
&= \left|C\right|^2 + \left|S(t-\tau)\right|^2 + C[S(t-\tau) + S^*(t-\tau)] \\
I_1 &= 4\,\mathrm{Re}\{[C + S(t-\tau)]^* \cdot [C + S(t)]\} \\
I_2 &= 4\,\mathrm{Im}\{[C + S(t-\tau)]^* \cdot [C + S(t)]\}
\end{aligned}
\tag{4.4}
$$

where the responsivity of single-ended PD and BPDs are assumed to be 1, Re{} and Im{} represent the real and imaginary parts of a complex value, respectively. The working principle of CADD receiver consists of two steps, first is recovering the DSB signals using above-mentioned three photocurrents, then SSBI needs to be mitigated. The first step is analogous to coherent detection, two photocurrents given by the pair of BPDs are summed as follows

$$
I_1 + jI_2 = 4[C + S(t-\tau)]^* \cdot [C + S(t)] \tag{4.5}
$$

We introduce R_2 to replace $I_1 + jI_2$

$$
\begin{aligned}
R_2 &= (I_1 + jI_2)/4 \\
&= \left|C\right|^2 + C[S(t) + S^*(t-\tau)] + S(t) \cdot S^*(t-\tau)
\end{aligned}
\tag{4.6}
$$

To be strict, the carrier and information-bearing signal field C and S should be given by $Ce^{j2\pi f_0 t}$ and $Se^{j2\pi f_0 t}$, respectively, where f_0 represents the carrier frequency. The common phase term existing in R_2 can be easily compensated using the DSP, and here for the sake of presenting the CADD scheme in a concise manner, the common phase term is not displayed in the equations. Both R_1 and R_2 contain the DC term, and the DC term can be cancelled using

$$
\begin{aligned}
R &= R_2 - R_1 \\
&= C[S(t) - S(t-\tau)] + S_2(t)
\end{aligned}
\tag{4.7}
$$

where $S_2(t)$ represents the SSBI distortions for CADD receiver,

$$
S_2(t) = S(t)S^*(t-\tau) - \left|S(t-\tau)\right|^2 \tag{4.8}
$$

It is worth noting that SSBI in the CADD scheme distinguishes from the SSBI in the SSB based direct detection schemes as discussed in the previous chapter. The first term on the right-hand side of Eq. (4.7) is the desired term, which is amplified by the carrier.

Consequently, when a sufficiently strong carrier is transmitted along with the signal, the second-order distortion impacts could be negligible. Otherwise, assuming SSBI can be estimated and removed, the desired term can be expressed as

$$S(t)-S(t-\tau)=\frac{R-S_2(t)}{C} \tag{4.9}$$

and the information-bearing signals can be recovered in the frequency domain using Eq. (4.10)

$$\begin{aligned} S(f) &= \frac{1}{1-e^{j2\pi f\tau}}\mathrm{F}\{\frac{R-S_2}{C}\} \\ &= \frac{1}{H(f)}\mathrm{F}\{\frac{R-S_2}{C}\} \end{aligned} \tag{4.10}$$

where $S(f)$ denotes the information-bearing signal in the frequency domain, and the Fourier transform function is denoted as Φ{}. The transfer function of CADD receiver is $H(f)$ as shown in Eq. (4.10). which is the core function to recover the DSB signal in the frequency domain. Consequently, the multi-carrier OFDM modulation intrinsically fits for the CADD scheme. Even with SSBI, the field of DSB signals has been recovered as shown in Eq. (4.10).

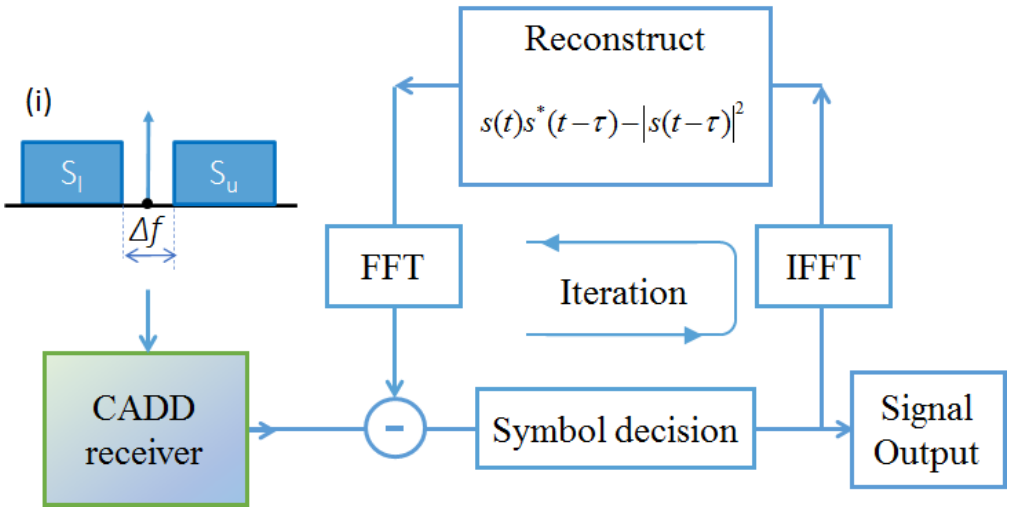

Fig. 4.3 DSP flow chart for CADD receiver. Inset(i) is the spectrum of DSB signals, where S_l and S_u are the lower and upper sideband signals, respectively. FFT: fast Fourier transform. IFFT: inverse fast Fourier transform.

When the CSPR is not sufficiently high to neglect second-order distortions, SSBI needs to be estimated and subtracted from the received signals as shown in Eq. (4.10). The specific DSP flow chart of SSBI mitigation used for CADD receiver is illustrated in Fig. 4.3, which is the second step of CADD receiver working procedure. The inset of Fig. 4.3 is the spectrum of DSB signals with a small guard band in the vicinity of the carrier frequency. The bandwidth of the guard band can be merely 10% of the information-bearing signal bandwidth. The functions of implementing guard band are twofold, accommodating partial SSBI and avoiding the null point of the transfer function. For the narrow frequency gap used in CADD, (e.g., merely 10% of the signal bandwidth) SSBI overlaps with the information-bearing signals in the frequency domain. Although there exist SSBI distortions, preliminary symbol decisions are made. For the iteration, symbol decisions made in the frequency domain are transformed into the time domain via IFFT, SSBI are then reconstructed using the formula shown in Fig. 4.3. Since the output of the transfer function for CADD receiver is the frequency-domain recovered signals, the time-domain reconstructed SSBI needs to be transformed into the frequency domain via FFT, and then subtracted from R as shown in Eq. (4.10). After the subtraction of SSBI, the symbol decision is made again to accomplish one iteration. It is reasonable to expect at some certain CSPRs after the first-time SSBI cancellation as discussed above, the system performance can be improved. After several iterations, namely, iterative cancellation of SSBI, when the system performance finally converges, the process of iterative SSBI cancellation can be terminated.

It is worth noting that the structure of CADD receiver shown in Fig. 4.2 can be simplified. For example, the optical hybrid can be replaced using a 3×3 optical coupler [155]. For the photonics integrated circuit (PIC) such as silicon photonics, the number of required PDs (e.g., three PDs used for the CADD receiver) is not the dominating factor of the total cost compared with the electrical bandwidth of the circuit. Compared with SSB based direct detection as discussed in Chapter 3, the implementation of two more PDs into the PIC does not predominantly increase the system cost but doubling the receiver bandwidth would.

4.3. Simulation and experimental demonstration of CADD

4.3.1. Transfer function for CADD

The transfer function $H(f)$ for CADD scheme shown in Eq. (4.10) is depicted in Fig. 4.4, where the optical delay is set to be 50 ps. At some frequencies, the magnitude of the transfer function is zero, leading to the singularity which needs to be avoided. Since $H(f=0)=0$, SSBI distortions and the noise is severely amplified in the vicinity of zero frequency, a small guard band is required between the lower and upper sideband. Besides the zero frequency, at the frequencies of ±20 GHz (1/50 ps=20 GHz) another two null points are observed, and such null points are inevitable since the transfer function equals to zero when $f\tau = 1,2, etc$. It is expected that such null points bring in severe distortions at these frequencies, and hence the information-bearing signal frequency region should be deliberately designed in two ways: tuning the frequency gap in the vicinity of zero frequency and adjusting the length of optical delay.

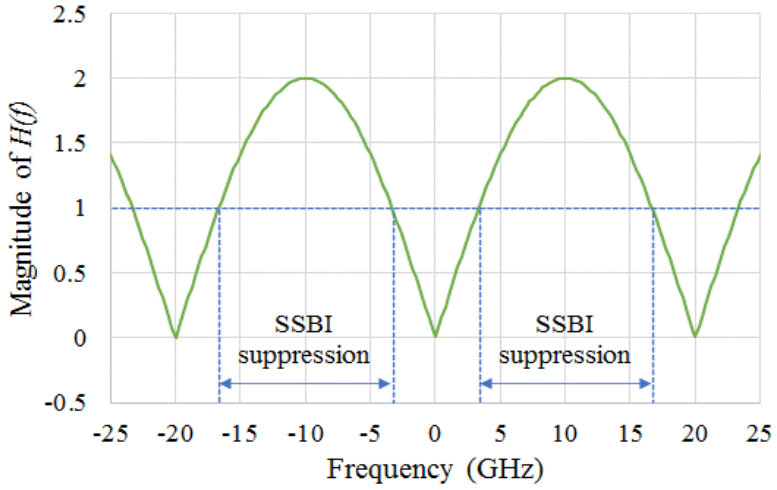

Fig. 4.4 Magnitude of transfer function H(f) for CADD with the optical delay of 50 ps. SSBI suppression is defined as |H(f)|>1.

When $|H(f)|>0$, SSBI is suppressed via the transfer function, and such frequency region is illustrated as SSBI suppression region in Fig. 4.4. As such, for the 50-ps optical delay it is desirable to allocate signals in the frequency region of [-16.6 GHz, -3.4 GHz] and [3.4 GHz, 16.6 GHz]. It can be concluded that the frequency gap between two sidebands serves as two functions: (i) SSBI at low frequency is more

severe than that in the high frequency region, and hence the frequency gap in the vicinity of zero frequency can accommodate parts of severe SSBI; (ii) the frequency gap is helpful to assign information-bearing signals into the SSBI suppression region rather than the region with singularity induced by the null point of transfer function.

4.3.2. Length of optical delay

The transfer function for CADD scheme is a function of the optical delay τ, and the optical delay determines the frequency of null points. The principle of designing CADD receiver is allocating signals into the SSBI suppression region, which involves

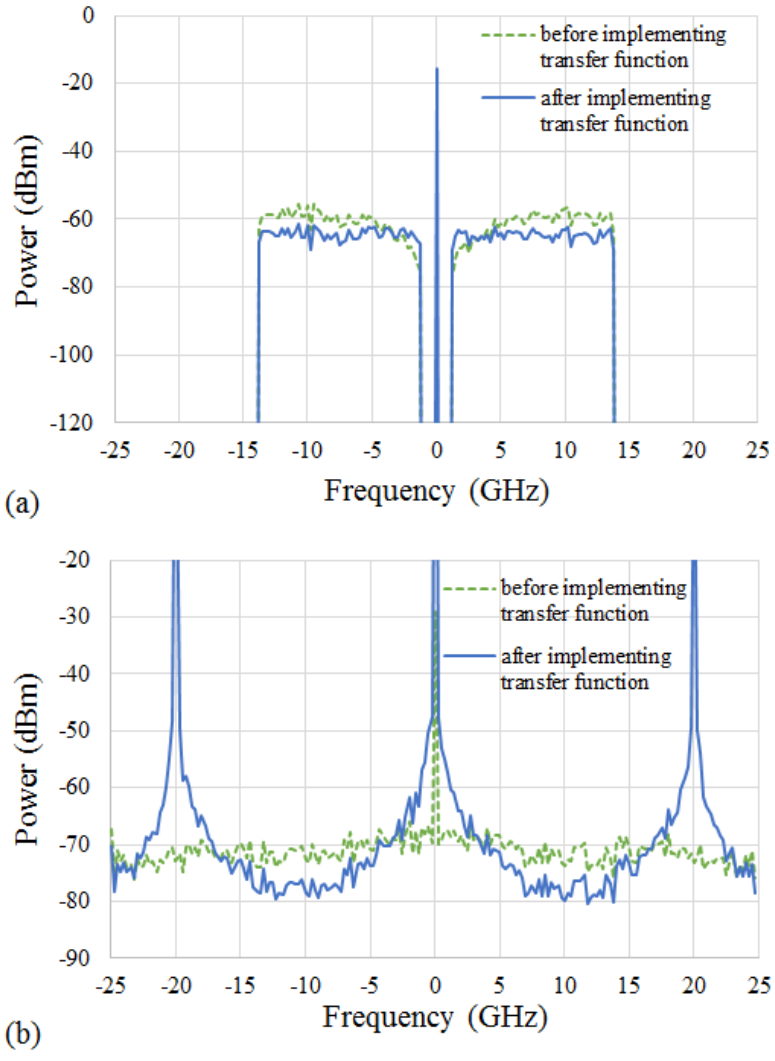

Fig. 4.5 (a) Signal spectra before and after implementing transfer function H(f). (b) SSBI spectra before and after implementing transfer function H(f).

the interplay between the frequency gap and the optical delay. To investigate the impacts of optical delay, the frequency gap is set to be 2.5 GHz, and the Monte Carlo simulation of 25-Gbaud QAM16 OFDM signals with the sampling rate of 50 Gsample/s is conducted. As such, the frequency gap merely occupies 10% of the signal bandwidth, and signals occupy the frequency region of [-13.75 GHz, -1.25 GHz] and [1.25 GHz, 13.75 GHz]. The spectrum of signal before implementing the transfer function (e.g., $S(t) - S(t-\tau)$) is illustrated in Fig. 4.5(a), and the signal after implementing the transfer function (e.g., $S(t)$) is the blue curve shown in Fig. 4.5(a). To verify the SSBI can be suppressed in some frequency regions, the spectra of SSBI are depicted in Fig. 4.5(b). It is shown that after implementing the transfer function,

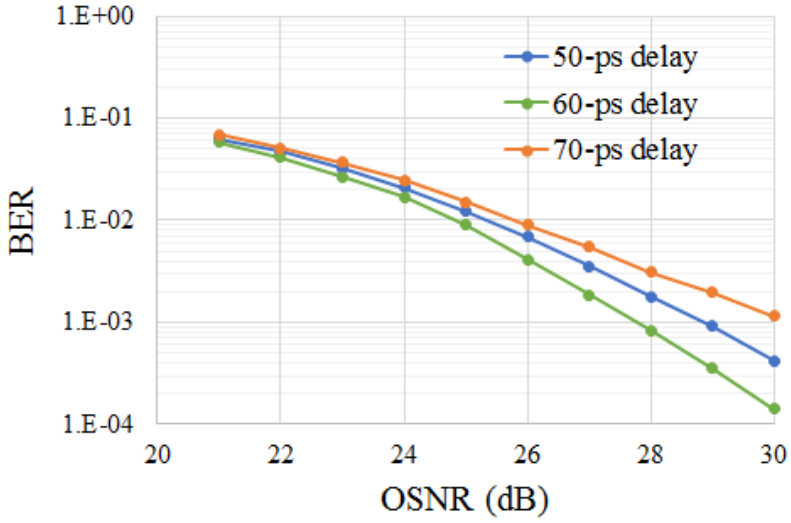

Fig. 4.6 BER performance versus OSNR with varying optical delays.

the power of SSBI is suppressed by up to 6 dB at the frequency region of [-16.7 GHz, -3.3 GHz] and [3.3 GHz, 16.7 GHz]. Besides, at the frequency of 0 and ±20 GHz the severely enhanced distortions are observed, which indicates the guideline of designing signal frequency region. To study the impacts of optical delay, the CSPR is set to be 8 dB, and four iterations of SSBI iterations are conducted. The BER as a function of OSNR with various optical delays is depicted in Fig. 4.6. For the definition of OSNR, since the carrier is transmitted along with the information-bearing signals from the transmitter, the power of both carrier and information-bearing signals is regarded as 'signal' power while calculating OSNR. Fig. 4.6 shows that the optimal delay is 60 ps. Compared to the 50-ps delay, the slope of 60-ps transfer function around zero

frequency is steeper, which fits better for the 2.5-GHz frequency gap. The phenomenon of existing an optimal optical delay can be explained as follows: when the optical delay line is too short, the SSBI suppression region moves to higher frequency which indicates the bandwidth of frequency gap should be wider; if the optical delay line is too long, the second null point of the transfer function is shifted to low frequency region, as such, the bandwidth to accommodate the information-bearing signals shrinks. Correspondingly, the length of optical delay line needs to be carefully designed to obtain the superior system performance.

4.3.3. Optimal CSPR

Before optimizing the CSPR for CADD receiver, the iteration number needs to be clarified. The BER performance versus iteration number is shown in Fig. 4.7 with the

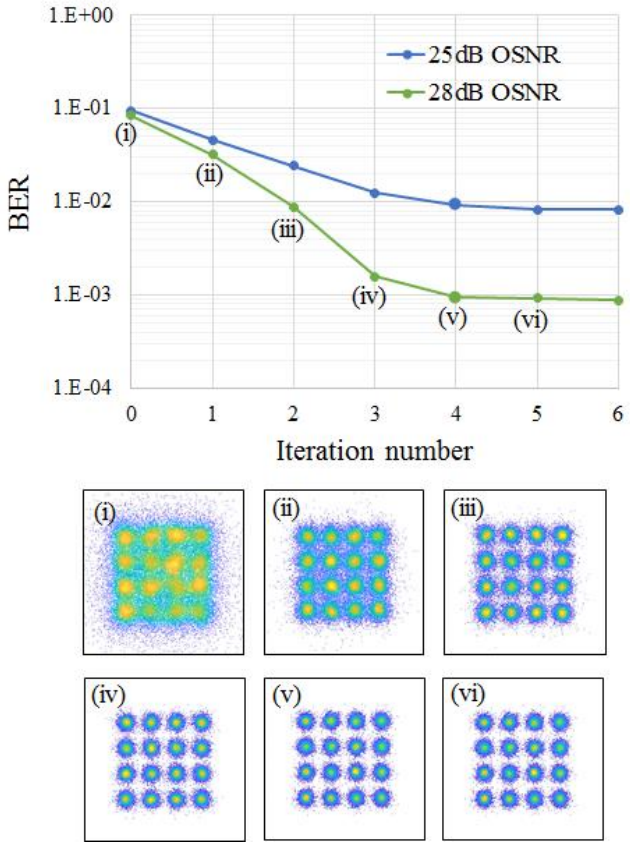

Fig. 4.7 BER as a function of iteration number for 25-Gbaud QAM 16 signals @ CSPR of 8 dB, optical delay of 60 ps, and frequency gap of 10%. Insets are the corresponding constellations for each iteration @ OSNR=28 dB.

corresponding constellations. When SSBI is not cancelled, the iteration number is zero. For the 25-dB OSNR, the first three iterations bring in the improved performance evidently, and the fourth iteration of SSBI cancellation still results in the marginal improvement. Similar phenomenon is observed for the 28-dB OSNR, the first four iterations have mitigated SSBI effectively, and more iterations do not bring in extra improvement, and hence it is reasonable to conduct four iterations for 25-Gbaud QAM16 signals.

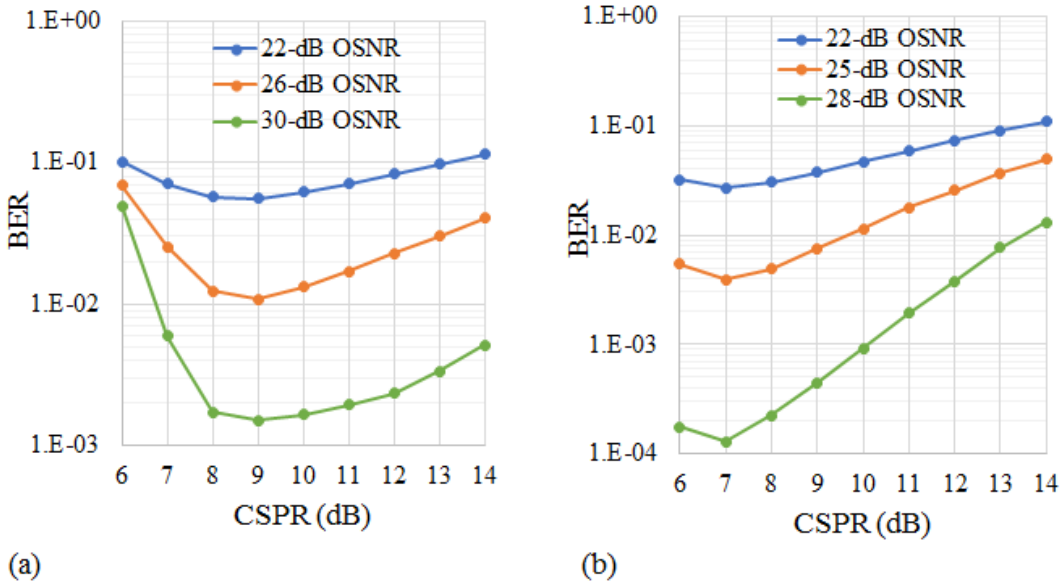

Fig. 4.8 BER versus CSPR for 25-Gbaud signals (a) with 5% frequency gap, (b) with 20% frequency gap.

After optimizing the length of optical delay line for the signals with certain bandwidth, CSPR is another factor to be optimized. For a given frequency gap, the CSPR is swept from 6 to 14 dB with the step size of 1 dB, as shown in Fig. 4.8 CSPR evidently affects the system performance. Although a low CSPR is desired since the carrier does not transmit any information, desired term $S(t) - S(t-\tau)$ is not sufficiently amplified by the strong carrier and the SSBI distortions cannot be ignored. As such, the preliminary symbol decisions are not accurate and the SSBI iterative cancellation is not effective, which limits the system performance. For the high CSPR circumstance, the power of information-bearing signals is relatively small, and signals become more sensitive to noise, leading to the poor performance. Consequently, there

exists an optimal CSPR value. For the 5% frequency gap case, the 25-Gbaud DSB signals are in the frequency region of [-13.125 GHz, -0.625 GHz] and [0.625 GHz, 13.125 GHz]. When OSNR is 30 dB, the optimal CSPR is found to be 9 dB as shown in Fig. 4.8 (a). For lower OSNRs, the optimal CSPR gradually decreases. That is because at low OSNRs, the SSBI distortions are not the predominant factor limiting the system performance, and the enhancement of desired term using a high CSPR to combat SSBI impacts does not bring in evident improvements, namely, for low OSNRs the optimal CSPR is lower than that for high OSNRs. For the wide frequency gap (e.g., 20% of the signal bandwidth) shown in Fig. 4.8 (b), the optimal CSPR is found to be 7 dB, indicating a wide frequency gap helps relax the requirement of large CSPRs. In other words, there exists a trade-off between the high spectral efficiency and required CSPRs.

4.3.4. Simulated OSNR sensitivity

As discussed above, the optical delay and CSPR are two parameters which require optimization for a certain frequency gap. Accordingly, to study the system performance of CADD receiver, the optimal optical delay and CSPRs for each frequency gap are shown in Table 4.1.

Table 4.1 Optimal delay and CSPRs for 25-Gbaud 16 QAM signals with each frequency gap.

Frequency gap	Optical delay	CSPR
5%	60 ps	9 dB
10%	60 ps	8 dB
15%	60 ps	8 dB
20%	50 ps	7 dB
25%	50 ps	7 dB

When the frequency gap is small, it requires the optical delay to be large and hence the slope of the transfer function is steep in the vicinity of zero frequency, which suppresses the bandwidth of SSBI enhancement region. Meanwhile, the small

frequency gap requires a relatively large CSPR, for example, the optimal CSPR is 9 dB for 5% frequency gap, while the optimal CSPR is 7 dB for a wide frequency gap (e.g., 25% gap) with the optimal optical delay decreasing from 60 ps to 50 ps. The decrease of optical delay is due to the interplay of frequency gap and SSBI suppression. Since a wide guard band is inserted between two sidebands, the information-bearing signals are allocated in the relatively high frequency region. Accordingly, the optical delay becomes smaller to enable the signals are in the SSBI suppression region rather than the SSBI enhancement region.

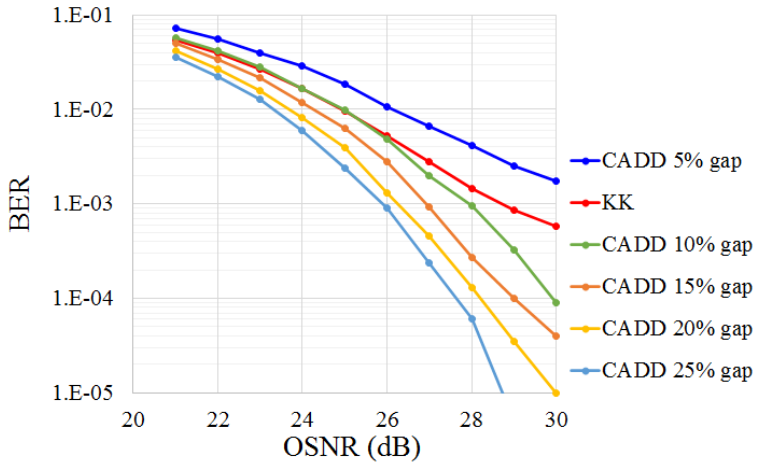

Fig. 4.9 OSNR sensitivity of CADD and KK receiver with varying frequency gaps at back-to-back.

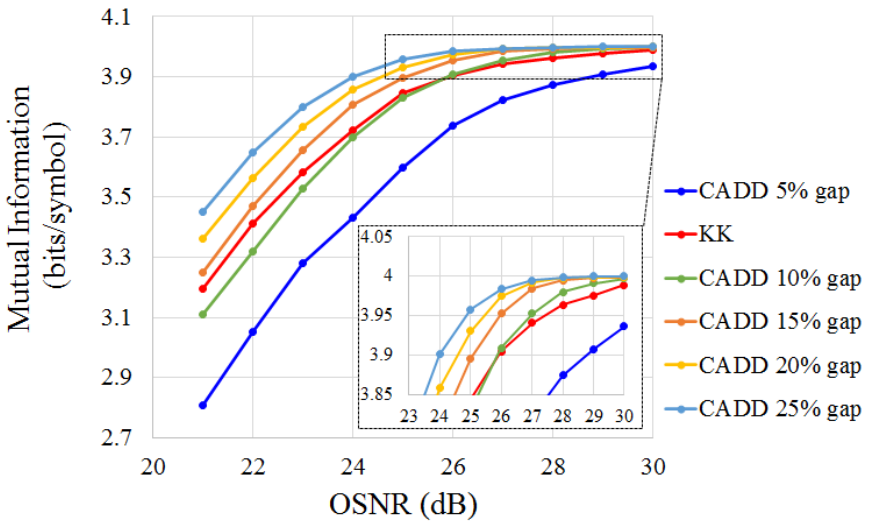

Fig. 4.10 Mutual information of CADD and KK receiver with varying frequency gaps at back-to-back.

The Monte Carlo simulation of 25-Gbaud QAM16 OFDM signals is conducted to investigate the performance of CADD receiver. The CADD receiver is designed for the DSB signals, and to make a comparison with SSB case, KK receiver is selected as a representative scheme of SSB signals. Since the KK relation requires the high oversampling rate, for the KK receiver the sampling rate is set to be 100 Gsample/s, while the sampling rate for CADD scheme is 50 Gsample/s. The bit rate of DSB and SSB signals are 100 Gb/s, and the corresponding detection scheme is CADD and KK receiver, respectively. The modulation format for the CADD receiver is multi-carrier OFDM since the characteristic of the transfer function inherently fits for OFDM signals, while single-carrier modulation is adopted for the KK receiver due to the low PAPR of single-carrier signals. The optical delay and CSPRs utilized for the CADD scheme simulation are the optimal values shown in Table 4.1, and the optimal CSPR for KK receiver is 6 dB. For both DSB and SSB signals, no optical filters are implemented. The OSNR sensitivity of two receiver schemes are shown in Fig. 4.9. Simulation results show that both CADD and KK receiver schemes are effective of mitigating SSBI. For the 100-Gb/s DSB signals with merely 1.25-GHz frequency gap (corresponding to 5% frequency gap), CADD scheme still works properly. When the requirement of high spectral efficiency is alleviated, for the 10% gap case, the OSNR sensitivity is 28 dB at the BER threshold of 1×10^{-3}. If the inserted frequency gap were wider, the OSNR sensitivity can be further improved. For example, when the frequency gap is 25%, around 2-dB OSNR improvement is obtained compared with the 10% gap circumstance. Although the system sensitivity of CADD scheme can be further improved by inserting a wider guard band, the sacrifice of spectral efficiency violates the original intention of developing DSB signal field recovery via direct detection. The mutual information (MI) of both CADD and KK schemes is depicted in Fig. 4.10, and the inset shows the zoom-in MI at high OSNR regions.

Given that the transfer function is nonuniform and the signal may not be perfectly allocated within the SSBI suppression region, it is desirable to investigate the SNR over the signal bandwidth. For the 25-Gbaud OFDM signals with 10% frequency gap, the SNR as a function of the frequency is presented in Fig. 4.11, where the frequency gap corresponds to the region of [-1.25 GHz, 1.25 GHz], and the SNRs of two

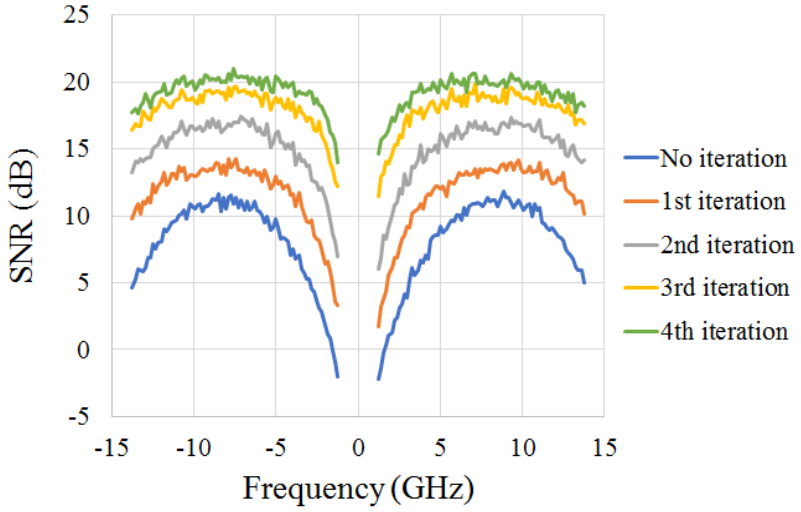

Fig. 4.11 SNR versus frequency for 25-Gbaud signals with 10% frequency gap, 60-ps optical delay, 8-dB CSPR, and 30-dB OSNR.

sidebands are given. When no iteration of SSBI cancellation is conducted, the SNR curve agrees well with the transfer function. The SNR in the SSBI suppression region is evidently higher than that in the SSBI enhancement region. The lowest SNR appears in the vicinity of zero frequency, which is coincident with the fact that SSBI is more severe at low frequency regions. After employing SSBI iterative cancellation algorithm, the SNR over the whole signal bandwidth gradually increases, moreover, the colored-SNR characteristic of SNR distribution is correspondingly mitigated. This phenomenon can be explained as follows, the symbol decisions are made in the frequency domain for OFDM signals, and SSBI is reconstructed in the time domain, indicating the low correlation between the symbol decisions and reconstructed SSBI, and hence the second-order distortions can be effectively mitigated. This low correlation alleviates the colored-SNR phenomenon and empowers the efficiency of iterative cancellation. It is noticed that the fourth iteration does not bring remarkable SNR improvement compared to the first two iterations, and this phenomenon is in line with the results shown in Fig. 4.7. After four iterations, the average SNR is 19.7 dB, and the lowest SNR in the vicinity of zero frequency is around 15 dB. It is worth mentioning that the colored-SNR characteristic can be alleviated by inserting a wider frequency gap.

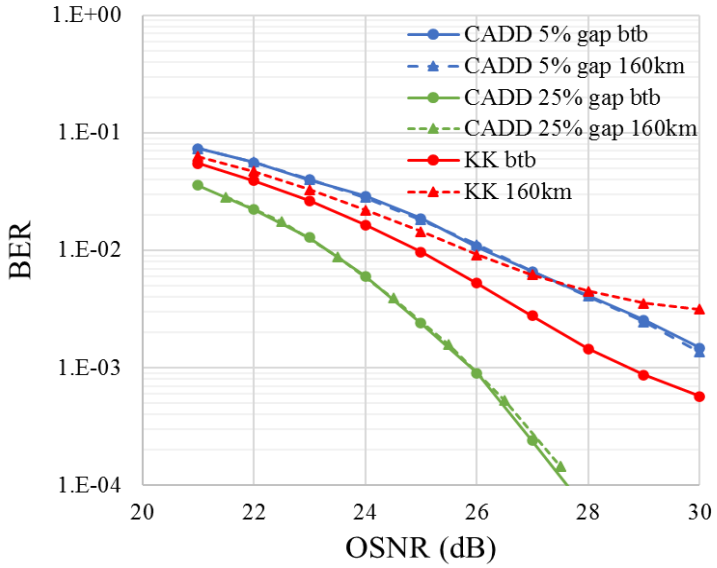

Fig. 4.12 Transmission performance of CADD and KK receivers with each optimal parameter.

The transmission performance of CADD receiver is displayed in Fig. 4.12.The transmission over 160-km SSMF with the CD of 17 ps/(nm×km) is emulated. Since the CADD scheme is capable of recovering the optical field, CD can be digitally compensated at the receiver. Simulation results show that the BER curves at back-to-back and after 160-km transmission are overlapped, indicating the CADD receiver is not sensitive to CD even with 5% guard band. While for the KK receiver, although the CD is also digitally compensated using the recovered field information, after 160-km transmission the PAPR of signals increases, which leads to the degradation of system performance after transmission.

The system performance of DSB based CADD receiver and SSB based KK receiver has been presented and discussed. More generally, several state-of-the-art schemes realizing field recovery via direct detection and coherent detection schemes are in a good position to make a comparison. For the various detection schemes shown in Table 4.2, the bit rate is 200 Gb/s per polarization per wavelength and the OSNR is set to be 30 dB. In terms of required bandwidth per ADC, the homodyne coherent is superior to the other schemes. For the homodyne coherent, two ADCs are required, and heterodyne coherent merely needs one ADC, however, heterodyne coherent requires twice the receiver bandwidth, which significantly increases the system cost.

Table 4.2 Cost metrics of 200-Gb/s net interface rate per wavelength per polarization detection systems with field recovery. This table is reproduced from ref [97], and OSNR is set to be 30 dB. BW: bandwidth

	BW per ADC (GHZ)	Requirement of stable lasers	Number of ADCs
Coherent (homodyne)	9.7	Yes	2
Coherent (heterodyne)	19.4	Yes	1
CADD	16.0	No	3
KK	31.6	No	1
Stokes	25.1	No	3
Gapped SSB	50.2	No	1
Interleaved SSB	50.2	No	1

As the required receiver bandwidth is the predominant factor of the system cost compared with the number of components, homodyne coherent systems rather than heterodyne coherent systems have been widely adopted in field-deployed coherent systems. Analogous to homodyne over heterodyne in coherent detection, the CADD scheme which requires around half of the receiver bandwidth compared with SSB based schemes is a novel promising direct detection scheme.

For the implementation cost of PIC, the optoelectronic bandwidth and whether a coherent laser is needed or not are two predominant factors. The first concern of optoelectronic bandwidth can be addressed by using DSB rather than SSB modulation, and the second concern of the coherent laser can be addressed by using direct detection. Consequently, the DSB modulation based CADD scheme is in a great position to be implemented in the PIC. From the perspective of practical implementation scenarios (e.g., data center interconnections), for coherent receiver the utilization of LO not only increases the system cost as a hardware component but also contributes to the complicated DSP including LO frequency offset estimation and carrier phase estimation, which leads to high power consumption [156]. Compared with the homodyne coherent receiver, the CADD scheme and SSB based direct detection

schemes do not require the LO, which makes both schemes suitable for cost-sensitive transports in terms of both system cost and power consumption. Accordingly, field recovery schemes via direct detection fills the gap between conventional IMDD and conventional systems, namely, both CADD and SSB based direct detection schemes tactfully strike the balance between the system cost and performance [157][158].

4.3.5. Experimental demonstration and results

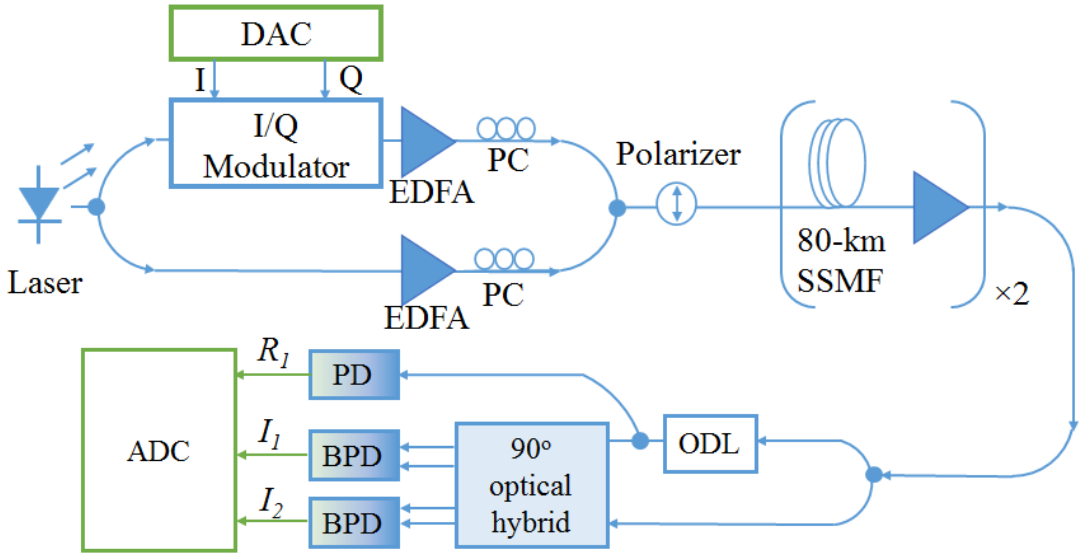

Fig. 4.13 Experimental setup for CADD scheme.

Experimental demonstration of the proposed CADD scheme has been carried out to reveal the capability of DSB signal field recovery via direct detection. The experimental setup is depicted in Fig. 4.13. The pseudo-random bit sequence is mapped to QPSK signals, and then loaded into 900 subcarriers out of 1000 to obtain 54-Gb/s OFDM signals. To enhance the spectral efficiency, the CP is not employed. Since the channel response may be not uniform over the signal bandwidth, compensation of the channel response without the impacts of SSBI is indispensable. As such, six OFDM training symbols are used, with signals only loaded in the odd-numbered subcarriers and null even-numbered subcarriers. After the CADD detection, SSBI is allocated onto the even-numbered subcarriers with no impacts on odd-numbered subcarriers. The channel response can be estimated from the information-bearing odd-numbered subcarriers. The frequency gap inserted between two sidebands

of the 54-GB/s signals is 4.86 GHz. An external-cavity laser is used for the light source, and the transmitter for the CADD scheme consists of two optical paths, an IQ

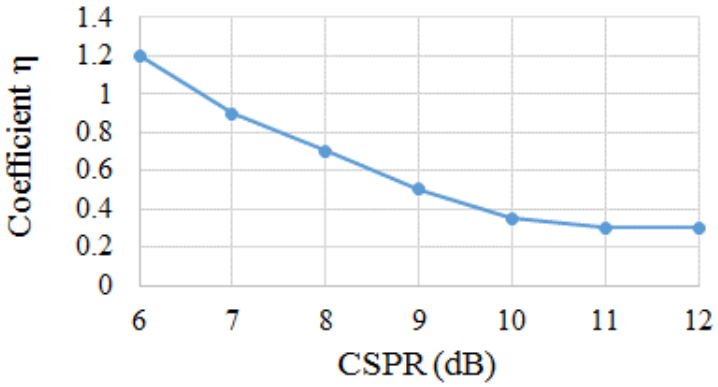

Fig. 4.14 Scaled coefficient η used in the experimental demonstration versus CSPR.

modulator is implemented in one path and the other optical path provides the CW from the same laser, which serves as the carrier. Two EDFAs are employed in two paths, as such, various CSPRs can be obtained by tuning the gain of each EDFA. After the modulated signals and the carrier are combined using an optical coupler, a polarizer is used to guarantee signals and carrier are in the same polarization state. To validate the optical field recovery ability of CADD scheme, signals are transmitted over two spans of fiber, corresponding to 160 km, and CD is digitally compensated at the receiver side. Besides the tunable optical delay line and 90-degree optical hybrid, three matched BPDs are implemented at the receiver, and one of the BPDs is used as a single-ended PD. The sampling rate of the ADC is 80 GSa/s and the bandwidth is 33 GHz.

DSP used in the experimental demonstration generally follows with the flow chart shown in Fig. 4.3. It is worth noting that coefficient η is needed to scale the reconstructed SSBI. Since the symbol decisions for QPSK signals are ±1±1j, and the reconstructed SSBI using ±1±1j needs to be scaled according to the CSPR as displayed in Fig. 4.14. To be specific, when the CSPR is small, the portions of SSBI are relatively large. The optical power fed into the PDs is kept constant, while SSBI is reconstructed using the same ±1±1j regardless of the CSPR, and hence the coefficient η at small CSPRs should be large to subtract the relatively severe SSBI portions. As

the coefficient η is related to the oversample rate, received optical power and the responsivity of PDs, the value of η is scaled to around 1 in Fig. 4.14.

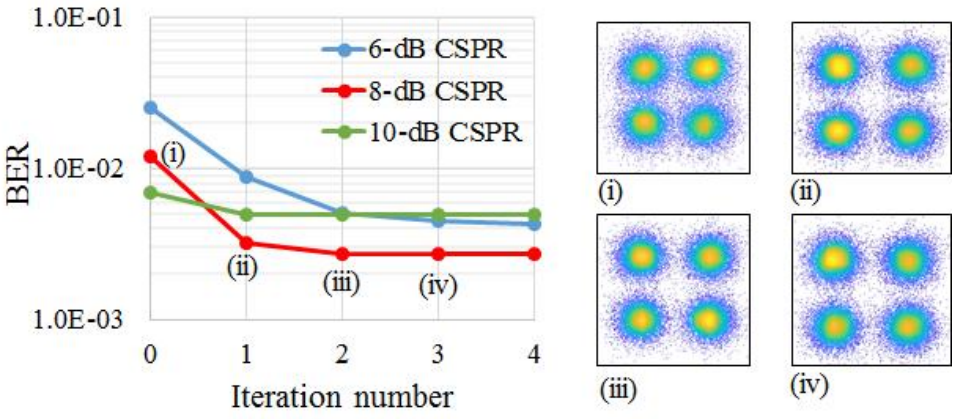

Fig. 4.15 BER versus the number of iterations for various CSPRs after transmission of 160-km SSMF. Insets (i-iv) are corresponding constellations for each iteration with the CSPR of 8 dB.

To identify the optimal CPSR in the experimental demonstration, CSPR is swept from 6 to 12 dB with the step size of 1 dB. After 160-km transmission over SSMF, the BER performance as a function of iteration number is shown in Fig. 4.15, and the insets display the corresponding constellations for the 8-dB circumstance after each iteration. At low CSPRs (e.g., 6-dB CSPR), system performance can be greatly improved after two iterations, the third and even fourth iteration can still bring in some marginal improvements. When CSPR is 10 dB, only the first iteration is effective in mitigating SSBI, from the second iteration sustainable improvements are not observed. That is because at high CSPRs, SSBI impacts on system performance are relatively small, and hence the effectiveness of SSBI iterative cancellation is limited. The optimal CSPR is found to be 8 dB as shown in Fig. 4.15, where the first two iterations provide evident improvements, which are also indicated by the corresponding constellations. For the optimal 8-dB CSPR, the third and fourth iterations do not present the necessity to be carried out, and thus it is reasonable to conduct two iterations of SSBI cancellation

The optimal CSPR is related to the BER threshold, as such, BER performance at various OSNRs is presented in Fig. 4.16(a). At 36-dB OSNR, the optimal CSPR is

around 8-9 dB. When OSNR decreases to 28 dB, the optimal CSPR shifts to 7-8 dB. This phenomenon agrees with the theoretical analysis in the previous sections, that is at low OSNRs the major limitation of the system is the optical noise rather than SSBI distortions. At the BER threshold of 4×10^{-3} shown in Fig. 4.16(b), the OSNR sensitivity is around 32 dB with the optimal CSPR of 8 dB.

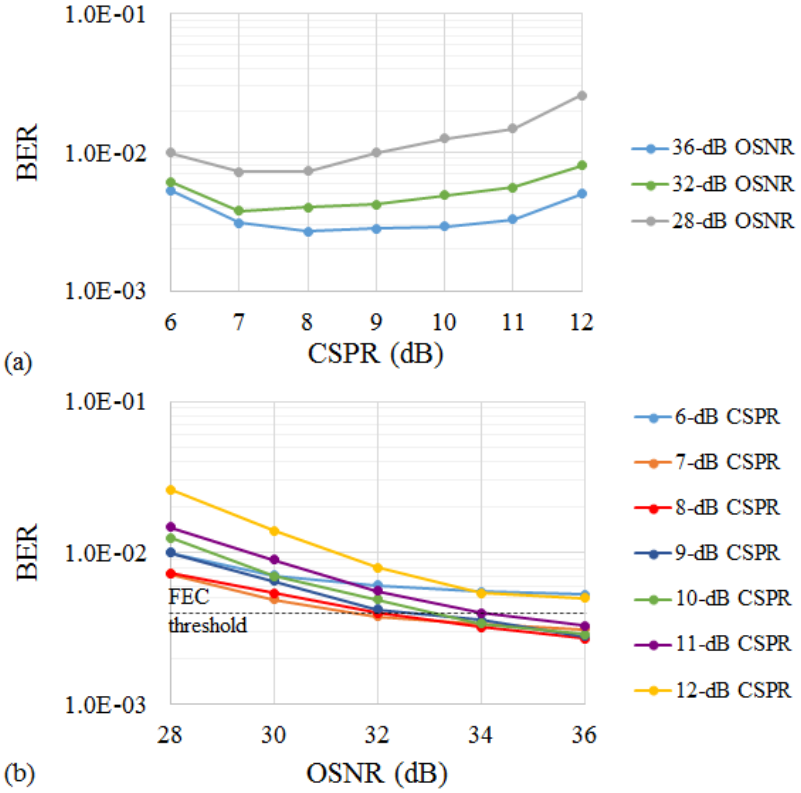

Fig. 4.16 (a) Optimization of CSPR at various OSNRs. (b) BER versus OSNR for various CSPRs.

To conclude, the transmission of 54-Gb/s DSB signals over 160-km SSMF has been demonstrated. The optical field has been successfully recovered via direct detection and CD is digitally compensated at the receiver side. Besides, compared to SSB based direct detection schemes, the required receiver bandwidth of proposed CADD scheme is reduced by 41%.

4.4. IQ imbalance impacts on CADD

As shown in Fig. 4.13, an IQ modulator is implemented at the transmitter for CADD scheme. From practical aspects, the IQ imbalance is a widely existing factor limiting the system performance. The IQ imbalance may stem from the I and Q paths

of electrical amplifiers, electrical cables, and the internal structure of IQ modulator [159-160]. When the frequency response of I and Q paths of these components is not identical, signals are degraded at the transmitter, which poses a tough task on the signal recovery especially when the IQ imbalance parameters are blind at the receiver side. The DSP of CADD scheme can be understood as two steps: obtain preliminary symbol decisions even with SSBI distortions and then conduct iterative SSBI mitigation. As such, it is highly desirable to study the impacts of IQ imbalance, and whether the iterative SSBI mitigation can work properly in the presence of IQ imbalance.

The degradation induced by IQ imbalance is that the mirror interference generated from one sideband would distort another sideband, and vice versa. For SSB signals, such mirror interference can be easily observed since one sideband should be null, however, both sidebands carry information for DSB signals. The IQ imbalance includes the amplitude and phase mismatch, and for CADD scheme the tolerance of both mismatches is investigated. The IQ imbalance model is built as follows, for the OFDM signals consisting of 2k subcarriers, R(-k) and R(k) are used to present the subcarriers in the lower and upper sideband, respectively. Correspondingly, the IQ imbalance distorted signals in the lower and upper sideband are denoted as $R_{iq}(-k)$ and $R_{iq}(k)$, which can be expressed as [161-162]

$$\begin{pmatrix} R_{iq}(k) \\ R_{iq}^{*}(-k) \end{pmatrix} = \begin{pmatrix} G_1(k) & G_2^{*}(k) \\ G_2(k) & G_1^{*}(k) \end{pmatrix} \begin{pmatrix} R(k) \\ R^{*}(-k) \end{pmatrix} \tag{4.11}$$

where G_1 and G_2 are IQ imbalance related parameters, containing amplitude imbalance denoted by $\alpha(k)$, and phase imbalance denoted by $\beta(k)$,

$$\begin{aligned} G_1(k) &= (1+\alpha(k)e^{j\beta(k)})/2 \\ G_2(k) &= (1-\alpha(k)e^{j\beta(k)})/2 \end{aligned} \tag{4.12}$$

Since the IQ imbalance is assumed to be linearly frequency dependent, the amplitude imbalance α is loaded from 0 to 30% mismatch over the frequency region of information-bearing signals, and the phase mismatch β is loaded from 0 to 0.2 rad. To investigate the tolerance of IQ imbalance, the above-mentioned IQ imbalance parameters are blind to the receiver and no IQ imbalance compensation algorithm is

implemented. The simulation of 25-Gbaud QAM16 OFDM signals using CADD receiver is carried out. Several optimal parameters used in the simulation are the CSPR of 8 dB and optical delay of 60 ps with the frequency gap of 2.5 GHz.

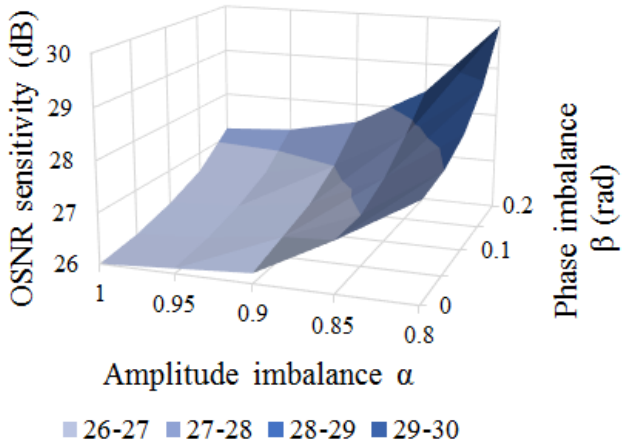

Fig. 4.17 OSNR sensitivity @BER=4×10^{-3} versus amplitude and phase imbalance.

Fig. 4.17 presents the OSNR sensitivity of CADD receiver in the presence of IQ imbalance, including both amplitude and phase imbalance. The BER threshold is set to be 4×10^{-3}, and the OSNR sensitivity is found to be 26 dB with no IQ imbalance. With the combination of amplitude and phase imbalance, for example, α equals to 80% and β equals to 0.2 rad, the OSNR sensitivity degrades to 30 dB.

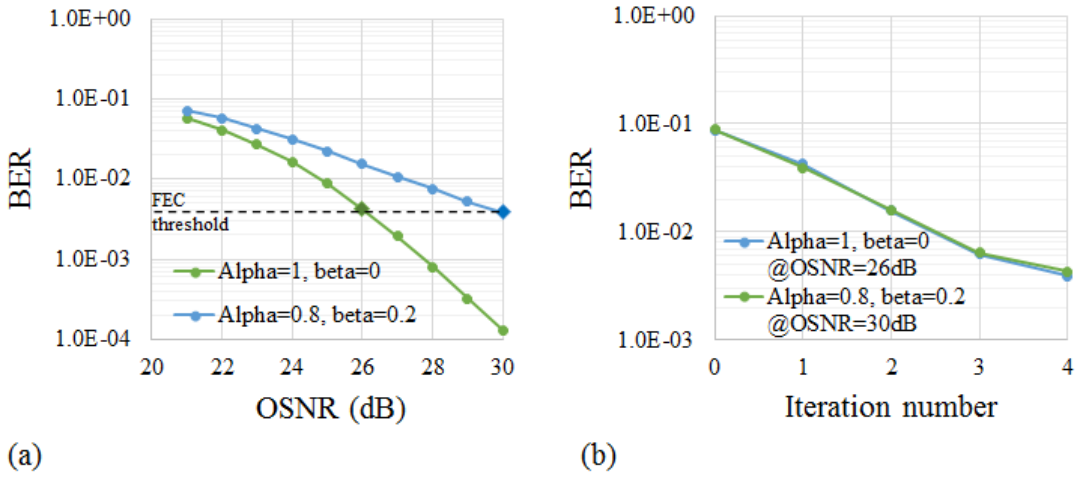

Fig. 4.18 (a) BER as a function of OSNR for the cases with no IQ imbalance (alpha=1, beta=0) and with IQ imbalance (alpha=0.8, beta=0.2), respectively. (b) BER as a function of iteration number for two bold diamond points shown in (a).

The BER performance of two cases (e.g., one with no IQ imbalance, one with α equals to 80% and β equals to 0.2 rad) is depicted in Fig. 4.18 (a). At the 7% FEC threshold, the OSNR penalty induced by IQ imbalance is up to 4 dB. To study the effectiveness of SSBI iterative cancellation in the presence of IQ imbalance, two diamond points with almost the same BER shown in Fig. 4.18 (a) are selected. The corresponding BER curve as a function of iteration number is depicted in Fig. 4.18 (b). The blue curve represents the circumstance with no IQ imbalance at 30-dB OSNR, and it is overlapped with the BER curve representing the case with amplitude mismatch parameter α of 0.8 and phase mismatch parameter β of 0.2 rad, indicating that iterative SSBI cancellation for CADD does not incur extra OSNR penalties due to the IQ imbalance, despite that both amplitude and phase mismatch degrades the system performance as a whole.

Chapter 5 Towards low CSPR for direct detection schemes

5.1. Introduction

For the field recovery of complex-valued signals via direct detection, the carrier is needed to obtain the beating term between the carrier and information-bearing signals, namely, the replica of modulated signals. A large CSPR is generally applied for both SSB based KK and IC receivers and DSB based CADD receiver to enable the acceptable system performance. However, no information is loaded on the carrier and it is preferable to enhance the information-bearing signal power rather than the carrier power. Besides the power efficiency issue, the high carrier power incurs nonlinear effects. Accordingly, it is highly desirable to relax the requirement of high CSPR. However, the minimum phase condition for the KK receiver is the limitation of CSPR, when the minimum phase condition is violated due to the low CSPR, KK relations cannot work properly. The high CSPR requirement also applies for the SSB based IC receiver, preliminary symbol decisions cannot be made accurately at low CSPRs, and hence degrades the effectiveness of SSBI iteration mitigation. The cause of required high CSPRs for DSB based CADD scheme is analogous to the IC receiver. In the recent years, the issue of high carrier power has attracted research interests and several novel algorithms have been proposed to deal with the high CSPR restrictions.

A modified KK receiver was proposed to reconstruct the field at low CSPRs [163-164]. The core of this scheme is applying an exponential operation to SSB signals, which enables the time trajectory of signals does not encircle the origin. To be specific, the DSP flow chart of this proposed modified KK receiver algorithm is shown in Fig. 5.1. The baseband signals are upconverted first, and then exponential operation is carried out. As such, the signals after exponential operation intrinsically do not encircle the origin, in other words, the minimum phase condition is satisfied. The CD impacts can be dealt with via pre-compensation using the known channel information (e.g., the transmission distance), or CP can be implemented. Experimental demonstration has

shown that the CSPR using this modified KK receiver scheme can be reduced by 2 dB compared with the conventional KK receiver.

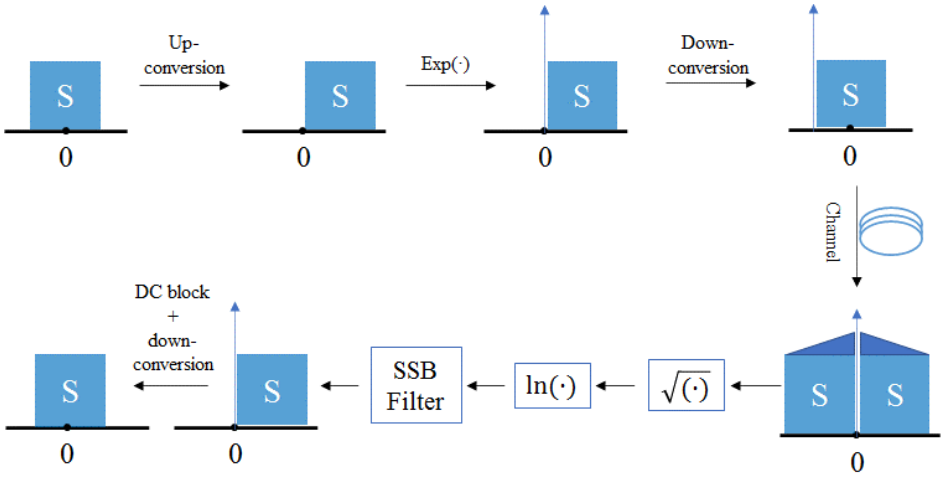

Fig. 5.1 DSP flow chart of the modified KK receiver scheme with the corresponding spectra.

For the DSB based CADD receiver, interleaved subcarrier loading scheme has been proposed to enable CADD scheme work properly at low CSPRs [165]. Analogous to the SSB based interleaved scheme, odd-numbered subcarriers with respect to the carrier are loaded with information and even-numbered subcarriers are intentionally set to be null for DSB signals. The corresponding spectrum is shown in

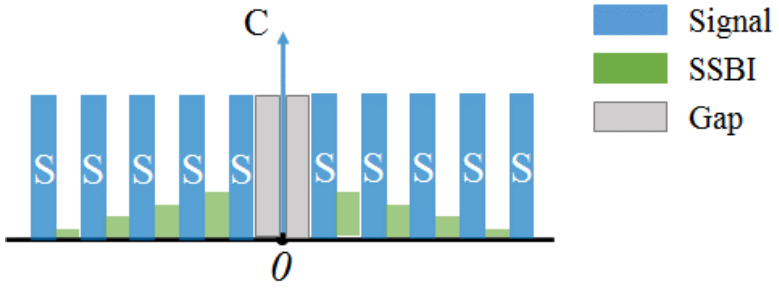

Fig. 5.2 Interleaved subcarrier loading for CADD receiver.

Fig. 5.2. Such loading scheme has two advantages, one is the SSBI induced by square-law detection allocates in the null even-numbered subcarriers, another one is that the required CSPR is low since it does not need a strong carrier to combat SSBI. Depending on the frequency gap in the vicinity of zero frequency, the CSPR can be as low as 0~3 dB. Although a wide frequency gap of 50% can be used to fully

accommodate SSBI, it is desirable to take the advantage of low-frequency region of components in the system since the frequency response of electrical or O/E components generally presents better than that in the high frequency region. Experimental results show that the optimal CSPR is merely 1.5 dB when the guard band is 25% of the signal bandwidth.

In this chapter, two novel algorithms are presented to reduce the required CSPR for SSB based direct detection schemes, and the power loading scheme is demonstrated to effectively deal with the colored-SNR issues for CADD receiver, and hence relax the requirement of high CSPR.

5.2. Enhanced SSBI mitigation

As discussed in Chapter 3, SSB based KK receiver relies on the minimum phase condition, which requires the time trajectory of signals does not encircle the origin, otherwise the field could not be recovered accurately. Besides, the O/E response has been demonstrated to affect the accuracy of the field reconstruction given by KK relations in the practical implementation [166-167]. Although a high CSPR can help weaken the impacts of SSBI, the power efficiency and high power induced nonlinearity are two concerns. Consequently, enhanced SSBI mitigation scheme is proposed and discussed in this section.

For the signal transmitted along with the carrier, $S = E_s e^{j\omega_s t}$ and $C = E_c e^{j\omega_c t}$ are used to represent the signal and carrier field, respectively. Upon the direct detection, assuming the responsivity of the PD is 1, the photocurrent can be expressed as

$$I = |C + S|^2 = |E_C|^2 + |E_S|^2 + E_C E_S e^{j(\omega_C - \omega_S)t} + E_C E_S e^{j(\omega_S - \omega_C)t} \tag{5.1}$$

SSB signals use either upper or lower sideband to load information. With the assumption of upper sideband is selected (e.g., $\omega_0 < \omega_s$), the desired term in Eq. (5.1) is $E_C E_S e^{j(\omega_S - \omega_C)t}$. When the minimum phase condition is fully satisfied, the desired term can be recovered via KK relations, while at low CSPRs distortions caused by the violation of minimum phase condition are involved. The distortions, namely, error signals are denoted as ΔE_S, and the distorted signals E_S' can be given by $E_S' = E_S +$

ΔE_S. Using the conventional KK algorithm, the recovered term containing the error signals is $E_C(E_S + \Delta E_S)e^{j(\omega_S - \omega_C)t}$. Compared with the desired term, the involved distortion D_1 is given by

$$D_1 = E_C \Delta E_S e^{j(\omega_S - \omega_C)t} \tag{5.2}$$

which is the distortion term for the conventional KK receiver at low CSPRs. Based on the KK algorithm, the enhanced SSBI mitigation is using the obtained symbol decisions to reconstruct SSBI and then subtracted from the original received photocurrent. The corresponding equation can be given as follows with the assumption of DC has been removed

$$I - \left|E_S{}'\right|^2 = E_C E_S e^{j(\omega_C - \omega_S)t} + E_C E_S e^{j(\omega_S - \omega_C)t} - \left|\Delta E_S\right|^2 - (E_S \cdot \Delta E_S^* + E_S^* \cdot \Delta E_S) \tag{5.3}$$

The first two terms on the right-hand side of Eq.(5.3) are two sidebands, and one SSB filter denoted by $\boldsymbol{L}[\cdot]$ can be utilized to obtain the desired sideband. With the filter, the rest terms become $E_C E_S e^{j(\omega_S - \omega_C)t} - \boldsymbol{L}[E_S \Delta E_S^* + E_S^* \Delta E_S]$ containing both the replica of signals and distortion term D_2, and D_2 is given by

$$D_2 = -\boldsymbol{L}\left[E_S \Delta E_S^* + E_S^* \Delta E_S\right] \tag{5.4}$$

which is the distortion of enhanced SSBI mitigation scheme. By comparing D_1 and D_2, the superiority of enhanced SSBI mitigation over conventional KK algorithm can be shown. The power ratio of D_1 and D_2 can be expressed by

$$\begin{aligned} \left|D_1\right|^2 / \left|D_2\right|^2 &= \left|E_0 \Delta E_s e^{j(\omega_s - \omega_0)t}\right|^2 \Big/ \left|-\boldsymbol{L}\left[E_s \Delta E_s^* + E_s^* \Delta E_s\right]\right|^2 \\ &= \left|E_0\right|^2 \left|\Delta E_s\right|^2 / 2\left|E_s\right|^2 \left|\Delta E_s\right|^2 = CSPR/2 \end{aligned} \tag{5.5}$$

In various reported demonstrations of the KK receiver, the optimal CSPR generally ranges from 6 to 12 dB, which is larger than 3 dB. Under such circumstance, it can be seen from Eq. (5.5) that the power of error signals given by conventional KK receiver is larger than the counterpart given by the proposed enhanced SSBI mitigation scheme. As such, with the same CSPR the proposed enhanced SSBI mitigation scheme can remove SSBI impacts more effectively, and from another prospective, the proposed scheme can work properly at lower CSPRs.

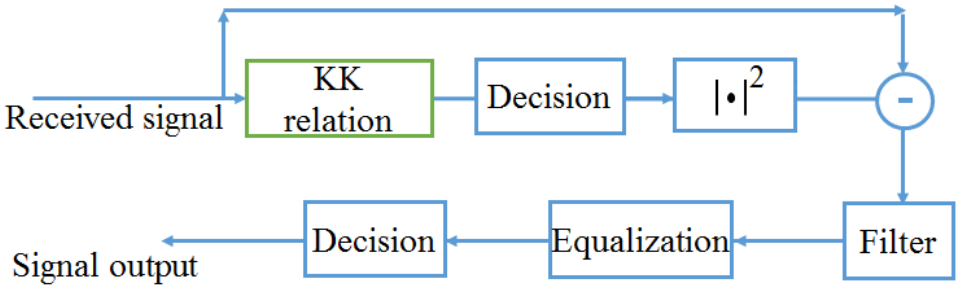

Fig. 5.3 DSP flow chart for the proposed enhanced SSBI mitigation scheme.

The signal processing for the proposed enhanced SSBI mitigation scheme is depicted in Fig. 5.3, where SSBI is reconstructed using the absolute square of preliminary symbol decisions. The subtraction operation in Fig. 5.3 denotes the processing shown in Eq. (5.3), after that, the SSB filter is implemented to obtain one of the sidebands. The equalization is implemented to deal with the channel response before making the final symbol decisions. After transmission over fibers, CD compensation and CD decompensation while reconstructing CD distorted SSBI are required.

To verify the effectiveness of enhanced SSBI mitigation scheme, experimental demonstration was conducted. The experimental setup is same as Fig. 3.10, and the Q-factor as a function of OSNR for various CSPRs is depicted in Fig. 5.4. At low

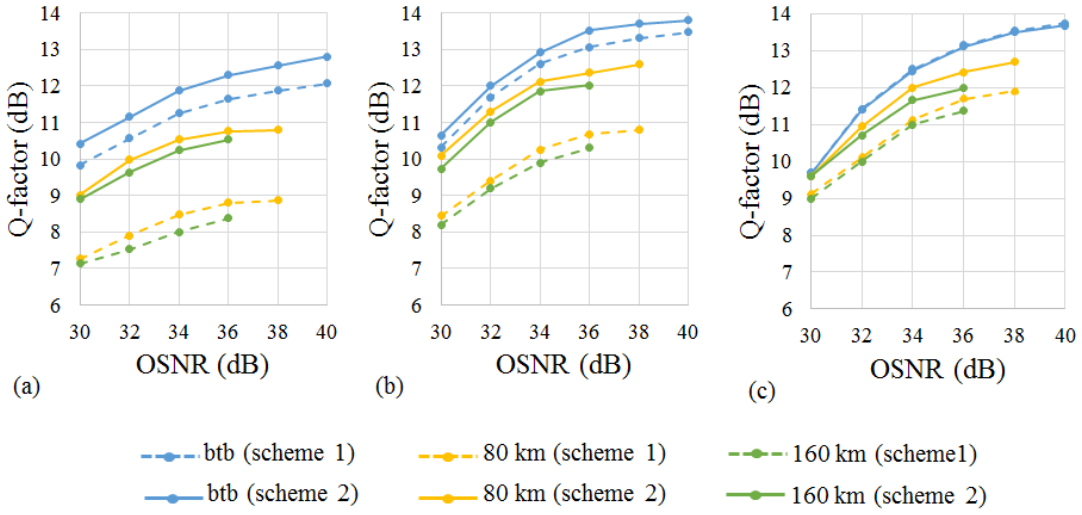

Fig. 5.4 Q-factor versus OSNR for different CSPRs. (a) 4-, (b) 6-, (c) 8-dB CSPR. Scheme 1: conventional KK receiver. Scheme 2: proposed enhanced SSBI mitigation based on KK relation.

CSPRs, for example, at 4-dB CSPR the Q-factor can be improved by using the proposed enhanced SSBI mitigation scheme for both btb and after transmission conditions. The improvement of Q-factor is more evident for the transmitted than the btb case. This phenomenon is attributed to the fact that even the minimum phase condition is satisfied at the transmitter, after transmission over 80/160-km fiber, the PAPR of signals increases and hence violates the minimum phase condition at the receiver side. When the CSPR is increased to 8 dB, the enhanced SSBI mitigation scheme does not provide Q-factor improvement at btb, but still can improve the system performance after 80- and 160-km transmission over SSMF.

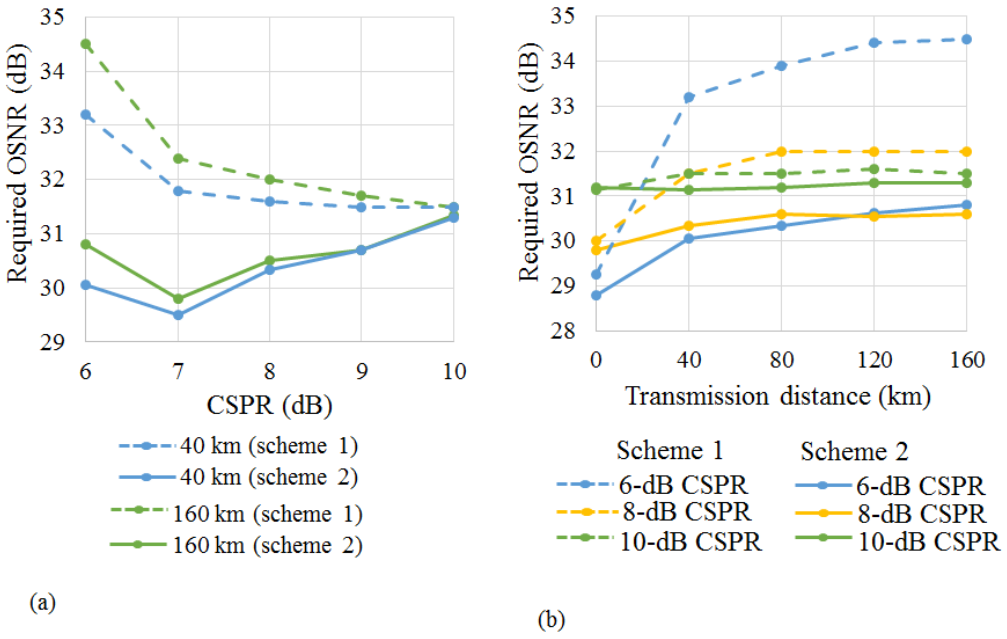

Fig. 5.5 (a)System performance after 40- and 160-km transmission. (b) Required OSNR as a function of transmission distance for various CSPRs. Scheme 1: conventional KK receiver. Scheme 2: proposed enhanced SSBI mitigation based on KK relation.

The BER threshold is set to be 1×10^{-3}, and the transmission performance using conventional KK and proposed enhanced SSBI mitigation scheme is illustrated in Fig. 5.5. As shown in Fig. 5.5 (a), after 40- and 160-km transmission the optimal CSPR for KK receiver is found to be 9-10 dB, while for the enhanced SSBI mitigation scheme the optimal CSPR is 7 dB for both 40- and 160-km transmission condition, which indicates the effectiveness of SSBI cancellation given by the proposed algorithm at

low CSPRs. Compared with the conventional KK receiver using relatively high CSPRs, the low CSPRs indicate more power is loaded to the information-bearing signals rather than the carrier, leading to the OSNR improvement. At each optimal CSPR, after transmission over 40- and 160-km SSMF, the OSNR can be improved by 1.9 and 1.7 dB, respectively. Besides, as illustrated in Fig. 5.5 (b) at low CSPRs the required OSNR for the conventional KK receiver increases as the transmission distance increases, and the enhanced SSBI mitigation scheme can improve the OSNR sensitivity compared with that of the conventional KK receiver. In terms of computational complexity, the requirement of proposed scheme is higher than that of KK receiver, as symbol decision and SSBI reconstruction are needed in this scheme. One approach to reduce the computational complexity is estimating SSBI without making symbol decisions.

In conclusion, when the minimum phase condition is violated at low CSPRs KK algorithm cannot recover the optical field accurately, and the proposed enhanced SSBI mitigation can effectively reduce the CSPR by 2-3 dB compared to that for the conventional KK receiver.

5.3. Virtual CSPR enhancement

Since the KK receiver requires a high CSPR to meet minimum phase condition, generally a strong carrier is generated at the transmitter side and propagates along with the signal, which inevitably limits the power of information-bearing signal. The alternative solution can be generating the carrier at the receiver using another laser source, and this approach definitely increases the system cost. Another choice is splitting the carrier and information-bearing signal using multi-core fiber or two separate SMF [168], while one separate path to accommodate the carrier inherently increases the system complexity. For the various optical field recovery direct detection schemes shown in Table 4.2, the required CSPR ranges from 9 dB to 15 dB after transmission over the fiber. As adopting a low CSPR may sacrifice the system performance, one solution is transmitting the signals with the low CSPR at the transmitter while enhancing the carrier power digitally at the receiver side.

Correspondingly, the virtual CSPR enhancement was proposed to relax the requirement of high CSPRs at the transmitter side.

The signal processing procedure can be elaborated as two stages. The first stage is obtaining the preliminary symbol decisions via conventional KK relations. Then the second stage is adding DC and reconstructing SSBI terms using preliminary symbol decisions to realize the virtual CSPR enhancement. Specifically, the carrier and information-bearing signals are denoted as C and S, respectively. At low CSPRs, signals are distorted due to the violation of minimum phase condition, distorted signals are denoted as S', which are the preliminary symbol decisions given by the KK algorithm. To achieve a high CSPR at the receiver, the reconstructed received photocurrent I' is given by

$$\begin{aligned} I' &= \left|\sqrt{\Delta CSPR}\cdot C + S\right|^2 \\ &= \Delta CSPR\cdot\left|C\right|^2 + \left|S\right|^2 + 2\sqrt{\Delta CSPR}\,\mathrm{Re}(C\cdot S^*) \end{aligned} \tag{5.6}$$

where $\Delta CSPR$ (e.g., >1) is the virtual CSPR increment in decimal format, and Re(·) denotes the real part of a complex value. The original photocurrent I is shown in Eq.(3.9), when the CSPR of signals increases by $\Delta CSPR$, I' is used to denote the photocurrent of signals with CSPR increment of $\Delta CSPR$. I' can be estimated using the known original photocurrent I and preliminary symbol decisions S' as follows

$$\begin{aligned} I' \approx{}& \sqrt{\Delta CSPR}\cdot I + (\Delta CSPR - \sqrt{\Delta CSPR})\cdot\left|C\right|^2 \\ &+ (1-\sqrt{\Delta CSPR})\cdot\left|S'\right|^2 \end{aligned} \tag{5.7}$$

As such, the photocurrent with increased CSPR is obtained. This approach virtually increases the CSPR at the receiver, and hence avoids the issue of nonlinearity due to the strong carrier. Meanwhile, when the CSPR is not sufficiently high to fully satisfy the minimum phase condition for the conventional KK receiver, this virtual CSPR enhancement can enable the accurate optical field recovery at low CSPRs.

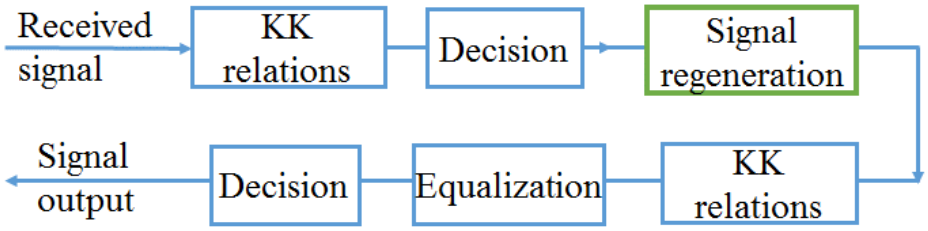

Fig. 5.6 DSP flow chart for the proposed virtual CSPR enhancement scheme.

The DSP flow chart is presented in Fig. 5.6, where the core of this scheme is the signal regeneration using the formula shown in Eq. (5.7). The variable of signal regeneration is the CSPR increment, which is swept from 1 to 5 dB to figure out the optimal value. The experimental setup is same as Fig. 3.10, and the experimental results are depicted in Fig. 5.7.

At the BER threshold of 1×10^{-3}, the OSNR sensitivity and the corresponding optimal $\Delta CSPR$ as a function of original CSPR are shown in Fig. 5.7, where the original CSPR, namely, the CSPR at the transmitter side is denoted as $CSPR_0$. The secondary vertical axis of Fig. 5.7 is the optimal $\Delta CSPR$, which only applies to the proposed virtual CSPR enhancement scheme. From Fig. 5.7 it can be seen that $\Delta CSPR$ is not the higher the better, that is because the regenerated signals are based on the

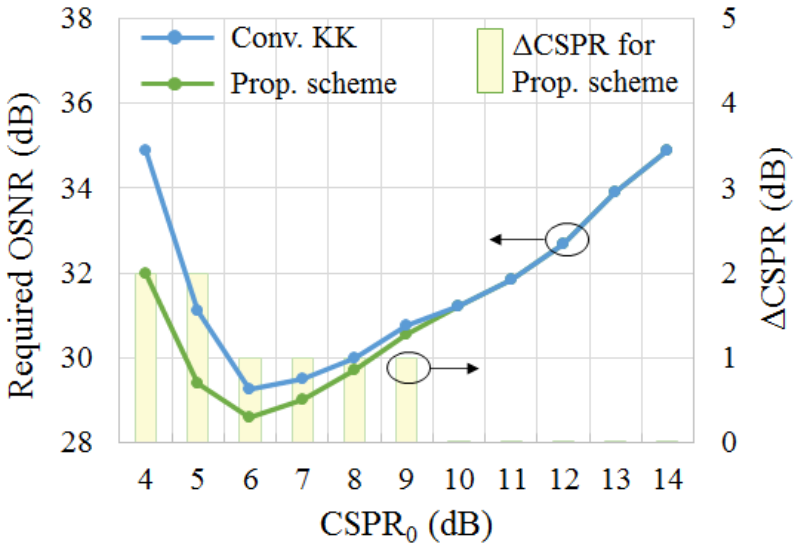

Fig. 5.7 Required OSNR and optimal ΔCSPR as a function of original CSPR in the btb configuration.

preliminary symbol decisions which may contain some errors, and the decision error propagation would be amplified by a large $\Delta CSPR$, which leads to the degradation of system performance when the CSPR increment is too large. As such, the optimal CSPR increment indicates the balance between the improvement of system performance given by the digitally increased CSPR and symbol decision error propagation. In the btb circumstance, the optimal increment of CSPR is from 0 to 2 dB, depending on the original CSPRs. When the original CSPR is low (e.g., 4-5 dB), an increment CSPR of 2 dB can evidently improve the BER performance. At high CSPR regions (e.g., $CSPR_0$> 5dB), the optimal $\Delta CSPR$ is lower than those at low CSPR regions. This phenomenon is attributed to the fact that at low CSPRs the minimum phase condition required by KK receiver is not fully satisfied, and the virtual CSPR increment at the receiver can compensate the penalty induced by the violation of minimum phase condition. While at high CSPRs, the predominant limitation of system performance is SNR rather than the penalty induced by not fully satisfying minimum phase condition. As such, when the original CSPR is sufficiently large, the virtual increase of CSPR is not an effective approach to improve the performance, which is verified by the fact that when the CSPR is larger than 9 dB, the optimal $\Delta CSPR$ is 0 and the virtual CSPR enhancement scheme has the same performance as conventional KK receiver. It is worth noting that the optimal CSPR for the conventional KK receiver is 6 dB, however, the virtual CSPR enhancement scheme can provide the OSNR sensitivity improvement of 0.6 dB, indicating that 6-dB CSPR does not fully satisfy the minimum phase condition. Instead, this value is the compromise between the strict satisfaction of minimum phase condition and the system performance degradation induced by the high CSPR. Therefore, the proposed virtual CSPR enhancement scheme has been demonstrated to exploit the potential improvement of system performance.

As discussed in Chapter 3, the KK receiver requires a higher CSPR after transmission over the fiber than that in the btb condition. The proposed virtual CSPR enhancement scheme is implemented to verify the effectiveness of reducing CSPRs. Fig. 5.8 presents the required OSNR and optimal ΔCSPR for both conventional and proposed schemes after 160-km transmission. Compared to the optimal CSPR of 6 dB

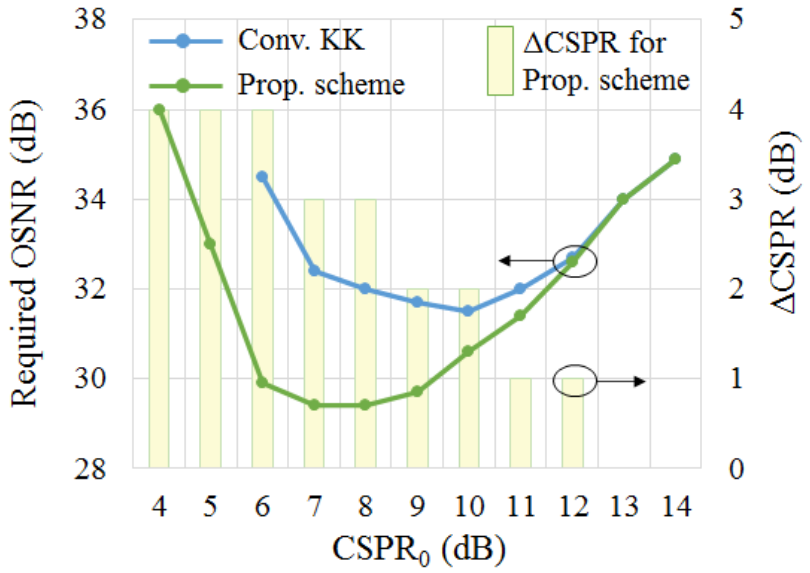

Fig. 5.8 Required OSNR and optimal ΔCSPR as a function of original CSPR after 160-km transmission.

for the KK receiver in the btb condition, the optimal CSPR increases to 10 dB after 160-km transmission, indicating that KK receiver is sensitive to CD. For conventional KK receiver, the OSNR sensitivity degrades by 2.3 dB after 160-km transmission with each optimal CSPR (e.g., 6-dB CSPR for the btb, and 10-dB CSPR for the transmission case). For the proposed virtual CSPR enhancement scheme, the optimal increment of CSPR can be up to 4 dB at low $CSPR_0$ regions, and $\Delta CSPR$ gradually decreases as the $CSPR_0$ increases, and the virtual CSPR enhancement scheme does not improve the system performance when $CSPR_0$ is larger than 12 dB. It is worth noting that the optimal $\Delta CSPR$ shown in Fig. 5.8 is generally larger than that at btb. This is because after transmission the PAPR of signal increases due to CD impacts, the minimum phase condition is violated at the receiver, and the results shown in Fig. 5.8 indicate the proposed signal regeneration with the CSPR increment can effectively alleviate the requirement of high CSPR. The optimal CSPR using the proposed virtual CSPR enhancement is 7 dB as shown in Fig. 5.8, which is 3 dB lower than that for KK receiver, and the OSNR sensitivity is improved by 2.1 dB compared to the conventional KK receiver.

To sum up, the proposed virtual CSPR enhancement scheme has presented the capability of relaxing requirement of high CSPRs, and the optimal CSPR can be reduced by 3 dB, with the OSNR improvement of 2.1 dB.

5.4. Power loading scheme for CADD

In the previous two sections, algorithms of reducing required CSPR for SSB based direct detection have been elaborated, and this section concentrates on the CSPR reduction scheme for the DSB based scheme, which is power loading scheme for CADD.

One unique feature of CADD is the nonuniform transfer function, which shapes the SNR curves as illustrated in Fig. 4.11. In the vicinity of zero frequency, the SNR is generally lower than that in the high frequency regions, and the decision errors made for the low-frequency subcarriers are propagated to the SSBI reconstructed process,

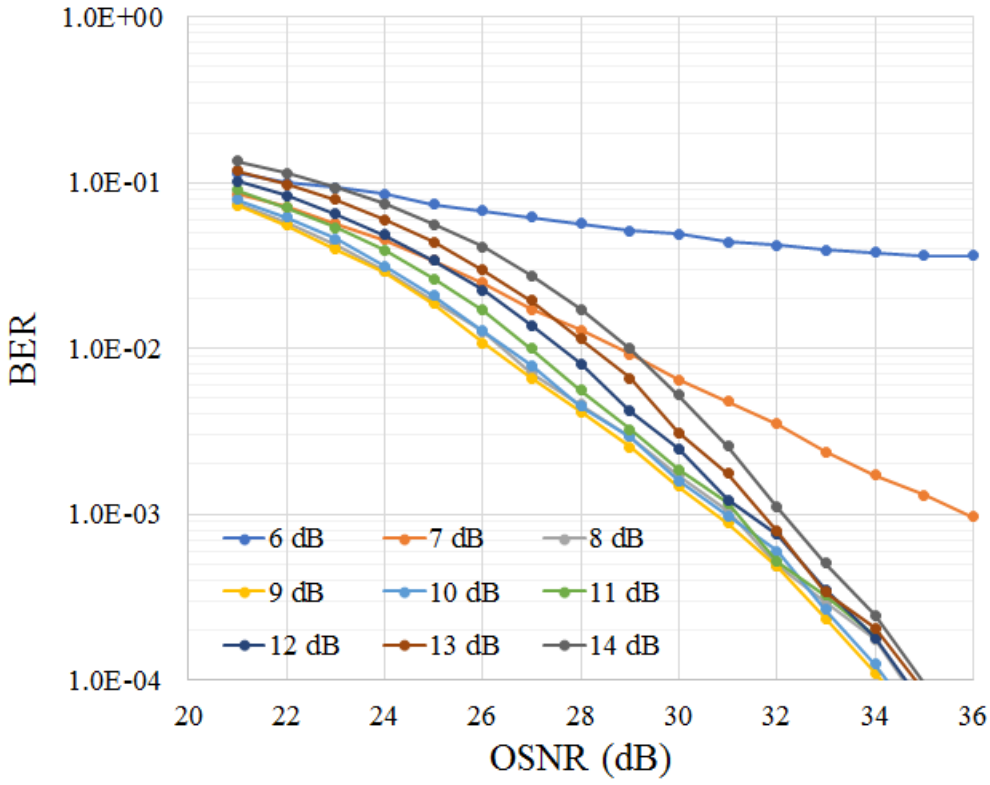

Fig. 5.9 BER performance versus OSNR for the CADD receiver with uniform power loading.

leading to the error propagation. The decision errors in low frequency regions are partially due to the severe SSBI, and hence to combat the SSBI, more power can be allocated in the low frequency region to enable the relatively accurate symbol decisions, which lead to the system performance improvement with a low CSPR.

For the 25-Gbaud QAM16 OFDM signals with 5% guard band, the simulated system performance using various CSPRs is shown in Fig. 5.9, where subcarriers carrying data are with the same loaded power, namely, the uniform power loading. For the 6-dB CSPR, there exists the error floor and it cannot reach the BER threshold of 1×10^{-3}. The optimal CSPR is found to be 9 dB for the uniform power loading circumstance. With merely 2 dB lower than the optimal CSPR, 7-dB case is evidently inferior to the 9-dB CSPR, and OSNR sensitivity is 35.9 dB and 30.8 dB for the 7- and 9-dB CSPR cases, respectively. At the BER threshold of 1×10^{-3}, the required OSNR for each CSPR is shown in Fig. 5.10. When the CSPR is larger than 9 dB the higher CSPR does not provide the performance improvement, as the system is limited by the optical noise rather than SSBI. Since it is desirable to load power on information-bearing signals rather than the carrier, it is preferable to enable CADD receiver work properly at low CSPRs (e.g., 7-dB CSPR). One effective approach is loading nonuniform power according to the colored SNR curve as shown in Fig. 4.11 to combat SSBI.

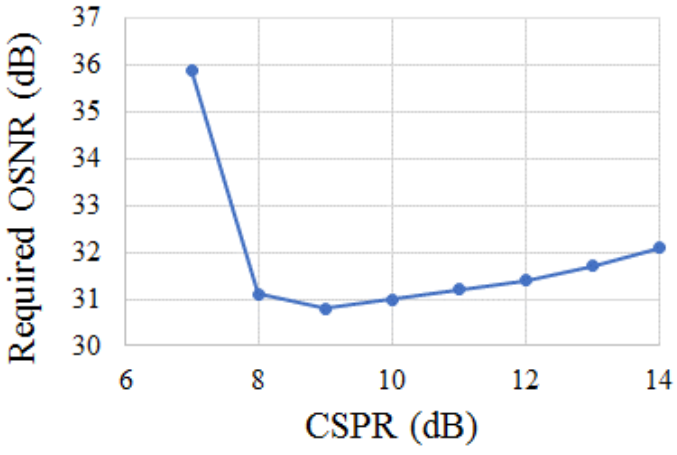

Fig. 5.10 Required OSNR for each CSPR.

Although the SSBI distortions are more severe in the vicinity of zero-frequency region, the guard band cannot be too wide because of the valued spectral efficiency. With the unchanged spectral efficiency, the solution is loading more power on the signals in the low-frequency region than those in the high-frequency region. As the spectrum of SSBI is 'triangular', the loading scheme is triangular power loading as illustrated in Fig. 5.11. As such, two parameters need to be determined: (1) the bandwidth of the frequency region to load more power, (2) the increment of power to load. It is worth noting that some other functions beyond the 'triangular' shape can be adopted, however, the triangular loading scheme is deemed to the simplest one.

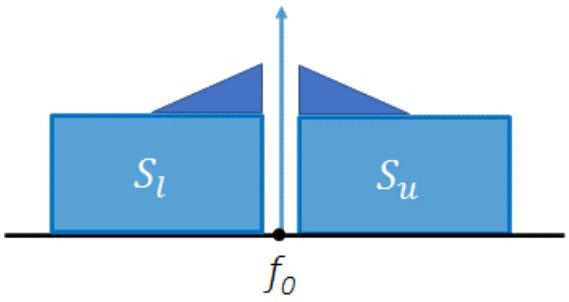

Fig. 5.11 Schematic diagram of triangular power loading scheme. S_l and S_u are lower and upper sideband signals, respectively.

Simulation is conducted to demonstrate the effectiveness of this proposed triangular power loading scheme. For the 25-Gbaud QAM16 OFDM signal with 5 % gap, 7-dB CSPR is adopted to investigate the system performance improvement given by the nonuniform power loading scheme at a low CSPR example. To identify the optimal bandwidth of frequency region to load 'triangular' like power, the amplitude of the signal in the subcarrier nearest to the carrier is set to be twice than the other subcarriers with no triangular power loading, corresponding to 6 dB in power, and then linearly decreases to the amplitude of subcarriers with no triangular power loading. The optimization of the frequency region bandwidth to conduct triangular power is shown in Fig. 5.12. For example, the bandwidth of 2.5 GHz shown in the legend of Fig. 5.12 indicates the subcarrier occupying 2.5 GHz in each sideband are with triangular power loading, in other words, for 25 Gbaud signals with 5% guard band

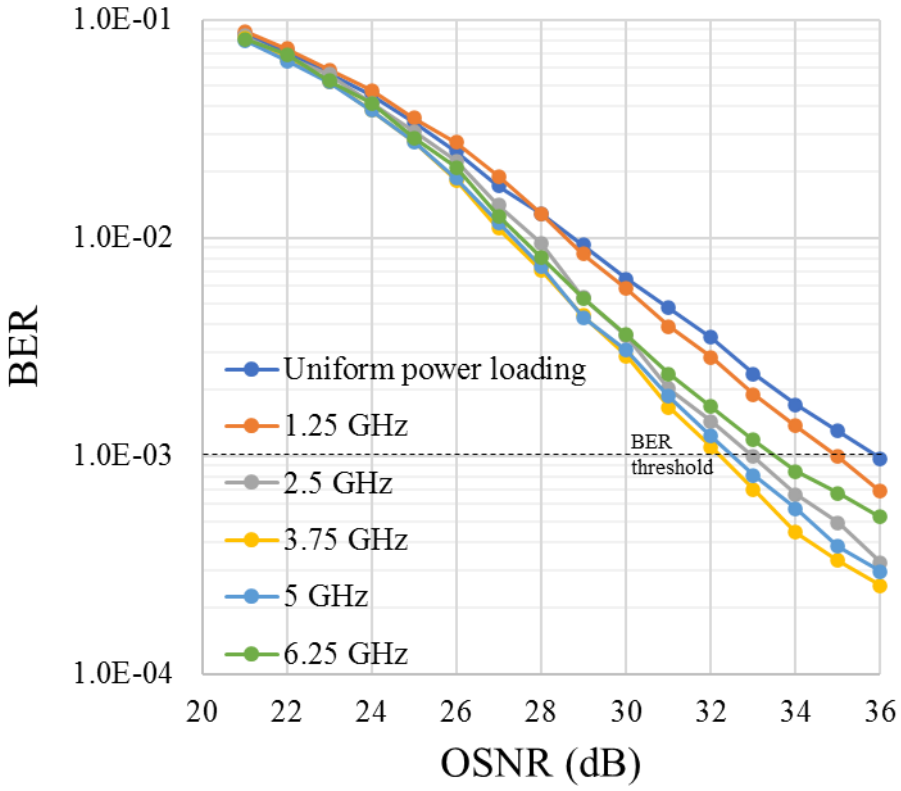

Fig. 5.12 Optimization of bandwidth of the frequency region to implement triangular power loading.

the subcarriers in the frequency region of [-3.125 GHz, -0.625 GHz] and [0.625 GHz, 3.125 GHz] are implemented with triangular power loading. It can be found that the triangular power loading is generally superior to the conventional uniform power loading. The optimal bandwidth to conduct triangular power loading is found to be 3.75 GHz. However, the optimal bandwidth is no longer 3.75 GHz when the increment of amplitude changes, as the optimal system performance depends on the interplay between the bandwidth and increment of amplitude.

The jointly optimized increment of amplitude and bandwidth for the proposed triangular power loading scheme is shown in Fig. 5.13. For example, the amplitude of 4.5 indicates the amplitude of the subcarrier nearest to the guard band is 4.5 times that of the subcarriers without triangular power loading, and the triangular power loading scheme follows the diagram shown in Fig. 5.11. When the increment of amplitude is small, the optimal bandwidth needs to be relatively large. That is because for the narrow guard band (e.g., merely 5% of the signal bandwidth) signals cannot be fully

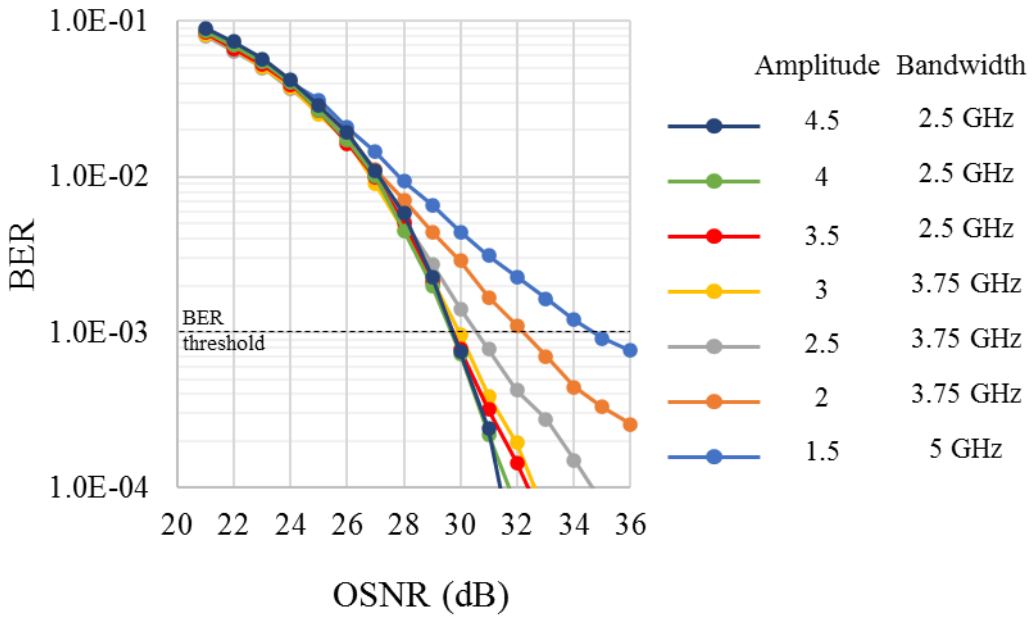

Fig. 5.13 Joint optimization of amplitude and bandwidth for the triangular power loading.

allocated in the SSBI suppression region, and the SSBI is severe in the low-frequency region, as such, the bandwidth which is with triangular power loading to combat SSBI is large. At the BER threshold of 1×10^{-3}, several combinations of amplitude and bandwidth can achieve the OSNR sensitivity of lower than 30 dB. While for the uniform loading cases with various CSPRs shown in Fig. 5.9, no OSNR sensitivity lower than 30 dB is obtained. Besides, the optimal CSPR for uniform power loading scheme is 9 dB, while the optimal triangular power loading is implemented with the CSPR of 7 dB which is 2 dB lower, meanwhile, prominent OSNR sensitivity improvement is achieved. This is because the 7-dB CSPR for the uniform power loading is not sufficiently high to mitigate and combat SSBI distortions, and the subcarriers in the low frequency region possess low SNRs as depicted in Fig. 4.11. The low-SNR subcarriers provide symbol decisions with relatively low accuracy, and the error propagation exists while reconstructing and mitigating SSBI. As such, the CADD receiver does not work properly at low CSPRs. By adopting the proposed triangular power loading scheme, even 7-dB CSPR presents superior performance with the OSNR sensitivity of 29.8 dB at the BER threshold of 1×10^{-3}.

It has been demonstrated that CADD receiver can work properly at 7-dB CSPR using proposed triangular power loading scheme, however, the 7-dB CSPR is not optimal for CADD receiver as shown in Fig. 5.9. Beyond the scope of CSPR reduction, to further investigate the OSNR improvement merely given by triangular power loading scheme (e.g., using the same CSPR as the uniform power loading scheme), the 9-dB CSPR condition is studied. Analogous to the optimization of bandwidth and increment of amplitude procedure, the optimal parameters are first obtained for the 9-dB CSPR, and the SNR versus frequency using the triangular power loading is depicted in Fig. 5.14.

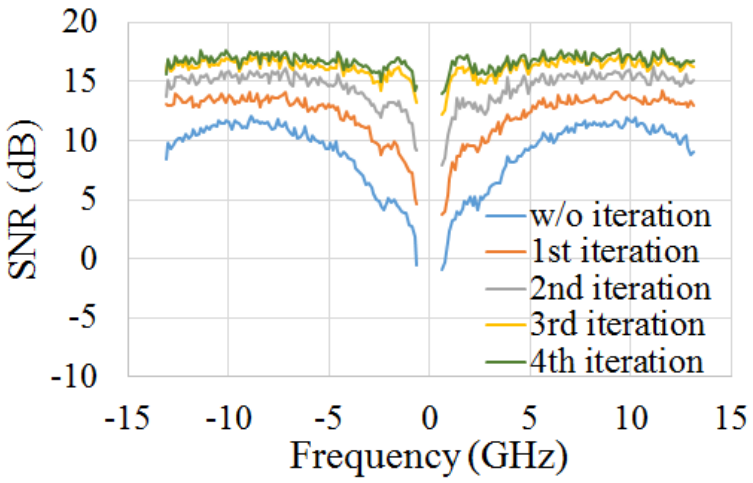

Fig. 5.14 SNR versus frequency for 25Gbaud signals with 5% frequency gap with triangular power loading @ optical delay=60 ps, CSPR=9 dB, and OSNR=28 dB.

With the aid of triangular power loading, the severe SNR fading induced by both SSBI characteristic and transfer function of CADD receiver has been remarkably alleviated. As shown in Fig. 5.14, the SNR curve of no iteration is not even over the signal frequency, while due to the nonuniform power loading the SNR in the vicinity of guard band is slightly improved. As the iterations are carried out, SNR gradually increases and the averaged SNR after four iterations is 16.64 dB, while the averaged SNR for the uniform power loading 16.15 dB. This phenomenon verifies the fact that the triangular power loading is effective in improving the overall system performance rather than blindly enhancing the subcarriers in the low-frequency region and sacrificing the SNR at high frequency. The principle is that triangular power loading

enables low-frequency subcarriers with relatively more power, which is favorable to make accurate symbol decisions. As such, the error propagation issues are alleviated, and SSBI can be mitigated more effectively using more accurate symbol decisions in an iterative manner. Since SSBI distortions are regarded as 'noise', when noise is more effectively removed signals with less SSBI possess higher SNRs. For the subcarriers in the high-frequency region, although the SNR slightly decreases since the power is compromised to enhance low-frequency subcarriers, the slightly decreased SNR does not affect to make correct symbol decisions via deliberately tuning the parameters used in triangular power loading scheme. Another phenomenon is that SNR curve using triangular power loading is generally even after four iterations compared to the colored SNR curve shown in Fig. 4.11. This is because the simple but deliberately tuned triangular shaped power loading complements the transfer function of CADD receiver, and the fading SNR shaped by transfer function can be compensated by the enhanced signal power loading. The BER performance as a function of OSNR is depicted in Fig. 5.15(a), and the uniform power loading case is also presented as a reference. At the BER threshold of 1×10^{-3}, the OSNR sensitivity improvement is 2.7 dB. Besides, the mutual information versus OSNR is presented in Fig. 5.15(b) to evaluate the

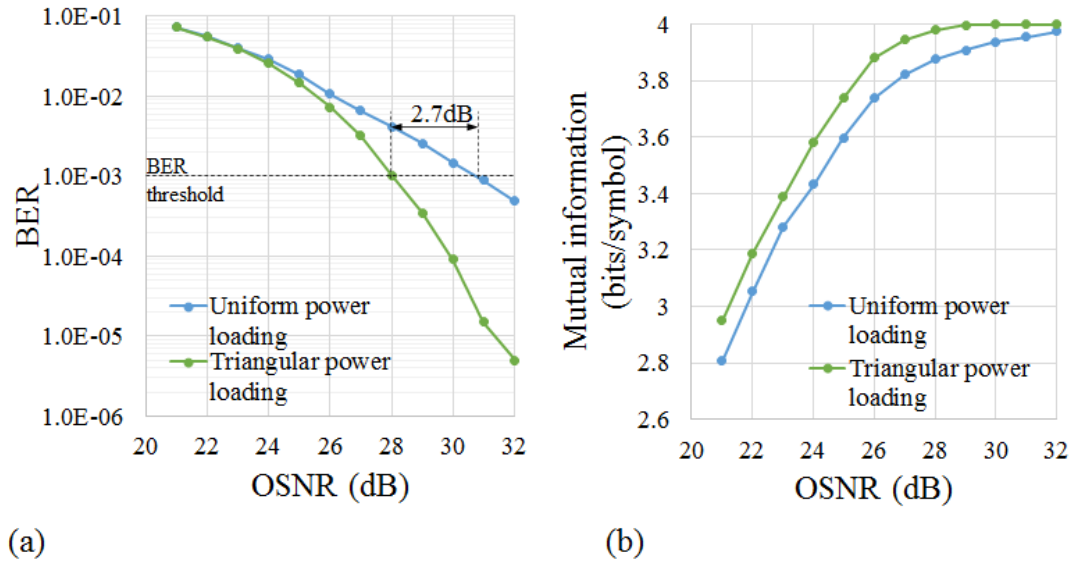

Fig. 5.15 (a) BER versus OSNR. (b) Mutual information versus OSNR for uniform and triangular power loading.

improvement of system capacity via adopting the proposed triangular power loading scheme.

To conclude, the proposed triangular power loading enables the CADD receiver to work at low CSPRs. The averaged SNR over the signal bandwidth is improved, and the severe SNR fading issue is predominantly alleviated via triangular power loading scheme.

Chapter 6 Conclusions

6.1. Summary of this work

The recent decade has witnessed the rapid development of high-capacity short- to medium-reach optical networks, and accordingly, a cost-effective detection scheme with optical field recovery is on demand. The conventional IMDD system has the disadvantage of CD induced power fading, while the conventional coherent detection is so far not a promising solution for cost-sensitive transports. In this thesis, various novel low-cost direct detection schemes with the field recovery have been studied and proposed, and hence elongate the transmission distance compared with the traditional intensity-only detection schemes.

6.1.1. Field recovery of SSB signal

Due to the square-law detection, the folding issue between the lower and upper sideband signals poses the problem on the direct detection of intensity-modulated signals. As such, the direct detection enabled field recovery of complex-valued signal was initially designed to fit for SSB signals, where one sideband carries the data with the other truncated. The recently proposed KK and IC receivers are two representatives of direct detection schemes with optical field recovery, and the corresponding modulation formats for each scheme have been studied. Both single-carrier and multi-carrier signals have been adopted for KK and IC receiver schemes, and results show that single-carrier modulation is the better fit for the KK receiver, as the low PAPR of single-carrier signals is favorable for the minimum phase condition required by the KK relations. While for the IC receiver, the OFDM signal possesses the superior performance to the single-carrier signal due to its low correlation between reconstructed SSBI and symbol decisions. This is because the symbol decisions are made in the frequency domain for OFDM signals and SSBI is formed in the time domain. Besides, CD impacts on KK and IC receiver are investigated. Both simulation and experimental demonstrations show that KK receiver is sensitive to CD, namely, the KK receiver requires a higher CSPR as the transmission distance increases and the

IC receiver is robust against the CD impacts. As KK receiver is designed for the short- to medium-reach transports, the first-order PMD impacts on KK receiver are also studied. Although single-polarization signals are adopted for the KK receiver, the frequency-dependent PMD effects may degrade the system performance. However, results show that PMD is a minor factor for the short-reach transmission using KK receivers.

6.1.2. Field recovery of DSB signal

Although the field recovery of SSB signals has been extensively investigated, the required receiver bandwidth generally needs to be the same as the signal bandwidth. In other words, to detect the signal with the bandwidth of B, the required receiver bandwidth is B. Analogous to the fact that homodyne receiver is more widely implemented over heterodyne receiver in coherent detection, the required receiver bandwidth is a major concern for the cost of optical transports. As such, it is highly desirable to relax the requirement of receiver bandwidth, for example, to detect signal bandwidth of B with the required receiver bandwidth of B/2. Correspondingly, a direct detection scheme called CADD fitting for DSB signals is worth investigating. The working principle of the CADD scheme along with the algorithm of recovering the field of DSB signals has been elaborated, and various parameters including the bandwidth of inserted frequency gap, length of optical delay, and CSPR have been optimized via simulations. For the same bit rate, the required receiver bandwidth comparison of DSB based coherent and CADD schemes and various SSB based schemes have been conducted. Although the proposed CADD scheme requires higher receiver bandwidth than that of homodyne coherent detection mainly due to the small frequency gap and high CSPR, CADD is superior to the other SSB direct detection schemes in terms of electrical spectral efficiency. Regarding the practical implementation of CADD scheme, since the IQ modulator is utilized, one concern is the IQ mismatch. Both amplitude and phase mismatch impacts on CADD are studied, and results show that even though the IQ imbalance degrades the performance of CADD scheme as a whole, the imperfection of IQ paths does not affect the effectiveness of SSBI iterative cancellation.

6.1.3. Techniques of reducing CSPR

For both above-mentioned SSB and DSB signal direct detection schemes, a strong carrier is required to obtain the replica of signals while suppressing the impacts of SSBI. However, no information is loaded on the carrier and hence the strong carrier indicates the sacrifice of power efficiency. To reduce the required carrier power, namely, reduce the CSPR, three schemes have been proposed for SSB and DSB direct detection schemes. For SSB signals, the proposed enhanced SSBI mitigation scheme is conducting the consequent SSBI reconstruction and cancellation after employing KK relations, and hence enables the improved performance with lower CSPRs. Besides, the CSPR can be virtually enhanced at the receiver side, which refers to the virtual CSPR enhancement scheme. Both schemes based on SSB signals can effectively reduce the optimal CSPR by 2 to 3 dB. For DSB signal based CADD scheme, a simple but effective power loading scheme has been proposed to enhance the low-frequency subcarrier performance. The proposed triangular power loading scheme enables relatively accurate symbol decisions, which is beneficial for SSBI reconstruction and mitigation. Therefore, the requirement of high CSPR is alleviated. Results show that the optimal CSPR of 9 dB for the conventional CADD scheme can be reduced to 7 dB with prominent OSNR improvement.

6.2. Future work and perspectives

Given the prevalence of data centers, the short- to medium-reach high-capacity transmission links with low cost will be in great demand. To break the bottleneck of limited transmission distance for conventional IMDD system and complicated receiver structure for coherent detection, novel cost-effective direct detection schemes with field recovery will be promising solutions in the near future. Accordingly, the gap between conventional coherent and direct detection will be narrowed.

Given that the spectral efficiency is a valued resource, the null sideband for SSB signals and the frequency gap inserted in the vicinity of carrier for DSB signals leave the room for improvement. From the perspective of the carrier power, more DSP techniques of reducing the carrier power is expected. As to the receiver structure, a

simplification of the CADD structure will be desirable. One example is the reduction of one ADC as presented in [169].

Besides, to further increase the system capacity, the modulation and transmission beyond one single mode in fiber combined with direct detection can be a future research topic. Furthermore, the IQ modulator used in the CADD scheme still has issues in its cost and the bulky size for short-reach links. As such, the possibility of generating IQ signals using DMLs combined with direct detection at the receiver side is worthy of exploration.

Bibliography

[1] Alan Willner, “Optical fiber telecommunications,” Academic Press, vol. 11, (2019).

[2] Jean-Marie Dilhac, “The telegraph of claude chappe-an optical telecommunication network for the XVIIIth century,” Institute National des Sciences Appliquées de Toulouse (2001).

[3] K. C. Kao and G. A. Hockham, “Dielectric-fiber surface waveguides for optical frequencies,” IEEE Proc., vol. 113, no. 7, pp. 1151-1158, (1966).

[4] M. Sathish Kumar, “Fundamentals of optical fibre communication,” (2005).

[5] Dave Evans, “The Internet of Things how the next evolution of the Internet is changing everything,” Cisco white paper.

[6] Cisco, “Cisco Annual Internet Report (2018–2023),” White Paper (2020).

[7] Paul W. Shumate, “Fibre-to-the-home:1997-2007,” Journal of Lightwave Technology, vol. 26, no. 9, pp. 1093–1103, (2008).

[8] Kazuro Kikuchi, “Fundamentals of coherent optical fiber communications,” Journal of Lightwave Technology, vol. 34, no. 1, pp. 157–179, (2016).

[9] Govind P. Agrawal, “Fiber-optic Communication Systems,” 3rd ed., John Wiley & Sons, (2010).

[10] Seb J. Savory, “Digital coherent optical receivers: algorithms and subsystems,” IEEE Journal of Selected Topics in Quantum Electronics, vol. 16, no. 5, pp. 1164-1179, (2010).

[11] R. P. Giddings, X. Q. Jin, E. Hugues-Salas, E. Giacoumidis, J. L. Wei, and J. M. Tang, “Experimental demonstration of a record high 11.25Gb/s real-time optical OFDM transceiver supporting 25km SMF end-to-end transmission in simple IMDD systems,” Optics Express, vol. 18, no. 6, pp.5541-5555, (2010).

[12] Fan Li, Dongdong Zou, Qi Sui, Jianping Li, Xingwen Yi, Liangchuan Li, and Zhaohui Li “Optical amplifier-free 100 Gbit/s/lamda PAM-N transmission and

reception in O-band over 40-km SMF with 10-G Class DML," in Optical Fiber Communication Conference (OFC) 2019, paper Tu2F.4.

[13] Jiao Zhang, Jianjun Yu, Xinying Li, Yiran Wei, Kaihui Wang, Li Zhao, Wen Zhou, Jiangnan Xiao, Xiaolong Pan, Bo Liu, Xiangjun Xin, Liwei Zhang, and Yun Zhang, "Demonstration of 100-Gb/s/λ PAM-4 transmission over 45-km SSMF using one 10G-class DML in the C-band," in Optical Fiber Communication Conference (OFC) 2019, paper Tu2F.1.

[14] Jian Chen, Acai Tan, Zhengxuan Li, Tingting Xu, Linghuan Liang, Wei Chen, Yingchun Li, and Yingxiong Song, "50-km C-band transmission of 50-Gb/s PAM4 using 10-G EML and complexity-reduced adaptive equalization," IEEE Photonics Journal, vol. 11, no. 1, pp. 1-10, (2019).

[15] Radhakrishnan Nagarajan, Mark Filer, Yang Fu, Masaki Kato, Todd Rope, and James Stewart, "Silicon photonics-based 100 Gbit/s, PAM4, DWDM data center interconnects," Journal of Optical Communications and Networking, vol. 10, no. 7, B25-B36, (2018).

[16] Ilyadis Nicholas, "Large Scale Data Centers and the Evolution to 100G Ethernet," in Optical Fiber Communication Conference (OFC) 2012, paper OW1J.4.

[17] José Manuel Estarán, Haik Mardoyan, Filipe Jorge, Oskars Ozolins, Aleksejs Udalcovs, Agnieszka Konczykowska, Muriel Riet, Bernadette Duval, Virginie Nodjiadjim, Jean-Yves Dupuy, Xiaodan Pang, Urban Westergren, Jiajia Chen, Sergei Popov, and Sébastien Bigo, "140/180/204-Gbaud OOK transceiver for inter- and intra-data center connectivity," Journal of Lightwave Technology, vol. 37, no. 1, pp. 178-187, (2019).

[18] Chongjin Xie, Lei Wang, Liang Dou, Ming Xia, Sai Chen, Huan Zhang, Zhao Sun, and Jingchi Cheng, "Open and disaggregated optical transport networks for data center interconnects," Journal of Optical Communications and Networking, vol. 12, no. 6, pp. 12-22, (2020).

[19] Zhe Li, M. Sezer Erkilinc, Lidia Galdino, Kai Shi, Benn C. Thomsen, Polina Bayvel, and Robert I. Killey, "Comparison of digital signal-signal beat interference compensation techniques in direct-detection subcarrier modulation systems," Optics Express, vol. 24, no.25, pp. 29176-29189, (2016).

[20] Arthur James Lowery, Liang Du, and Jean Armstrong, "Orthogonal frequency division multiplexing for adaptive dispersion compensation in long haul WDM systems," in Optical Fiber Communication Conference (OFC) 2006, paper PDP39.

[21] Wei-Ren Peng, Xiaoxia Wu, Vahid R. Arbab, Bishara Shamee, Louis C. Christen, Jeng-Yuan Yang, Kai-Ming Feng, Alan E. Willner, and Sien Chi, "Experimental demonstration of a coherently modulated and directly detected optical OFDM system using an RF-tone insertion," in Optical Fiber Communication Conference (OFC) 2008, paper OMU2.

[22] Antonio Mecozzi, Cristian Antonelli, and Mark Shtaif, "Kramers–Kronig coherent receiver," Optica vol. 3, no. 11, pp. 1220–1227, (2016).

[23] Godfrey Anuga Akpakwu, Bruno J. Silva, Gerhard P. Hancke, and Adnan M. Abu-Mahfouz, "A survey on 5G networks for the Internet of Things: communication technologies and challenges," IEEE Access, vol. 6, pp. 3619-3647, (2018).

[24] Xiang Liu and Frank Effenberger, "Emerging optical access network technologies for 5G wireless," Journal of Optical Communications and Networking vol. 8, no.12, B70-B79, (2016).

[25] Thomas Pfeiffer, "Next generation mobile fronthaul and midhaul architectures," Journal of Optical Communications and Networking vol. 7, no.11, B38-B45, (2015).

[26] Mu Xu, Jhih-Heng Yan, Junwen Zhang, Feng Lu, Jing Wang, Lin Cheng, Daniel Guidotti, Gee-Kung Chang, "Bidirectional fiber-wireless access technology for 5G mobile spectral aggregation and cell densification," Journal of Optical Communications and Networking vol. 8, no. 12, B104-B110 (2016).

[27] Nikolaos-Panteleimon Diamantopoulos, Hiroshi Yamazaki, Suguru Yamaoka, Munehiko Nagatani, Hidetaka Nishi, Hiromasa Tanobe, Ryo Nakao, Takuro Fujii, Koji Takeda, Takaaki Kakitsuka, Hitoshi Wakita, Minoru Ida, Hideyuki Nosaka, Fumio Koyama, Yutaka Miyamoto, and Shinji Matsuo, "Net 321.24-Gb/s IMDD transmission based on a >100-GHz bandwidth directly-Modulated laser," in Optical Fiber Communication Conference (OFC) 2020, PDP paper1-3.

[28] Jiao Zhang, Kaihui Wang, Yiran Wei, Li Zhao, Wen Zhou, Jiangnan Xiao, Bo Liu, Xiangjun Xin, Feng Zhao, Ze Dong, and Jianjun Yu, "280 Gb/s IM/DD PS-PAM-8 transmission over 10 km SSMF at O-Band for optical interconnects," in Optical Fiber Communication Conference (OFC) 2020, paper 1-3.

[29] Mohamed Morsy-Osman, Mathieu Chagnon, and David V. Plant, "Four-dimensional modulation and Stokes direct detection of polarization division multiplexed intensities, inter polarization phase and inter polarization differential phase," Journal of Lightwave Technology, vol. 34, no. 7, pp. 1585–1592, (2016).

[30] Robbert van der Linden, Nguyen-Cac Tran, Eduward Tangdiongga, and Ton Koonen, "Increasing flexibility and capacity in real PON deployments by using 2/4/8-PAM formats," in Optical Fiber Communication Conference (OFC) 2016, paper 1-3.

[31] Zhiguo Zhang, Bingbing Zhang, Yanxu Chen, Bingchang Hua, and Xue Chen, "Channel-reuse IMDD-based 40 Gb/s/λ 16-QAM Nyquist-SCM downstream and 20 Gb/s/λ Nyquist 4 PAM upstream WDM-PON," in OptoElectronics and Communication Conference, OECC (2016), paper 1-3.

[32] Junwen Zhang, Jun Shan Wey, Jianyang Shi, Jianjun Yu, Zhijuan Tu, Bo Yang, Wei Yang, Yong Guo, Xingang Huang, and Zhuang Ma, "Experimental demonstration of unequally spaced PAM-4 signal to improve receiver

sensitivity for 50-Gbps PON with power-dependent noise distribution," in Optical Fiber Communication Conference (OFC) 2018, paper 1-3.

[33] Doutje van Veen, Vincent Houtsma, and Hungkei Chow, "Demonstration of symmetrical 25 Gbps quaternary PAM/duobinary TDM-PON with multilevel interleaving of users," in European Conference on Optical Communication (ECOC) 2015, paper PD.3.3.

[34] Ming Chen, Jing He, Jin Tang, Xian Wu, and Lin Chen, "Real-time 10.4-Gb/s single-band optical 256/64/16QAM receiver for OFDM-PON," IEEE Photonics Technology Letters, vol. 26, no. 20, pp. 2012-2015, (2014).

[35] Ming Chen, Jing He, and Lin Chen, "Real-time demonstration of 1024-QAM OFDM transmitter in short-reach IMDD systems," IEEE Photonics Technology Letters, vol. 27, no. 8, pp. 824-827, (2015).

[36] Shohei Beppu, Keisuke Kasai, Masato Yoshida, and Masataka Nakazawa, "2048 QAM (66 Gbit/s) single-carrier coherent optical transmission over 150 km with a potential SE of 15.3 bit/s/Hz," in Optical Fiber Communication Conference (OFC) 2014, paper 1-3.

[37] Yiran Wei, Yingjun Zhou, Cuiwei Liu, Feng Wang, Kaihui Wang, Junting Shi, Nan Chi, and Jianjun Yu, "C-Band PS 4096QAM OFDM FSO transmission with 6.98bit/s/Hz net SE based on Kramers-Kronig detection," in Optical Fiber Communication Conference (OFC) 2020, paper 1-3.

[38] Masaki Terayama, Seiji Okamoto, Keisuke Kasai, Masato Yoshida, and Masataka Nakazawa, "4096 QAM (72 Gbit/s) single-carrier coherent optical transmission with a potential SE of 15.8 bit/s/Hz in all-Raman amplified 160 km fiber link," in Optical Fiber Communication Conference (OFC) 2018, paper 1-3.

[39] Xi Chen, Junho Cho, Andrew Adamiecki, and Peter Winzer, "16384-QAM transmission at 10GBD over 25-km SMF using polarization-multiplexed probabilistic constellation shaping," in European Conference on Optical Communication (ECOC) 2019, paper PD.3.3.

[40] Frederik Klejs, Edson P. da Silva, Mads Lillieholm, Metodi P. Yankov, Toshio Morioka, Leif K. Oxenlewe, and Michael Galili, “Spectrally efficient DP-1024QAM 640 Gb/s long haul transmission using a frequency comb,” in Optical Fiber Communication Conference (OFC) 2020, paper 1-3.

[41] An Li, Abdullah Amin, Xi Chen, and William Shieh, “Reception of mode and polarization multiplexed 107-Gb/s CO-OFDM signal over a two-mode fiber,” in Optical Fiber Communication Conference (OFC) 2011, PDP paper B8.

[42] Karsten Schuh, Fred Buchali, Roman Dischler, Mathieu Chagnon, Vahid Aref, Henning Buelow, Qian Hu, Florian Pulka, Massimo Frascolla, Esmaeel Alhammadi, Adel Samhan, Islam Younis, Mohamed El-Zonkoli, and Peter Winzer, “49.2-Tbit/s WDM transmission over 2×93-km field-deployed fiber,” in Optical Fiber Communication Conference (OFC) 2011, paper 1-3.

[43] Jun Sakaguchi, Yoshinari Awaji, Naoya Wada, Atsushi Kanno, Tetsuya Kawanishi, Tetsuya Hayashi, Toshiki Taru, Tetsuya Kobayashi, and Masayuki Watanabe, “109-Tb/s (7×97×172-Gb/s SDM/WDM/PDM) QPSK transmission through 16.8-km homogeneous multi-core fiber,” in Optical Fiber Communication Conference (OFC) 2011, paper PDPB6.

[44] Jun Sakaguchi, Benjamin J. Puttnam, Werner Klaus, Yoshinari Awaji, Naoya Wada, Atsushi Kanno, Tetsuya Kawanishi, Katsunori Imamura, Harumi Inaba, Kazunori Mukasa, Ryuichi Sugizaki, Tetsuya Kobayashi, Masayuki Watanabe, “19-core fiber transmission of 19x100x172-Gb/s SDM-WDM-PDM-QPSK signals at 305Tb/s,” in Optical Fiber Communication Conference (OFC) 2012, paper PDP5C.1.

[45] Yang Hong, Kyle R. H. Bottrill, Natsupa Taengnoi, Naresh K. Thipparapu, Yu Wang, Andrey A. Umnikov, Jayanta K. Sahu, David J. Richardson, and Periklis Petropoulos, “Experimental demonstration of dual O+C-Band WDM transmission over 50-km SSMF with direct detection,” Journal of Lightwave Technology, vol. 38, no. 8, pp. 2278–2284, (2020).

[46] Pierre Mertz, Stephen Grubb, Jeffrey Rahn, Warren Sande, Marc Stephens, James O'Connor, Matthew Mitchell, Stefan Voll, "Record ultra-high full-fill capacity Trans-Atlantic submarine deployment ushering in the SDM era," in Optical Fiber Communication Conference (OFC) 2020, paper M2D.1.

[47] Shota Ishimura, Byung Gon Kim, Kazuki Tanaka, Kosuke Nishimura, Hoon Kim, and Yun C. Chung, and Masatoshi Suzuki, "Broadband IF-Over-Fiber Transmission With Parallel IM/PM Transmitter Overcoming Dispersion-Induced RF Power Fading for High-Capacity Mobile Fronthaul Links," IEEE Photonics Journal, vol. 10, no. 1, pp. 1-10, (2018).

[48] Sha Zhu, Ming Li, Ning Hua Zhu, and Wei Li, "Chromatic-dispersion-induced power-fading suppression technique for bandwidth-quadrupling dual-chirp microwave signals over fiber transmission," Optics Letters, vol. 44, no. 4, pp. 923-926, (2019).

[49] Shangyuan Li, Xiaoping Zheng, Hanyi Zhang, and Bingkun Zhou, "Compensation of dispersion-induced power fading for highly linear radio-over-fiber link using carrier phase-shifted double sideband modulation," Optics Letters, vol. 36, no. 4, pp. 546-548, (2011).

[50] Alan E. Willner, Salman Khaleghi, Mohammad Reza Chitgarha, and Omer Faruk Yilmaz, "All-optical signal processing," Journal of Lightwave Technology, vol. 32, no. 4, pp. 660–680, (2014).

[51] Xi Xiao, Miaofeng Li, Lei Wang, Daigao Chen, Qi Yang, and Shaohua Yu, "High speed silicon photonic modulators" in Optical Fiber Communication Conference (OFC) 2017, paper 1-3.

[52] Hoon Kim, "EML-based optical single sideband transmitter," IEEE Photonics Technology Letters, vol. 20, no. 4, pp. 243-245, (2008).

[53] Ning Hua Zhu, Zhan Shi, Zhi Ke Zhang, Yi Ming Zhang, Can Wen Zou, Ze Ping Zhao, Yu Liu, Wei Li, and Ming Li, "Directly modulated semiconductor lasers," IEEE Journal of Selected Topics in Quantum Electronics, vol. 24, no. 1, pp. 1–19, (2018).

[54] Zhengxuan Li, Lilin Yi, Wei Wei, Meihua Bi, Hao He, Shilin Xiao, and Weisheng Hu, “Symmetric 40-Gb/s, 100-km passive reach TWDM-PON with 53-dB loss budget,” vol. 32, no. 21, pp. 3389-3396, (2014).

[55] Fred Buchali, Karsten Schuh, Son Thai Le, Xuan-Quang Du, Markus Grözing, and Manfred Berroth, “A SiGe HBT BiCMOS 1-to-4 ADC frontend supporting 100 GBaud PAM4 reception at 14 GHz digitizer bandwidth,” in Optical Fiber Communication Conference (OFC) 2019, Paper Th4A.7.

[56] Avigdor Brillant, “Digital and analog fiber optic communications for CATV and FTTx applications,” John Wiley & Sons, (2008).

[57] Chuanbowen Sun, S. H. Bae, and Hoon Kim, “Transmission of 28-Gb/s duobinary and PAM-4 signals using DML for optical access network,” IEEE Photonics Technology Letters, vol. 29, no. 1, pp. 130-133, (2017).

[58] Rodney. S. Tucker, “High-speed modulation of semiconductor lasers,” IEEE Transactions on Electron Devices vol. 32, no. 12, pp. 2572–2584, (1985).

[59] Asier Villafranca, Javier Lasobras, and Ignacio Garcés, “Precise characterization of the frequency chirp in directly modulated DFB lasers,” in Proceedings Spanish Conference on Electron Devices (Madrid, Spanish), pp. 173-176, (2007).

[60] Laurens Breyne, Michiel Verplaetse, Christian Neumeyr, Timothy De Keulenaer, Wouter Soenen, Xin Yin, Peter Ossieur, Guy Torfs, and Johan Bauwelinck, “DSP-free and real-time NRZ transmission of 50 Gb/s over 15-km SSMF and 64 Gb/s back-to-back with a 1.3-μm VCSEL” Journal of Lightwave Technology, vol. 37, no. 1, pp. 170–177, (2019).

[61] M. Verplaetse, L. Breyne, Christian Neumeyr, Timothy De Keulenaer, Wouter Soenen, X. Yin, P. Ossieur, G. Torfs, and J. Bauwelinck, “DSP-free and real-time NRZ transmission of 50Gb/s over 15km SSMF and 64Gb/s back-to-back with a 1.3μm VCSEL,” in Optical Fiber Communication Conference (OFC) 2018, paper 1-3.

[62] Antonio Malacarne, Fabio Falconi, Christian Neumeyr, Wouter Soenen, Claudio Porzi, Timo Aalto, Juergen Rosskopf, Marco Chiesa, Johan Bauwelinck, and Antonella Bogoni, “Low-power 1.3-μm VCSEL transmitter for data center interconnects and beyond,” in European Conference on Optical Communication (ECOC) 2017, paper 1-3.

[63] Ming Li, Ye Deng, Jian Tang, Shuqian Sun, Jianping Yao, Jose Azana, and Ninghua Zhu, “Reconfigurable optical signal processing based on a distributed feedback semiconductor optical amplifier,” Scientific reports, vol. 6, pp. 19985-19993, (2016).

[64] Di Che, Qian Hu, and William Shieh, “Linearization of direct detection optical channels using self-coherent subsystems,” Journal of Lightwave Technology, vol. 34, no. 2, pp. 516–524, (2016).

[65] G.H. Smith, D. Novak, and Z. Ahmed, “Technique for optical SSB generation to overcome dispersion penalties in fibre-radio systems,” Electronics Letters, vol. 33, no. 1, pp. 74-75, (1997).

[66] Ze Li, Hao Chi, Xianmin Zhang, and Jianping Yao, “Optical single-sideband modulation using a Fiber-Bragg-Grating-Based optical Hilbert transformer,” IEEE Photonics Technology Letters, vol. 23, no. 9, pp. 558-560, (2011).

[67] Doo-Ho Kim, Joo-Young Lee, Hyung-June Choi, and Jong-in Song, “All-optical single-sideband frequency upconversion utilizing the XPM effect in an SOA-MZI,” Optics Express, vol. 24, no.18, pp. 20309-20317, (2016).

[68] Graham H. Smith, Dalma Novak, and Zaheer Ahmed, “Overcoming chromatic-dispersion effects in fiber-wireless systems incorporating external modulators,” IEEE Transactions on microwave theory and techniques, vol. 45, no. 8, pp. 1410-1415, (1997).

[69] Carl. F. Kurth, “Generation of single-sideband signals in multiplex communication system,” IEEE Transactions on Circuits and Systems, vol. 23, no.1, pp. 1-17, (1976)

[70] Katsumi Takano, Nobutomo Hanzawa, Sadayuki Tanji, and Kiyoshi Nakagawa, “Experimental demonstration of optically phase-shifted SSB modulation with fiber-based optical Hilbert transformers,” in Optical Fiber Communication Conference, OFC (2007), paper JThA48.

[71] Ken-ichi Kitayama, Toshiaki Kuri, Member, Kiyoshi Onohara, Tomotada Kamisaka, and Kiyotaka Murashima, “Dispersion effects of FBG filter and optical SSB filtering in DWDM millimeter-wave fiber-radio systems,” Journal of Lightwave Technology, vol. 20, no. 8, pp. 1397–1407, (2002).

[72] J. Park, W.V. Sorin, and K.Y. Lau, “Elimination of the fibre chromatic dispersion penalty on 1550nm millimetre-wave optical transmission,” Electronics Letters, vol. 33, no. 6, pp. 512-513, (1997).

[73] Kazushige Yonenaga, and Noboru Takachio, “A fiber chromatic dispersion compensation technique with an optical SSB transmission in optical homodyne detection systems,” IEEE Photonics Technology Letters, vol. 5, no. 8, pp. 949-951, (1993).

[74] Yixiao Zhu, Kaiheng Zou, and Fan Zhang, “C-Band 112 Gb/s Nyquist single sideband direct detection transmission over 960 km SSMF,” IEEE Photonics Technology Letters, vol. 29, no. 8, pp. 651-654, (2017).

[75] Kaiheng Zou, Yixiao Zhu, and Fan Zhang, “800 Gb/s (8 × 100 Gb/s) Nyquist digital signal processing for short reach optical links single-sideband modulation direct-detection transmission over 320 km SSMF at C-band,” Journal of Lightwave Technology, vol. 35, no. 10, pp. 1900–1905, (2017).

[76] Son Thai Le, Karsten Schuh, Fred Buchali, and Hung Nguyen Tan, “5×240 Gb/s WDM DD transmission over 80 km with spectral efficiency of 5.25 bit/s/Hz,” IEEE Photonics Technology Letters, vol. 31, no. 22, pp. 1830-1833, (2019).

[77] S. Shimotsu, M. Izutsu, T. Kawanishi, S. Oikawa, and M. Sasaki, “Wideband frequency conversion with LiNbO3 optical single-sideband modulator,” in Optical Fiber Communication Conference, OFC (2001), paper WK3.

[78] Qian Hu, Robert Borkowski, Mathieu Chagnon, Karsten Schuh, Fred Buchali, and Henning Bülow, “Novel optical field reconstruction for IM/DD with receiver bandwidth well below full optical signal bandwidth,” in Optical Fiber Communication Conference, OFC (2020), paper M4F.3.

[79] Di Che, Yasuhiro Matsui, Xi Chen, Richard Schatz, and Patrick Iannone, “400-Gb/s direct modulation using a DFB+R laser,” Optics Letters, vol. 45, no. 12, pp. 3337-3339, (2020).

[80] Di Che, An Li, Xi Chen, Qian Hu, Yifei Wang, and William Shieh, “Stokes vector direct detection for short-reach optical communication,” Optics Letters, vol. 39, no. 11, pp. 3110–3113, (2014).

[81] Shigeru Kanazawa, Hiroshi Yamazaki, Yasuhiko Nakanishi, Takeshi Fujisawa, Kiyoto Takahata, Yuta Ueda, and Wataru Kobayashi, Yoshifumi Muramoto, Hiroyuki Ishii, and Hiroaki Sanjoh, “Transmission of 214-Gbit/s 4-PAM signal using an ultra-broadband lumped-electrode EADFB laser module,” in Optical Fiber Communication Conference, OFC (2016), paper Th5B.3.

[82] M. A. Mestre, F. Jorge, H. Mardoyan, J. Estaran, F. Blache, P. Angelini, A. Konczykowska, M. Riet, V. Nodjiadjim, J-Y. Dupuy, and S. Bigo, “100-Gbaud PAM-4 intensity-modulation direct detection transceiver for datacenter interconnect,” in European Conference on Optical Communication, ECOC (2016), Paper. M.2.C.2.

[83] Haik Mardoyan, Miquel A. Mestre, Jose Manuel Estarán, Filipe Jorge, Fabrice Blache, Philippe Angelini, Agnieszka Konczykowska, Muriel Riet, Virginie Nodjiadjim, Jean-Yves Dupuy, and Sebastien Bigo, “84-, 100-, and 107-GBd PAM-4 intensity modulation direct-detection transceiver for data center interconnects,” Journal of Lightwave Technology, vol. 35, no. 6, pp. 1253–1259, (2017).

[84] Liang Zhang, Jinlong Wei, Nebojsa Stojanovic, Cristian Prodaniuc, and Changsong Xie, “Beyond 200-Gb/s DMT transmission over 2-km SMF based on a low-cost architecture with single-wavelength, single DAC/ADC and single-PD,” in European Conference on Optical Communication, ECOC (2018), paper We1H.1

[85] P. Torres-Ferrera, H. Wang, V. Ferrero, R. Mercinelli, and R. Gaudino, “Towards 50 Gb/s in high-speed PON: optimization of modulation formats using pre-chirping,” in International Conference on Transparent Optical Networks, ICTON (2018), paper 1-3.

[86] Lilin Yi, Zhengxuan Li, Meihua Bi, Wei Wei, and Weisheng Hu, “Symmetric 40-Gb/s TWDM-PON with 39-dB power budget,” IEEE Photonics Technology Letters, vol. 25, no. 7, pp. 644-647, (2013).

[87] Tiago M. F. Alves, and Adolfo V. T. Cartaxo, “Power Budget of Ultra-Dense Virtual-Carrier-Assisted DD MB-OFDM Next-Generation PON,” IEEE Photonics Technology Letters, vol. 28, no. 13, pp. 1406-1409, (2016).

[88] Houtsma Vincent, and Van Veen Doutje, “Bi-Directional 25G/50G TDM-PON With Extended Power Budget Using 25G APD and Coherent Detection,” Journal of Lightwave Technology, vol. 36, no. 1, pp. 122-127, (2017).

[89] Van Veen Doutje T., Houtsma Vincent E., Gnauck Alan H., and Iannone Patrick, “Demonstration of 40-Gb/s TDM-PON over 42-km with 31 dB optical power budget using an APD-based receiver,” Journal of Lightwave Technology, vol. 33, no. 8, pp. 1675-1680, (2015).

[90] Gerd Keiser, “Optical fiber communications,” (2008).

[91] Joe C. Campbell, “Recent advances in telecommunications avalanche photodiodes,” Journal of Lightwave Technology, vol. 25, no. 1, pp. 109-121, (2007).

[92] Fang Xu, Mohammad-Ali Khalighi, and Salah Bourennane, “Impact of different noise sources on the performance of PIN- and APD-based FSO

receivers," International Conference on Telecommunications (2011), paper 1-3.

[93] William Shieh, Chuanbowen Sun, and Honglin Ji, "Carrier-assisted differential detection," Light: Science & Applications, vol. 9, no. 1, pp. 1–9, Feb. 2020.

[94] Irshaad Fatadin, and Seb J. Savory, "Compensation of frequency offset for 16-QAM optical coherent systems using QPSK partitioning," IEEE Photonics Technology Letters, vol. 23, no. 17, pp. 1246-1248, (2011).

[95] S. Adhikari, S. L. Jansen, M. Alfiad, B. Inan, V. A. J. M. Sleiffer, A. Lobato, P. Leoni, and W. Rosenkranz, "Self- coherent optical OFDM: An interesting alternative to direct or coherent detection," International Conference on Transparent Optical Networks (2011), paper 1-3.

[96] Nelson J. Muga, Romil K. Patel, Isiaka A. Alimi, Nuno A. Silva, and Armando N. Pinto, "Self-coherent optical detection for access and metro networks," in International Conference on Transparent Optical Networks, ICTON (2019), paper 1-3.

[97] X. Chen, S. Chandrasekhar, and P. Winzer, "Self-coherent systems for short reach transmission," in European Conference on Optical Communication, ECOC (2018), paper 1−3.

[98] Mingyang Lyu, Wei Shi, Leslie Rusch, "SiP-based SSBI cancellation for OFDM," IEEE Photonics Journal, vol. 11, no. 5, pp. 1-14, (2019).

[99] Peter J. Winzer, David T. Neilson, and Andrew R. Chraplyvy, "Fiber-optic transmission and networking: the previous 20 and the next 20 years," Optics Express, vol. 26, no. 18, pp. 24190-24239, (2018).

[100] Kangping Zhong, Xian Zhou, Jiahao Huo, Changyuan Yu, Chao Lu, and Alan Pak Tao Lau, "Digital signal processing for short-reach optical communications: A review of current technologies and future trends," Journal of Lightwave Technology, vol. 36, no. 2, pp. 377–400, (2018).

[101] Nicklas Eiselt, Jinlong Wei, Helmut Griesser, Annika Dochhan, Michael Eiselt, Jörg-Peter Elbers, Juan José Vegas Olmos, and Idelfonso Tafur Monroy, "First real-time 400G PAM-4 demonstration for inter-data center transmission over 100 km of SSMF at 1550 nm," in Optical Fiber Communication Conference, OFC (2016), paper 1-3.

[102] Kaiheng Zou, Yixiao Zhu, Fan Zhang, and Zhangyuan Chen, "Spectrally efficient terabit optical transmission with Nyquist 64-QAM half-cycle subcarrier modulation and direct-detection," Optics Letters, vol. 41, no. 12, pp. 2767–2770, (2016).

[103] Jens C. Rasmussen, Tomoo Takahara, Toshiki Tanaka, Yutaka Kai, Masato Nishihara, Tomislav Drenski, Lei Li, Weizhen Yan, and Zhenning Tao, "Digital signal processing for short reach optical links," in European Conference on Optical Communication, ECOC (2014) paper Tu.1.1.3.

[104] Liang Zhang, Jinlong Wei, Nebojsa Stojanovic, Cristian Prodaniuc, Changsong Xie, "Beyond 200-Gb/s DMT Transmission Over 2-km SMF Based on A Low-Cost Architecture with Single-Wavelength, Single-DAC/ADC and Single-PD," in European Conference on Optical Communication, ECOC (2018) paper We1H.1.

[105] Liang Zhang, Tianjian Zuo, Yuan Mao, Qiang Zhang, Enbo Zhou, Gordon Ning Liu, Xiaogeng Xu, "Beyond 100-Gb/s transmission over 80-km SMF using direct-detection SSB-DMT at C-Band," Journal of Lightwave Technology, vol. 34, no. 2, pp. 723-729, (2016).

[106] Jianyang Shi, Junwen Zhang, Yingjun Zhou, Yiguang Wang, Nan Chi, and Jianjun Yu, "Transmission performance comparison for 100-Gb/s PAM-4, CAP-16, and DFT-S OFDM with direct detection," Journal of Lightwave Technology, vol. 35, no. 23, pp. 5127–5133, (2017).

[107] John C. Cartledge, and Abdullah S. Karar, "100 Gb/s intensity modulation and direct detection," Journal of Lightwave Technology, vol. 32, no. 16, pp. 2809–2814, (2014).

[108] Xiaodan Pang, Oskars Ozolins, Rui Lin, Lu Zhang, Aleksejs Udalcovs, Lei Xue, Richard Schatz, Urban Westergren, Shilin Xiao, Weisheng Hu, Gunnar Jacobsen, Sergei Popov, and Jiajia Chen, "200 Gbps/lane IM/DD technologies for short reach optical interconnects," Journal of Lightwave Technology, vol. 38, no. 2, pp. 492–503, (2020).

[109] Arthur James Lowery, and Jean Armstrong, "Orthogonal-frequency-division multiplexing for dispersion compensation of long-haul optical systems," Optics Express, vol. 14, no. 6, pp. 2079-2084, (2006).

[110] Wei-Ren Peng, Xiaoxia Wu, Vahid R. Arbab, Kai-Ming Feng, Bishara Shamee, Louis C. Christen, Jeng-Yuan Yang, Alan E. Willner, and Sien Chi, "Theoretical and experimental investigations of direct-detected RF-tone-assisted optical OFDM systems," Journal of Lightwave Technology, vol. 27, no. 10, pp. 1332–1339, (2009).

[111] Brendon J. C. Schmidt, Zuraidah Zan, Liang B. Du, and Arthur J. Lowery, "120 Gbit/s over 500-km using single-band polarization-multiplexed self-coherent optical OFDM," Journal of Lightwave Technology, vol. 28, no. 4, pp. 328-335, (2010).

[112] Don F. Hewitt, "Orthogonal frequency division multiplexing using baseband optical single sideband for simpler adaptive dispersion compensation," in Optical Fiber Communication Conference, OFC (2007), paper OME7.

[113] Z. Li, M. S. Erkilinc, R. Maher, L. Galdino, K. Shi, B. C. Thomsen, B. Bayvel, and R. I. Killey, "Reach enhancement for WDM direct-detection subcarrier modulation using low-complexity two-stage signal-signal beat interference cancellation," in European Conference on Optical Communication, ECOC (2016), pp. 1–3.

[114] An Li, Wei-Ren Peng, Yan Cui, and Yusheng Bai, "Single-λ 112Gbit/s 80-km transmission of PAM4 signal with optical signal-to-signal beat noise cancellation," in Optical Fiber Communication Conference, OFC (2018), paper Tu2C.5.

[115] Mingyang Lyu, Wei Shi, and Leslie A. Rusch, “SiP alternative to enhanced KK for OFDM,” in European Conference on Optical Communication, ECOC (2018), pp. 1–3.

[116] Mingyang Lyu, Xun Guan, Zhihui Cao, Wei Shi, and Leslie A. Rusch, “Experimental examination of SSBI suppression using sip microring resonators,” in International Topical Meeting on Microwave Photonics, MWP (2017), pp. 1–4

[117] Xi Chen, An Li, Di Che, Qian Hu, Yifei Wang, Jiayuan He, and William Shieh, “Block-wise phase switching for double-sideband direct detected optical OFDM signals,” Optics Express, vol. 12, no. 11, pp. 13436-13441, (2013).

[118] Xi Chen, An Li, Di Che, Qian Hu, Yifei Wang, Jiayuan He, and William Shieh, “Highspeed fading-free direct detection for double-sideband OFDM signal via block-wise phase switching,” in Optical Fiber Communication Conference, OFC (2013), paper PDP5B.7.

[119] Xi Chen, An Li, Qian Hu, Jiayuan He, Di Che, Yifei Wang, and William Shieh, “Demonstration of direct detected optical OFDM signals via block-wise phase switching,” Journal of Lightwave Technology, vol. 32, no. 4, pp. 722-728, (2013).

[120] An Li, Di Che, Xi Chen, Qian Hu, Yifei Wang, and William Shieh, “61 Gbits/s direct-detection optical OFDM based on blockwise signal phase switching with signal-to-signal beat noise cancellation,” Optics Letters, vol. 38, no. 14, pp. 2614–2616, (2013).

[121] Di Che, Xi Chen, An Li, and William Shieh, “Signal-carrier interleaved direct-detection in optical single-carrier communication systems,” in OptoElectronics and Communication Conference, OECC (2014), paper 1-3.

[122] Di Che, Xi Chen, Jiayuan He, An Li, and William Shieh, “102.4-Gb/s single-polarization direct-detection reception using signal carrier interleaved optical

OFDM," in Optical Fiber Communication Conference, OFC (2014), paper 1-3.

[123] H. Voelcker, "Demodulation of single-sideband signals via envelope detection," IEEE Transactions on Communication Technology, vol. 14, no.1, pp. 22–30, (1966).

[124] Cristian Antonelli, Mark Shtaif, and Antonio Mecozzi, "Kramers-Kronig PAM transceiver," in in Optical Fiber Communication Conference, OFC (2017), paper Tu3I.5.

[125] X. Chen, C. Antonelli, S. Chandrasekhar, G. Raybon, J. Sinsky, A. Mecozzi, M. Shtaif, P. Winzer, "218-Gb/s single-wavelength, single-polarization, single-photodiode transmission over 125-km of standard singlemode fiber using Kramers-Kronig detection," in Optical Fiber Communication Conference, OFC (2017), paper Th5B.6.

[126] Z. Li, M. S. Erkilinç, K. Shi, E. Sillekens, L. Galdino, B. C. Thomsen, P. Bayvel, and R. I. Killey, "168 GB/s/λ direct detection 64-QAM SSB Nyquist-SCM transmission over 80 km uncompensated SSMF at 4.54 b/s/Hz net ISD using a Kramers-Kronig receiver," in European Conference on Optical Communication ECOC (2017), paper 1-3.

[127] Son Thai Le, Karsten Schuh, Mathieu Chagnon, Fred Buchali, and Henning Buelow, "1.6Tbps WDM direct detection transmission with virtual-carrier over 1200km," in Optical Fiber Communication Conference, OFC (2018), paper Tu2D.5.

[128] Yingjun Zhou, Jianjun Yu, Yiran Wei, Jianyang Shi, and Nan Chi, "Four-channel WDM 640 Gb/s 256 QAM transmission utilizing Kramers-Kronig receiver," Journal of Lightwave Technology, vol. 37, no. 21, pp. 5466-5473, (2019).

[129] Cristian Antonelli, Antonio Mecozzi, and Mark Shtaif, "Kramers–Kronig PAM Transceiver and Two-Sided Polarization-Multiplexed Kramers–Kronig

Transceiver," Journal of Lightwave Technology, vol. 36, no. 2, pp. 468-475, (2018).

[130] X. Chen, C. Antonelli, S. Chandrasekhar, G. Raybon, A. Mecozzi, M. Shtaif, and P. Winzer, "4 × 240 Gb/s dense WDM and PDM Kramers-Kronig detection with 125-km SSMF transmission," in European Conference on Optical Communication ECOC (2017), paper W.2.D.4.

[131] Haiyun Xin, Deming Kong, Kuo Zhang, Shi Jia, Yan Fu, Weisheng Hu, and Hao Hu, "100 Gbps simplified coherent PON using carrier-suppressed PDM-PAM-4 and phaee-recovery-free KK detection," in European Conference on Optical Communication ECOC (2019), paper 1-3.

[132] Yuki Yoshida, Akihiro Maruta, and Ken-ichi Kitayama, "On the peak-to-average power ratio distribution along fiber in the optical OFDM transmissions," in 37th European Conference and Exhibition on Optical Communication (2011), paper We. 10. P1. 69.

[133] Asghar Gholami, Denis Molin, and Pierre Sillard, "Compensation of chromatic dispersion by modal dispersion in MMF- and VCSEL-based Gigabit Ethernet transmissions," IEEE Photonics Technology Letters, vol. 21, no. 10, pp. 645-647, (2009).

[134] Rick Pimpinella, Jose Castro, Bulent Kose, and Brett Lane, "Investigation of bandwidth dependence on chromatic and model dispersion in MMF links using VCSELs," in Optical Fiber Communication Conference, OFC (2012), paper 1-3.

[135] Minsik Kim, Byung Gon Kim, Hoon Kim, and Y. C. Chung, "Transmission of 56-Gb/s PAM-4 signal over 2.3 km of MMF using mode-field matched center-launching technique," in OptoElectronics and Communication Conference, OECC (2017), paper 1-3.

[136] Biao Fu, and Rongqing Hui, “Fiber chromatic dispersion and polarization-mode dispersion monitoring using coherent detection,” IEEE Photonics Technology Letters, vol. 17, no. 7, pp. 1561-1563, (2005).

[137] Gilad Goldfarb, and Guifang Li, “Chromatic dispersion compensation using digital IIR filtering with coherent detection,” IEEE Photonics Technology Letters, vol. 19, no. 13, pp. 969-971, (2007).

[138] Maxim Kuschnerov, Fabian N. Hauske, Kittipong Piyawanno, Bernhard Spinnler, Mohammad S. Alfiad, Antonio Napoli, and Berthold Lankl, “DSP for coherent single-carrier receivers,” Journal of Lightwave Technology, vol. 27, no. 16, pp. 3614-3622, (2009).

[139] Brendon J. C. Schmidt, Arthur James Lowery, and Jean Armstrong, “Impact of PMD in single-receiver and polarization-diverse direct-detection optical OFDM,” Journal of Lightwave Technology, vol. 27, no. 14, pp. 2792-2799, (2009).

[140] Chongjin Xie, “Polarization-mode-dispersion impairments and mitigation in ultra-high speed transmission,” in IEEE/LEOS Summer Topical Meeting, pp. 244–245, (2007).

[141] Neda Cvijetic, Lei Xu, and Ting Wang, “Adaptive PMD compensation using OFDM in long-haul 10 Gb/s DWDM systems,” in Optical Fiber Communication Conference, OFC (2007), paper OTuA5.

[142] Ivan B. Djordjevic, “PMD compensation in fiber-optic communication systems with direct detection using LDPC-coded OFDM,” Optics Express, vol. 15, no. 7, pp. 3692–3701, (2007).

[143] Di Che, An Li, Xi Chen, Qian Hu, Yifei Wang, and William Shieh, “Stokes vector direct detection for linear complex optical channels,” Journal of Lightwave Technology, vol. 33, no. 3, pp. 678-684, (2015).

[144] P. J. Winzer and R. Essiambre, “Advanced optical modulation formats,” Proc. IEEE vol. 94, no. 5, pp. 952–985, (2006).

[145] Z. Li, M.S. Erkılınç, K. Shi, E. Sillekens, L. Galdino, B.C. Thomsen, P. Bayvel, and R.I. Killey, “112 Gb/s/λ WDM direct-detection Nyquist-SCM transmission at 3.15 (b/s)/Hz over 240 km SSMF enabled by novel beating interference compensation,” in Optical Fiber Communication Conference, OFC (2017), paper Tu3I.4.

[146] Yixiao Zhu, Mingxuan Jiang, and Fan Zhang, “4Tb/s faster-than-Nyquist WDM 16-QAM signal transmission with Kramers-Kronig detection,” Asia Communications and Photonics Conference (ACP) 2018, paper 1-3.

[147] Z. Li, M. S. Erkilinc, R. Maher, L. Galdino, K. Shi, B. C. Thomsen, P. Bayvel, and R. I. Killey, “Reach enhancement for WDM direct-detection subcarrier modulation using low-complexity two-stage signal-signal beat interference cancellation,” in European Conference on Optical Communication ECOC (2016), paper M 2.B.1.

[148] Yixiao Zhu, Mingxuan Jiang, Xiaoke Ruan, Chenjia Li, and Fan Zhang, “16×112Gb/s single-sideband PAM4 WDM transmission over 80km SSMF with Kramers-Kronig receiver,” in Optical Fiber Communication Conference, OFC (2018), paper 1-3.

[149] Sujie Fan, Qunbi Zhuge, Mohammed Y. S. Sowailem, Mohamed Morsy-Osman, Thang M. Hoang, Fangyuan Zhang, Meng Qiu, Yan Li, Jian Wu, and David V. Plant, “Twin-SSB direct detection transmission over 80km SSMF using Kramers-Kronig receiver,” in European Conference on Optical Communication, ECOC (2017), paper 1-3.

[150] Yixiao Zhu, Pengfei Wang, Mingxuan Jiang, and Fan Zhang, “4×288Gb/s orthogonal offset carriers assisted PDM twin-SSB WDM transmission with direct detection,” in Optical Fiber Communication Conference, OFC (2019), paper 1-3.

[151] Sujie Fan, Qunbi Zhuge, Mohammed Y. S. Sowailem, Mohamed Morsy-Osman, Thang M. Hoang, Fangyuan Zhang, Meng Qiu, Yan Li, Jian Wu, and David V. Plant, “Twin-SSB direct detection transmission over 80 km SSMF

using Kramers-Kronig receiver," in European Conference on Optical Communication, ECOC (2017), paper W.2.D.

[152] Masayuki Matsumoto, "Optical signal phase reconstruction based on temporal transport-of-intensity equation," Journal of Lightwave Technology, vol. 38, no. 17, pp. 4722-4729, (2020).

[153] Masayuki Matsumoto, "Phase reconstruction scheme using dispersive media in direct detection," in Optical Fiber Communication Conference, OFC (2020), paper 1-3.

[154] Haoshuo Chen, Nicolas K. Fontaine, Joan M. Gene, Roland Ryf, David T. Neilson, and Gregory Raybon, "Full-field, carrier-less, polarization-diversity, direct detection receiver based on phase retrieval," in European Conference on Optical Communication, ECOC (2019), paper Tu.1.D.1.

[155] Chongjin. Xie, Peter J. Winzer, Gregory Raybon, Alan H. Gnauck, Benyuan Zhu, Tommy Geisler, and Bent Edvold, "Colorless coherent receiver using 3x3 coupler hybrids and single-ended detection," Optics Express, vol. 20, no. 2, pp. 1164–1171, (2012).

[156] Jose Krause Perin, Anujit Shastri, and Joseph M. Kahn, "Data center links beyond 100 Gbit/s per wavelength," Optical Fiber Technology, vol. 44, pp. 69–85, (2018).

[157] Tianwai Bo and Hoon Kim, "Toward practical Kramers-Kronig receiver: resampling, performance, and implementation," Journal of Lightwave Technology, vol. 37, no. 2, pp. 461-469, (2018).

[158] Christoph Fullner, Md Mosaddek Hossain Adib, Stefan Wolf, Juned Nassir Kemal, Wolfgang Freude, Christian Koos, and Sebastian Randel, "Complexity analysis of the Kramers-Kronig receiver," vol.37, no. 17, pp. 4295-4307, (2019).

[159] Tianwai Bo and Hoon Kim, “Performance Analysis of Kramers–Kronig Receiver in the Presence of IQ Imbalance,” IEEE Photonics Technology Letters, vol. 30, no. 24, pp. 2171-2174, (2018).

[160] Tianwai Bo and Hoon Kim, “Impact of the IQ imbalance on the performance of Kramers-Kronig receiver,” in OptoElectronics and Communication Conference, OECC (2017), paper 4B4-4.

[161] Simin Chen, Abdullah Al Amin, and William Shieh, “Hybrid frequency-time domain Tx and Rx I/Q imbalance compensation for coherent optical OFDM transmission,” in Asia Communications and Photonics Conference, ACP (2010), paper 437-438.

[162] Al Amin Abdullah, Jansen, Sander L., Takahashi Hidenori, Morita Itsuro, and Tanaka Hideaki, “A hybrid IQ imbalance compensation method for optical OFDM transmission,” Optics Express, vol. 18, no. 5, pp. 4859-4866, (2010).

[163] Shaohua An, Qingming Zhu, Jingchi Li, and Yikai Su, “Modified KK receiver with accurate field reconstruction at low CSPR condition,” in Optical Fiber Communication Conference, OFC (2019), paper M1H.3.

[164] Shaohua An, Qingming Zhu, Jingchi Li, and Yikai Su, “Accurate field reconstruction at low CSPR condition based on a modified KK receiver with direct detection,” Journal of Lightwave Technology, vol. 38, no. 2, pp. 485-491, (2019).

[165] Tonghui Ji, Chuanbowen Sun, Honglin Ji, Zhaopeng Xu, and William Shieh, “Field recovery at low CSPR using interleaved carrier assisted differential detection,” in Optical Fiber Communication Conference (OFC) 2020, paper W4A.3.

[166] Xi Chen, Cristian Antonelli, Sethumadhavan Chandrasekhar, Gregory Raybon, Antonio Mecozzi, Mark Shtaif, and Peter Winzer, “Kramers–Kronig receivers for 100-km datacenter interconnects,” Journal of Lightwave Technology, vol. 36, no. 1, pp. 79-89, (2018).

[167] X. Chen, S. Chandrasekhar, S. Olsson, A. Adamiecki, and P. Winzer, “Impact of O/E front-end frequency response on Kramers-Kronig receivers and its compensation,” in European Conference on Optical Communication, ECOC (2018), paper 1-3.

[168] Thomas Gerard, Zhixin Liu, Lidia Galdino, Polina Bayvel, and Domanic Lavery, “Self-suppression of signal-signal beating interference using a split-carrier transmitter,” in European Conference on Optical Communication, ECOC (2019), paper 1-3.

[169] Yixiao Zhu, Longsheng Li, Yan Fu, and Weisheng Hu, “Symmetric carrier assisted differential detection receiver with low-complexity signal-signal beating interference mitigation,” Optics Express, vol. 28, no.13, pp.19008-19022, (2020).

Appendix A: Acronyms

ADC	analog to digital converter
APD	avalanche photodiode
ASE	amplified spontaneous emission
BPD	balanced photodiode
CADD	carrier assisted differential detection
CD	chromatic dispersion
CP	cyclic prefix
CSPR	carrier-to-signal power ratio
CW	continuous wave
DAC	digital to analog converter
DCF	dispersion compensation fiber
DCI	data center interconnect
DFB	distributed feedback
DGD	differential group delay
DML	directly modulated laser
DSB	double sideband
DSF	dispersion shifted fiber
DSP	digital signal processing
EAM	electro-absorption modulator
ECL	external cavity laser
EDC	electronic dispersion compensation

EDFA	Erbium-doped fiber amplifier
EML	electro-absorption modulated laser
FBG	fiber Bragg grating
FFT	fast Fourier transform
FP	Fabry-perot
FWM	four wave mixing
GS	Gerchberg-Saxton
GVD	group velocity dispersion
IC	iterative cancellation
IFFT	inverse fast Fourier transform
IoT	Internet of things
IQ	in-phase/quadrature
KK	Kramers-Kronig
LO	local oscillator
MI	mutual information
MMF	multi-mode fiber
MRR	micro ring resonator
MZM	Mach-Zehnder modulator
M2M	machine-to-machine
OHT	optical Hilbert transformer
OFDM	orthogonal frequency division multiplexing
OOK	on–off keying

OSNR	optical signal-to-noise ratio
PAM	pulse amplitude modulation
PBC	polarization beam combiner
PC	polarization controller
PD	photodetector
PIC	photonics integrated circuit
PMD	polarization mode dispersion
PON	passive optical network
QAM	quadrature amplitude modulation
SMF	single-mode fiber
SNR	signal-to-noise ratio
SOA	semiconductor optical amplifier
SSB	single sideband
SSBI	signal-signal beat interference
SSMF	standard single-mode fiber
TIA	transimpedance amplifier
TIE	transport-of-intensity equation
TEC	thermoelectric cooler
VCSEL	vertical cavity surface emitting laser
WDM	wave division multiplexing